Development of the partition of unity finite element method for the numerical simulation of interior sound field

Mingming Yang

Par **Mingming YANG**

Development of the partition of unity finite element method for the numerical simulation of interior sound field

Thèse présentée
pour l'obtention du grade
de Docteur de l'UTC

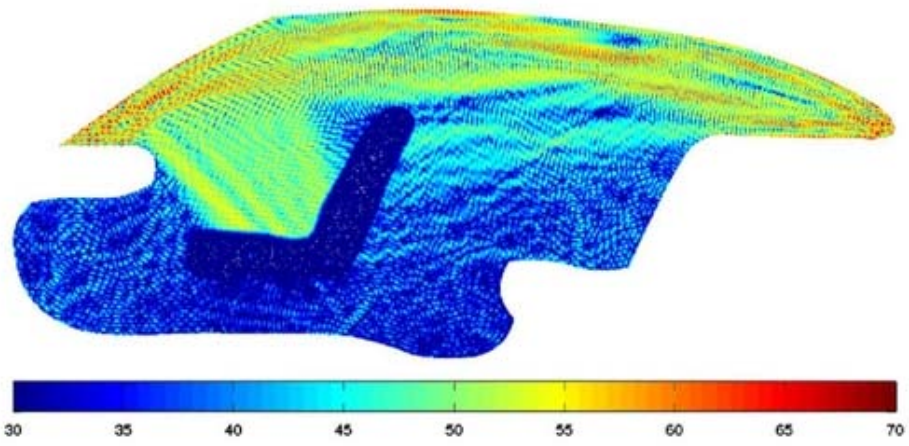

Soutenue le 29 juin 2016
Spécialité : Mécanique Avancée

D2282

Development of the partition of unity finite element method for the numerical simulation of interior sound field

Mingming Yang

Laboratoire Roberval UMR CNRS 7337
Sorbonne Universités, Université de Technologie de Compiègne

This dissertation is submitted for the degree of
Doctor of Philosophy

29 June 2016

Composition of the Jury

Reviewers:		
Alexandre LEBLANC	Université d'Artois	
Christian PRAX	Université de Poitiers	
Examiners:		
Olivier DAZEL	Université du Maine	
Mabrouk BEN TAHAR	UTC	
Jean-Daniel CHAZOT	UTC	(Invited)
Emmanuel PERREY-DEBAIN	UTC	(Supervisor)
Benoît NENNIG	SUPMECA	(Co-supervisor)

I would like to dedicate this thesis to my loving parents ...

Acknowledgements

My deep and sincere gratitude goes firstly to my two co-directors of thesis, Emmanuel Perrey-Debain, Professor of Université de Technologie de Compiègne, and Benoit Nennig, Maître de Conférences of SUPMECA, for their generous support and insightful guidance during my research. They spent numerous hours and days with me for explaining all the aspects and details about this work. I have learned a lot from these enlightening and passionate discussions, not only the scientific knowledges but also the positive attitude towards research and life. It was really an honor to work with them.

I am also especially grateful to Jean-Daniel Chazot, Maître de Conférences of Université de Technologie de Compiègne, for his patience and continuous support. He also guided me through many scientific problems that I encountered during this work. I have acquired so many useful knowledges and techniques from him, I will always regard him as my third director of this thesis.

Special thanks goes to Professor Alexandre Leblanc and Professor Christian Prax who have agreed to review this dissertation and proposed a lot of precious suggestions, I also want to thank the other members on my doctoral committee: Professor Mabrouk Ben Tahar and Professor Oliver Dazel for their efforts and time to kindly participate in my final defense.

I also want to express my sincere gratitude to the whole acoustic team of laboratory of Roberval for their generous helps with my research during the my wonderful PhD period. They are: Profs. Jean-Michel Ville, Philippe Gatignol, Mohamed-Ali Hamdi, Nicolas Dauchez, Moreau Solène, and all the other doctors and PhD students: Lei, Nan, Romain, Antoine, Thibaut, Nicolas, Ryan, Florian, David, Saad, Yorick, Julien, Charles, Sebastian, Boureima... for the great time we have spent together.

Finally, I would like to dedicate this thesis to my parents and all my relatives and my best friends for your support and love in the past three years and eight months. The scholarship of the UT-INSA program funded by the China Scholarship Council (CSC) is also highly appreciated.

Abstract

Wave problems involving the medium and high frequency range have been receiving increased attention in recent years, a wide range of applications of short wave problems can be found in the various engineering fields. One of the most challenging problems in scientific computation is to achieve accuracy and efficiency simultaneously at high wavenumber. It has been acknowledged that conventional Finite element Method (FEM) and Boundary Element Method (BEM) are extremely demanding computationally to reach a good resolution of medium and high frequency wave problems. Therefore, some advanced deterministic prediction techniques with enhanced computational efficiency have been developed in recent years to overcome these shortcomings. Partition of unity finite element method (PUFEM) is one of the candidates among them.

PUFEM has great ability for dealing with short wave problems. The fundamental concept and the related formulations of the PUFEM are introduced in this work, and the numerical implementation of the plane wave enrichment in the finite element model are also explained in detail. In brief, the known physical feature of the propagating waves(a set of oscillatory wave functions satisfying the Helmholtz equation) are included into the approximation process of local element space. Then, we present two selection approaches of these plane waves, both the advantages and disadvantages of them are investigated.

We also focus on the computation of propagating sound fields in two dimensions with respect to PUFEM technique. As it will be discussed, the heavy computational cost resulting from numerical quadrature of non-polynomial shape functions poses a threshold in terms of efficiency of the PUFEM. Thereby, an Exact Integration Scheme (EIS) for 2D problems is presented and explained with all necessary details. This procedure allows us to significantly accelerate the computation of the system coefficient matrices and ease the computational burden. Finally, a numerical model of practical interest is set up for validation purpose. The efficiency of the numerical model developed in this chapter which combines PUFEM and EIS together will be assessed.

The full development of the PUFEM for 3D acoustical problems is presented and illustrated in this work. We propse the underlying theory of the Exact Integration Scheme (EIS) as well as the associated algorithm for 3D tetrahedron PUFEM element. Detailed analysis with regard to several numerical aspects of 3D PUFEM are conducted in this thesis, including error estimation, convergence rate and computational cost. A few numerical examples involving the response of a point source in a 3D cavities with or without porous material are implemented to validate and verify the PUFEM model combined with EIS. In the end of this work, PUFEM is extended further to simulate the acoustic waves in a porous material modeled as a equivalent homogeneous fluid. The numerical performances and efficiency are also analyzed in detail.

Table of contents

List of figures

List of tables

Chapter 1

Introduction

1.1 Wave background

The phenomenon of wave propagation can be captured and observed almost everywhere in our daily life, without it, we can not hear and appreciate the amazing world surrounding us. If we try to imagine the most impressive and vivid waves propagation phenomena, the first picture popping into our head probably might be water waves ranging from the small ripple caused by a stone thrown into river when we were little children, to the huge sea waves which are staggering enough to overturn the cruise ship in movies. Other people who love listening to the radio would be interested in the way of transmission of its signal which in fact is electromagnetic waves, electromagnetic waves cover a spectrum from low frequency radio waves, through visible light to X- and gamma rays. We can state that the sound wave, water wave, light wave and electromagnetic wave etc. constitute the most fundamental way of physical movement of nature.

The term wave enjoys various descriptions and definitions, several most appropriate ones can be attributed to: a pattern of matter or energy that is spread over a volume of space [125, 84] and a disturbance that carries energy from one place to another [34]. However, the definition of wave is not easily made, we usually choose to view them as a generic set of phenomena with many similarities [18]. Sincerely speaking, waves phenomena is amazing, while at the same time found to be abstract and elusive. More importantly, it is so close to our daily life so as to constantly arouse the interests of many famous mathematicians and physicians. Many of them have profoundly studied and put it into practice use in wide spread fields such as acoustics, non-destructive evaluation of materials, seismic analysis, electromagnetic and so on.

1.2 Numerical simulation of waves

The practical interest of studying wave propagation problems is its great influence in the domain of science and engineering, including aerospace engineering, civil and mechanical engineering to name a few. It is important to take advantage of wave properties and behaviors and then put them into practical use for the interests of human being and the whole of society. Although numerous challenges with regards to wave problems have already been recognized and some parts of it have been overcome since the $16th$ century when the mathematicians and physicians started to work on the mathematical models of wave, there still exists numerous difficulties waiting to be conquered for the scientists in our time. For example, the long range propagation wave problems, short wave problems and wave propagating in complex media are always viewed as challenging multi-scale problems both mathematically and numerically.

For the long propagation wave problems, we would think of underwater acoustics and ocean acoustic waves which are known to propagate over several thousand kilometers. The corresponding practical remote sensing applications would also cross our mind, such as ocean current measurement, early warning system for Tsunamis and oil spills, remote surveillance [3, 11]. For instance, a devastating Tsunami caused by a underwater earthquake with a big magnitude occurred in the near sea of Japan in 2011, resulting in a destruction of the eastern coastline of Japan, where thousands of building collapsed and lead to more than $20,000$ people dead and missing. The Tsunamis even reached Hawaii's coastline which is located $6,400$ kilometers from its epicenter after several hours. Therefore, the study of long propagation wave problems definitely becomes valuable for the sake of our interest. In essence, the characteristic of all the long distance transmission problems is that their traveling distances of wave are always several orders of magnitude larger than their wavelength, which consequently brings about the issue that too many wavelengths will be contained in numerical models for the studying purpose.

The wave problem concerned with medium and high frequency range receives increasing attention in recent years. With the continuous development of computational hardwares and facilities as well as the advanced numerical techniques, the studying range of wave frequency has been continuously extended. However, the difficulty of simultaneously achieving accuracy and efficiency at high wavenumber has still been cited as one of the most challenging problems in scientific computation [129]. We can find many applications of short wave problems in medical image field, which mainly take advantage of ultrasonic waves with frequencies ranging from 1 MHz to 15 MHz. For the wave speed $c = 1500$ m/s, the average wavelength is varying from 1.5 mm to 100 microns. Another example could be a radar wave

scattered by an aircraft, the ratio between the radio wavelength and the size of aircraft could reach several thousands. In addition, we know the thumb rule for the wave simulation is that at least seven to ten nodal spaces per wavelength are required to achieve a certain level of accuracy. As a result, it's not hard to imagine that the density of the mesh grid required for the simulation of high frequency waves issues would definitely lead to remarkable computing loads and resources.

1.3 Low-frequency methods

The fundamental questions related to the existence and uniqueness of solutions to the Helmholtz problems were solved by the end of the 1950's, these results accomplished by several authors [63, 31] underly the most basic theories for the developments of numerical analysis and methods in acoustical domain. Because of that the general analytical solutions [98, 96, 20, 59] for wave problems are always limited to the idealized geometries and homogeneous domains, we have to develop much more advantageous and flexible methods to predict the dynamic field solutions in problems involving heterogeneous materials, complex geometries and different kinds of nonlinearities.

The most widely adopted numerical methods for simulating low-frequency waves belong to the Finite Element Method (FEM) and the Boundary Element Method (BEM). Both methods use very dense partitioning mesh and small elements to discretize the dynamic field variables. So basically, they share both the specific advantages and disadvantages of the element-based approach. But they also possess different capabilities and properties for modeling various kinds of acoustical problems. In the following, we will discuss these principles and properties in more detail.

1.3.1 Finite Element Method (FEM)

The development of FEM for time-harmonic wave problems governed by the reduced wave equation (Helmholtz equation), have been constantly regarded as an active and important research area for almost 50 years. Initial applications of Finite Element Methods on interior problems with complex geometries including direct and modal coupling of structural acoustic systems for forced vibration analysis, frequency response of acoustic enclosures, and waveguides [49, 33, 52, 99, 106, 128]. Considering that the FEM is based on a discretization of the entire problem domain into large but finite number of small elements, it has no ability to inherently handle unbounded problems. As a solution, an artificial boundary around the

region of interest have to be introduced to truncate the unbounded problem into an equivalent bounded problem. Different techniques are then required to reduce spurious reflection of waves at the truncation boundary to a level below that of the discretization error. There exists three main strategies to solve this problem [119]: absorbing boundary conditions [13, 56], infinite elements [16] and absorbing layers [14]. Review papers on the broader subject of absorbing schemes include those of [51, 55, 120]. Although the introduction for the unbounded field will exert some additional complexities on the simulating process, the FEM has a lot of numerical advantages which can make it an efficient technique:

- The system matrix is composed of a real and sparse mass and stiffness matrix, and additionally a damping matrix which in some cases shares the same properties. In the case of uncoupled acoustic problems, the matrices are also generally symmetric. Moreover, the matrices are mostly frequency-independent, saving time in system construction. Besides, the construction of those matrices only requires evaluation of simple integrals involving polynomial functions. These advantageous properties allow for an easy and fast construction of the system matrices. The specific matrix structure can also be exploited in highly optimized solvers to yield a fast solution of the FE system.
- The FE method was developed with the aim of discretizing geometrically complex structures. The necessary use of a large number of small elements allows to represent any arbitrary geometry without particular effort, thus giving the method a great geometrical flexibility.

The good performance and flexibility of the FEM make it a popular numerical technique, especially, for low-frequency bounded problems. However, it also suffers from some inherent shortcomings when we aim at solving higher frequencies and unbounded problems:

- The use of simple low-order polynomial shape functions could lead to the substantial approximation errors. We can find extensive error analysis with regards to this topic and two main types of error are indicated in the work of [21, 69], the first type is *Interpolation errors* resulting from the fact that the exact dynamic field is inevitably different from the approximating field which usually consists of piecewise polynomials. The second type is known as the *Pollution errors* or phase errors resulting from the over- or underestimation (depending on the FE formulation) of the physical wavelength by the FE model. The pollution effect is related to the loss of stability of the Helmholtz operator at large wave numbers. This results in a frequency shift in the calculated results with respect to the exact solution of the problem.

- The FEM is not capable of inherently dealing with unbounded problems. In order to use the FEM on unbounded domains, an artificial surface have to be introduced, on which some specific boundary conditions are applied to prevent spurious wave reflections. The application of the these boundary techniques presents an additional burden. Moreover, most of those techniques yield different matrix properties to the standard FEM, rendering the system complex, and additionally resulting in a possible loss of the sparse or symmetric characteristics, deteriorating the performance of dedicated solvers.

1.3.2 Boundary Element Method (BEM)

As another popular element-based technique for solving acoustic problems, BEM [22] has the ability to model unbounded problems without the need for considering the artificial truncation or extra simulating process because the problem is reduced to a formulation depending merely on the boundary. The BEM has been used to solve exterior acoustic problems for many years [32, 92, 118]. To be more specific, the assets of the BEM are:

- Thanks to the boundary integral formulation, BEM enjoys the popularity when it comes to solve wave problems for unbounded homogeneous media [26, 29, 30, 83, 127]. It only requires the discretization of the boundary of the region of interest and automatically satisfies the radiation condition at infinity [115].

- Although the assembled system matrices in the finite element formulation can be evaluated very easily due to their sparse structure, the numerical restriction arising from tremendous number of unknowns in FEM will still hamper the application of FEM in many cases. In contrast, BEM for the Helmholtz problems benefit from the advantage of one dimension fewer than FEM (e.g. only a 2D mesh for a 3D problem), and BEM model generates consistently smaller system matrices involving much less degrees of freedom.

- The boundary of the domain is discretized using elements which is analogous to the finite elements. Also for the BEM, the elements have to be small enough in order to satisfy the necessary accuracy of simulation results. Therefore, the BE mesh is able to model any geometrical domain of the model without additional procedures, leading to a robust and flexible method.

The above-mentioned properties make BEM a competitive and efficient method when dealing with unbounded wave problems. However, the BEM also has its drawbacks:

- Even though the system matrices of BEM are normally much smaller than the counterpart of FEM, they are fully populated, non symmetric and contain complex entries in most cases. These disadvantageous properties severely limit the applicability of optimised solvers.
- BEM in acoustics is based on the use of boundary integral equations (BIE) which are known to suffer from non-uniqueness difficulties at certain characteristic frequencies (or wavenumbers) for unbounded problems, and lead to a possible loss of accuracy around these frequencies. Special treatments can be made to mitigate this issue, but at the cost of more computational load and lower efficiency.
- BEM is not suitable for dealing with wave propagation in heterogeneous media.

1.4 Medium and high-frequency deterministic methods

Through the above discussion concerned with the disadvantages of FEM and BEM, we are aware of the fact that classical low-frequency methods are not sufficient enough to reach a good resolution of short wave problems due to the approximation and pollution errors. As a consequence, a huge amount of degrees of freedom would be required, if we want to ensure a certain level of accuracy. Let us consider a high frequency scattering problem at 1133 Hz from a cubic shaped obstacle with a lateral surface of 0.24 m $\times$ 0.24 m, the wavelength is 0.03m in the air (with $c = 340$ m/s). If we adopt a discretization level of ten nodes per wavelength to approximate the dynamic field, then at least 48 nodes along each side of the cube are needed, indicating that around 14000 finite elements are necessary on the surface of the cube. In this case, even though we could afford the high demand of computing resources such as CPU and memory and use an efficient iterative solver for high frequency scattering [85], the dispersion error problem would be largely accumulated during the approximation process in FEM [69], thus, leading to unreliable results and uncertainty analysis.

To overcome these shortcomings of conventional FEM, new deterministic prediction techniques have been developed in recent years through the process of expanding the dynamic field solution with wave functions that capture the oscillating character of the waves. For the Helmholtz equation, such wave functions generally take the form of plane, circular or spherical waves. These developments have given rise to different numerical methods which allowed to tackle medium and high frequency problems. This includes:

- Partition of Unity Finite Element Method (PUFEM),

- Wave-Based Method (WBM),
- Variational Theory of Complex Rays (VTCR),
- Ultra Weak Variational Formulation (UWVF).

1.4.1 PUFEM

PUFEM can be classified into the category of the meshless methods because it possesses the ability to include $apriori$ knowledge about the local behavior of the solution into the finite element space, underlying the major difference between traditional finite element method and PUFEM. With this property, PUFEM possesses the overwhelming advantage over the traditional FEM in terms of the computational cost, the complexity of the resulting numerical model and the adaptivity of the finite element space when handling medium and high frequency problems. The concept of PUFEM was firstly proposed by Melenk in his PhD thesis "On Generalized Finite Element Methods" [88] in which the mathematical background related to this technique was introduced and explained. Melenk and Babuška further extended this work into two most fundamental papers of PUFEM [90, 9] where a proof of convergence was given and some numerical tests were illustrated. Similar to their work, Mayer and Mandel [86] proposed a finite ray element method to solve the Helmholtz equation.

Laghrouche et al. [77, 78] took advantage of the PUFEM to solve wave scattering and diffraction problems in 2D. The finite element space in their model was approximated and expanded through a set of plane wave basis with carefully chosen propagation directions. The method was implemented for the purpose of solving several short wave problems, showing a great reduction of degrees of freedom compared with the traditional FEM. The application of the method was further extended to 3D problems by Laghrouche et al. [79] and Perrey-Debain et al. [105]. In their work, a 3D plane wave basis finite element model was developed and validated for the specific problem of a incident plane wave scattered by a rigid sphere. Later, the method of PUFEM was further developed to cope with more complex problems in which the wave speed is discontinuous [80].

Kacimi and Laghrouche [71, 73] studied both the L^2 error and conditioning behavior of the PUFEM with respect to the mesh size, frequency and the number of approximating plane waves. Mohamed et al. [93] pointed out the influence of the geometry on the numerical errors, and showed that the conjugated formulation performs better than the unconjugated one when odd numbers of plane waves are considered in the basis. Laghrouche and Mohamed [81] investigated the convergence behavior of PUFEM, and their analysis showed that both

h-refinement (i.e. by reducing the size of the mesh grid) and q-refinement (i.e. by increasing the number of approximating plane waves) lead to fast convergence rates. In this regard, the q-refinement was shown to perform better.

A new PUFEM model for solving acoustic propagation problems in non-uniform potential flows was proposed by Gamallo and Astley [47]. They achieved this purpose by enriching the solution space with plane waves in which the wavenumber is a function of the Mach number. The results showed the good performance of the method. In their second paper [91], the Partition of Unity Method was coupled to infinite elements based on the Astley–Leis conjugated formulation to deal with convected wave propagation in axisymmetric unbounded domains. Two specific applications concerning propagation in ducts and the radiation of a dipole have been analyzed in order to validate and show the advantages of the proposed method compared to classical FEM discretization.

1.4.2 Wave Based Method

The Wave-Based Method (WBM) was put forward by Desmet in his PhD dissertation [39] as an indirect Trefftz method. It is a deterministic prediction technique to solve steady-state dynamic problems and has the ability to handle the frequency limitations problems encountered in the traditional element-based prediction method. It has been successfully applied for acoustic [57, 15], equivalent fluid [82], uncoupled elastic [121, 122] and fully coupled vibro-acoustic problems [108, 107]. The fundamental theory of this approach relies on using a weighted sum of wave functions which are exact solutions of the governing partial differential equations, to approximate the dynamic field variables. This approach results in a smaller system of equations and enjoys a higher convergence rate and lower computational loads in comparison to conventional finite element prediction techniques. The disadvantage of the method becomes evident when complex geometrical features are involved. The geometrical complexity has to be moderate to obtain efficient solutions, because otherwise a subdivision into a large number of convex sub-domains is required or may even be impossible for some configurations. We can cite two recently developed approaches aimed to relax these limitations: a multi-level modeling framework allows the WBM to efficiently tackle configurations with complicated multiple scatterers or inclusions [48, 50] and a hybrid FE-WBM formulation was developed to handle complicated domains [49].

Deckers et al. [37] investigated the vibro-acoustic behavior of poroelastic materials by formulating the material as boundary value problems based on the Biot's theory. Exact solutions of the three coupled waves supported by Biot's equations are adopted as the basis

functions in the solution expansion process to approximate the wave field. As a result, more computationally efficient solutions of the Biot's equations can be achieved. Considering the limitation of the WBM in terms of geometry, Bert Jonckheere et al. [70] developed an hybrid simulation technique for coupled structural acoustic analysis. The idea of this technique is to apply a wave based model for the acoustic cavity while using a direct or modally reduced FEM model for the structural part, so that the whole hybrid model can benefit from the computational efficiency of the WBM, and at the same time, be capable of taking many more complex geometries into account. The authors showed that this hybrid method can be regarded as a powerful tool for analyzing structural-acoustic systems in the mid frequency range. WBM was also further developed for the analysis of time-harmonic three-dimensional interior acoustic problems by Vergote et al. [123]. Numerical tests showed computational efficiency for simulating acoustic waves in both damped and undamped cavities. Also, an empirically derived general guideline for determining the required number of wave based approximation functions was presented.

1.4.3 Variational Theory of Complex Rays

The Variational Theory of Complex Rays (VTCR) was introduced in Ladevèze [75] which is designed to calculate the vibrational response of structures in the medium-frequency range. The capability of this strategy has already been demonstrated in several works, including 3-D plate assemblies in [113], for plates with heterogeneities in [76] and for shells in [111]. Its extensions to acoustics can be found in reference [112]. The VTRC relies on a special weak formulation of the problem which makes the approximations within the substructures *a priori* independent of one another. Thereby, any type of wave function can be used in a substructure provided that it satisfies the governing equations. This gives the approach great flexibility and makes it very efficient. All the wave directions are taken into account and their amplitudes become the new unknowns of the problem. This method leads to a small system of equations which, contrary to element-based methods, does not result from a refined spatial discretization.

1.4.4 Ultra Weak Variational Formulation

The original concept of Ultra Weak Variational Formulation (UWVF) was introduced in the 1990's by Cessenat and Després in [23, 24]. Since then it has received remarkable attention and has been applied to numerous PDEs and BVPs. The first basic idea of UWVF is to divide the domain of interest into a set of sub-domain or elements, of which the inter-element continuity is imposed through a modified variational formulation applied on the boundary

interface between two sub-domains, yielding a weak impedance-type continuity. Second, alike to the former strategies, UWVF incorporates the $apriori$ analytical solutions of the considered PDEs into its trial functions. Later on, UWVF was regarded as an unusual version of the standard upwind discontinuous Galerkin (DG) method [66].

It has been proposed as an effective method for solving Helmholtz problems with high wavenumber. Huttunen et al. [68] considered the computational aspects of the ultra-weak variational formulation for the inhomogeneous Helmholtz problem. They introduced a method to improve the UWVF scheme and compare iterative solvers for the resulting linear system, they also considered a nonuniform number of basis functions per element to improve the conditioning of the resulting matrix system. Other papers investigated several relevant computational aspects of the UWVF: [65] showed how to implement the PML in the UWVF to accurately approximate physically unbounded problems and discuss the parallelization of the UWVF, the comparison with other wave-based schemes (e.g. PUFEM and least squares) are conducted in the references [45, 46, 64]. Furthermore, the UWVF has been used to couple Trefftz and polynomial trial spaces on different elements in [94], this is a very promising direction showing that the method can be employed to tackle realistic problems. Finally, three-dimensional numerical simulations are performed in [67] to examine the feasibility of the UWVF for simulating wave propagation and scattering in inhomogeneous media with complex structures.

1.5 The development of Exact Integration Scheme (EIS)

The above-introduced wave-based prediction techniques always accompany the highly oscillatory integrals, which renders the numerical calculation of the matrix coefficients very challenging. High computational cost will emerge if we follow conventional numerical integration using high order quadrature schemes such as the classical Gauss-Legendre quadrature. The root cause lies in the fact that too many integration points will be involved in the process of computing the system matrices. For instance, up to 120 by 120 integration points were used in the work [78] to evaluate element matrices when solving a wave scattering problem in 2D. Thus, a nature extension in 3D would involve approximately $120^3 = 1,728,000$ integration points per finite element! To mitigate this issue, the exact integration schemes have been proposed which are capable of largely reducing the computational cost.

Sugimoto et al. [117] used a semi-analytical approach to integrate the oscillatory functions in a straight edged quadrilateral finite element. Ortiz and Sanchez [101] used triangular

elements and performed a coordinate transformation by rotating the local coordinate system so that the oscillatory kernel varies only in a singe direction. In another approach, Gordon [54] used the divergence theorem to integrate exactly an oscillatory function over a polygon. This approach reduces the surface integral to a line integral over the polygon boundary, which can in turn be evaluated at the vertices over the polygon edges provided that they are straight lines. Kacimi and Laghrouche [72] developed a similar explicit closed-form solution for two-dimensional wave-based integrals The fundamental theorem behind their scheme is to take most advantage of the Green's theorem to reduce the integration dimensions. It was shown that the proposed integration scheme allows to evaluate accurately the entries of the system matrix with drastic reduction of the computational time. Similar to their work, a set of closed-form solutions for the integrals involving product of polynomial and exponential functions in two and three dimensions was proposed by Gabard [43]. These results apply to arbitrary polygons in two dimensions, and for arbitrary polygonal surfaces or polyhedral volumes. Quadrature methods are therefore not required for this class of integrals that can be evaluated quickly and exactly.

1.6 Overview of this thesis

In Chapter I, we have surveyed and presented the background and significance of waves, and reviewed the prior work in the field of numerical simulation. Advanced numerical schemes for solving short wave problem have been discussed.

In Chapter II, we present the fundamental concept of the PUFEM and introduce the basic PUFEM formulation for the acoustical wave propagation problem in a bounded domain. Also, the numerical implementation of the plane wave enrichment in the finite element model is explained in detail.

In Chapter III, we focus on the computation of sound fields in two dimensions using the PUFEM technique. The heavy computational cost resulting from numerical quadrature of non-polynomial shape functions force us to develop an Exact Integration Scheme (EIS) for 2D problems, all necessary details are presented and explained.

In Chapter IV, the full development of the PUFEM for 3D acoustical problems is presented. Several critical aspects of the method are investigated in detail.

In Chapter V, we concentrate on the application of the PUFEM element combined with

EIS for the analysis of interior sound field problems where absorbers are present. In particular, the PUFEM is extended to simulate the propagation of acoustic waves in a porous material.

In Chapter VI, the main conclusions and contributions of this dissertation and a discussion of potential avenues for future research are presented.

Chapter 2

The PUFEM applied to the Helmholtz equation

The aim of this chapter is to present the fundamental concept of the PUFEM and introduce the basic PUFEM formulation for the acoustical wave propagation problem in a bounded domain. Also, the numerical implementation of the plane wave enrichment in the finite element model is explained in detail. The whole structure of this chapter is organized as follows:

In Section 2.1, we present the linear wave equation and the boundary conditions as well as the associated weak formulation. Section 2.2 briefly recaps the classical finite element discretization process. Section 2.3 is devoted to illustrate the plane wave enrichment process, and the selection methods with regard to the wave directions for 2D and 3D problems. In Section 2.4, we investigate the inherent properties of the PUFEM coefficient matrices. Some other basis functions for PUFEM are also discussed in Section 2.5. Finally, we draw some conclusions in Section 2.6.

2.1 Variational formulation and boundary conditions

The basic formulations of linear time-harmonic acoustics are first derived through the use of two fundamental laws of the theory of continuum mechanics. They are, respectively, the principle of conservation of mass and the principle of balance of momentum. Under the assumptions that we are only dealing with small perturbations of ambient quantities, and only ideal gases with constant temperature are considered to ensure an adiabatic process, we

can easily derive the classical wave equation for the pressure p:

$$\Delta p - \frac{1}{c^2}\frac{\partial^2 p}{\partial t^2} = 0, \tag{2.1}$$

where, c is the sound wave speed in the medium, which is constant. This wave equation is valid for the sound pressure but it may also apply to the velocity potential. For the time harmonic wave oscillation problem, where time-dependence $p(\boldsymbol{x}, t) = p(\boldsymbol{x})\mathrm{e}^{-\mathrm{i}\omega t}$ is assumed, the homogeneous Helmholtz equation for the acoustic pressure in a bounded domain Ω thus becomes

$$\Delta p + \kappa^2 p = 0 \qquad \text{in } \Omega, \tag{2.2}$$

where $\kappa = \frac{\omega}{c}$ is the wavenumber and ω is the angular frequency. In order to get a solution, it's imperative to provide the boundary conditions for this partial differential equation. We can write different types of local boundary condition in a compact form as follows

$$(1+Q)\frac{\partial p}{\partial n} + (Q-1)\mathrm{i}\kappa p = g \qquad \text{on } \Gamma. \tag{2.3}$$

Apparently, the Dirichlet boundary is recovered when $Q = -1$, and the Neumann boundary corresponds to $Q = 1$. Here, g denotes an imposed source term on the boundary. This boundary condition equation associated with the Helmholtz equation allow us to define a unique sound pressure field p (except when $|Q| = 1$, to avoid cavity's resonant frequencies). Applying the standard weighted residual scheme to the governing equation, we can write

$$\int_\Omega \delta p(\Delta p + \kappa^2 p)\mathrm{d}\Omega = 0, \tag{2.4}$$

where δp stands for the weighting function. It's worth mentioning that the choice of this function is not unique. Among them, the Galerkin method which is probably the most common approach adopted in the finite element community, consists in choosing the weighting function to be identical to the trial basis function. The reason of its popularity among others stems from the fact that this selection allows the fast construction of a symmetric linear system.

By applying integration by parts, we can reduce the order of derivative from Laplace operator to the calculation of gradients for both weighting and trial functions. Consequently, the weak form of the Helmholtz equation becomes

$$\int_\Omega \left(\nabla p \cdot \nabla(\delta p) - \kappa^2 p \delta p\right)\mathrm{d}\Omega - \int_\Gamma \frac{\partial p}{\partial n}\delta p \mathrm{d}\Gamma = 0, \tag{2.5}$$

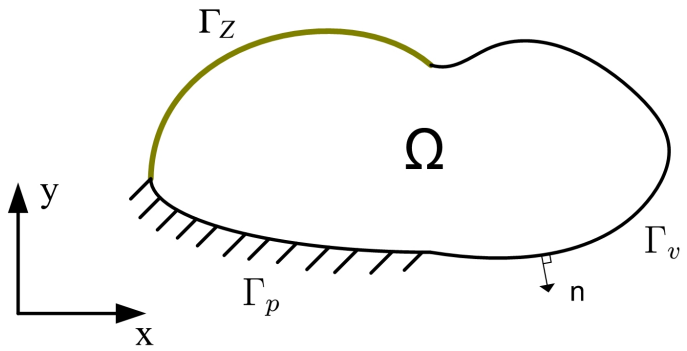

Fig. 2.1 General acoustic domain with different types of boundary condition.

where Γ is the boundary of Ω. The second integral term contains the boundary conditions expressed in (2.3). For the sake of illustration, Figure 2.1 shows an example of an interior acoustic problem with a closed boundary $\Gamma = \Gamma_p + \Gamma_v + \Gamma_Z$ surrounding the fluid domain Ω, in which we let Γ_p represent the Dirichlet boundary, and Γ_v and Γ_Z represent the Neumann and Robin type boundary conditions, respectively. In the following, in order to simplify the presentation, we shall consider a particular Robin type boundary condition with $Q = 0$ in (2.3), which gives rise to

$$\frac{\partial p}{\partial n} - \mathrm{i}\kappa p = g \qquad \text{on } \Gamma. \tag{2.6}$$

The associated weak form of the Helmholtz equation to be solved becomes

$$\int_\Omega \left(\nabla p \cdot \nabla(\delta p) - \kappa^2 p \delta p\right) \mathrm{d}\Omega - \mathrm{i}\kappa \int_\Gamma \delta p \cdot p \, \mathrm{d}\Gamma - \int_\Gamma \delta p \cdot g \, \mathrm{d}\Gamma = 0. \tag{2.7}$$

Note that the integrand terms appearing in the above equation have to satisfy a certain requirements of continuity (smoothness) across interfaces between elements (conventionally termed as compatibility condition). This indicates that the selected trial and test functions p and δp of the field variable must have the derivatives up to the order $n-1$ inside and between the elements, where n is the highest derivative of the integrand terms involved in the weak formulation. In other words, the trial functions p must have the continuity of C^{n-1} between interconnected elements, and also be C^n piecewise differentiable inside each element. Under this circumstance, we can say that the discrete function in the above weak form equation should be continuous everywhere.

Besides, boundary condition (2.5) becomes more complicated when we deal with the numerical problems involving wave propagation in porous materials. Special treatments must be followed in order to satisfy the continuity conditions between the two domains. This shall be explained and discussed in Chapter 5.

2.2 Classical finite element discretization

The enriched finite element encountered in the context of PUFEM can be viewed as an generalization or extension of the traditional finite element method, so in this section we briefly review the classical process of FE discretization. The core idea of the finite element method is to partition the domain of interest into a set of elements, then to approximate the physical field by a discrete method to establish the finite element space. The trial functions which are largely used in the finite element community generally consist of piecewise polynomials ranging from low order functions (e.g., hat function shown in Figure 2.2) to high order functions (e.g., spline function). The convergence rate greatly depends on the choice of these trial functions.

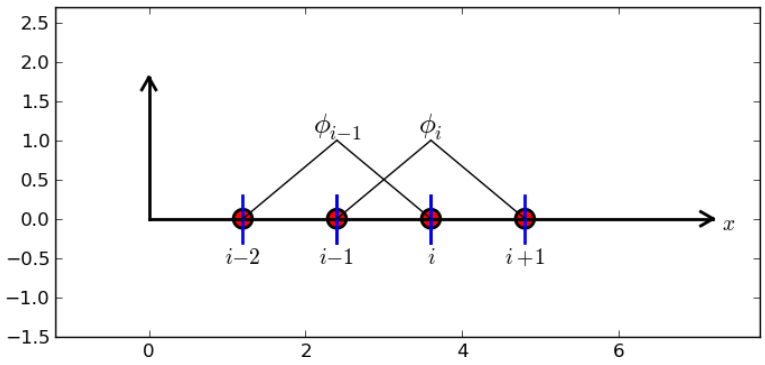

Fig. 2.2 Low order hat function is chosen to be the trial function for 1D problem.

The whole sound field domain is partitioned as $\Omega = \bigcup_{e=1}^{N_{el}} \Omega_e$, in which N_{el} denotes the number of partitioned element of the whole domain, and the sound pressure field in each element Ω_e in the computational domain can be approximated in the form of

$$p(\boldsymbol{x}) = \sum_{j=1}^{n} N_j(\boldsymbol{x}) p_j = \mathsf{N}^{\top}\mathsf{p}, \tag{2.8}$$

in which N_j is the classical Lagrangian shape function with regard to the j^{th} node of the element, and all shape functions are linearly independent. Here, n stands for the number of nodes, for example, $n = 3$ refers to the classical triangular element for 2D problems, and $p_j = p(\boldsymbol{x}_j)$ represents the value of the pressure at node position $\boldsymbol{x}_j$. As a consequence, if we substitute the interpolation (2.8) for the test and trial functions in equation (2.7), we can

finally arrive at a finite system of equations:

$$\begin{aligned}\sum_{e=1}^{N_{el}} \int_{\Omega_e} \left\{ \nabla N_i(\boldsymbol{x}) \cdot \nabla \left[\sum_{j=1}^{n} N_j(\boldsymbol{x}) p_j \right] - \kappa^2 N_i(\boldsymbol{x}) \left[\sum_{j=1}^{n} N_j(\boldsymbol{x}) p_j \right] \right\} \mathrm{d}\Omega_e(\boldsymbol{x}) \\ = \mathrm{i}\kappa \int_{\Gamma} N_i(\boldsymbol{x}) \left[\sum_{j=1}^{n} N_j(\boldsymbol{x}) p_j \right] \mathrm{d}\Gamma(\boldsymbol{x}) + \int_{\Gamma} N_i(\boldsymbol{x}) g(\boldsymbol{x}) \mathrm{d}\Gamma(\boldsymbol{x}).\end{aligned} \tag{2.9}$$

For the purpose of clarity, we introduce element mass matrix $\mathsf{M_e}$ with entries m_{ij}^e given by

$$m_{ij}^e = \int_{\Omega_e} N_i(\boldsymbol{x}) N_j(\boldsymbol{x}) \mathrm{d}\Omega_e(\boldsymbol{x}), \tag{2.10}$$

the element stiffness matrix $\mathsf{K_e}$ with entries k_{ij}^e given by

$$k_{ij}^e = \int_{\Omega_e} \nabla N_i(\boldsymbol{x}) \cdot \nabla N_j(\boldsymbol{x}) \mathrm{d}\Omega_e(\boldsymbol{x}), \tag{2.11}$$

and the element matrix $\mathsf{C_e}$ with entries c_{ij}^e given by the boundary terms is

$$c_{ij}^e = \int_{\Gamma_e} N_i(\boldsymbol{x}) N_j(\boldsymbol{x}) \mathrm{d}\Gamma_e(\boldsymbol{x}). \tag{2.12}$$

Then the load vector $\mathsf{b_e}$ is given by

$$b_i^e = \int_{\Gamma_e} N_i(\boldsymbol{x}) g(\boldsymbol{x}) \mathrm{d}\Gamma_e(\boldsymbol{x}). \tag{2.13}$$

Consequently, through the assembly of all the contributions from element matrices, the system of equations can be written in the following matrix form

$$[\mathsf{K} - \kappa^2 \mathsf{M} + \mathrm{i}\kappa \mathsf{C}]\mathsf{x} = \mathsf{b}. \tag{2.14}$$

Here, the unknown vector x contains the nodal values for the acoustic pressure. The above equations system can be further written in a more compact form

$$\mathsf{A}\mathsf{x} = \mathsf{b}. \tag{2.15}$$

The accuracy of FEM results depends not only on the discretization level which refers to the refinement of the mesh, but also on the order of polynomial functions used to approximate the field variables. In the context of FEM, there exists two primary approaches to improve the accuracy of simulation results. On one hand, we can use the refinement of the computational mesh, which can be briefed as h-refinement. On the other hand, it is also feasible to meet the

requirement of the accuracy level through the enhancement of the order n of approximating polynomials (sometimes called p-refinement). The performances of both strategies, or the two combined (hp-refinement) can be found in the work of Babuška and Guo [7] and Melenk [89].

However, when it comes to medium and high frequency problems, the usually adopted 'ten nodes rule per wavelength' becomes insufficient to maintain the same accuracy level. This phenomenon which is linked to the indefiniteness of the Helmholtz operator and originally derived by Garding's inequality [12], is also known as *pollution effect* in [38, 8]. In essence, this comes from the phase difference between the simulated wave and the exact wave with increasing wavenumber κ, resulting in that the wavenumber of the FEM solution becomes different from the counterpart of the exact solution. It has been proved by Babuška and Sauter [10] that the pollution error cannot be avoided in two and three dimensions when classical FEM is employed. Due to this inherent numerical shortcoming, we have to use some other advanced numerical prediction techniques not influenced by the pollution effect. PUFEM is one candidate among them.

2.3 Plane wave enrichment for PUFEM

As we introduced in Chapter one, the PUFEM is recognized as a general approach for enhancing the numerical solution of partial differential equations. It provides a framework for incorporating part of the analytical solution of the PDEs in the shape function. Plane waves are usually selected to be the expansion basis for the sake of their convenience. More precisely, the starting point of PUFEM is to consider, for each node j, the following plane wave expansion

$$P_j(\boldsymbol{x}) = \sum_{q=1}^{Q_j} A_{jq} \exp(\mathrm{i}\kappa \boldsymbol{d}_{jq} \cdot (\boldsymbol{x} - \boldsymbol{x}_j)), \tag{2.16}$$

where, P_j is a function of $\boldsymbol{x}$ and consists of a set of Q_j plane wave directions. In order to better explain this plane wave enrichment process of PUFEM, Figure 2.3 depicts an two-dimensional enriched finite element of PUFEM where four plane wave directions are considered at each node of this element. It can be seen that they are indicated by four red arrows, namely $Q_j = 4$. Moreover, A_{jq} stands for the amplitude of each plane wave attached to the j^{th} node, which is now viewed as the new unknown of the equations system. And $\boldsymbol{d}_{jq}$ denotes the wave directions of the plane wave basis applied on the j^{th} node of the enriched element. It's also worth noting that the node $\boldsymbol{x}_j$ appears in (2.16) in order to:

- ensure that the nodal values can be recovered simply as

$$P_j(\boldsymbol{x}_j) = \sum_{q=1}^{Q_j} A_{jq}, \tag{2.17}$$

- avoid the round-off error due to the computation of the exponential function when the wavenumber κ is complex.

The fully discrete sound pressure field of the PUFEM is found by replacing the nodal value p_j in (2.8), which yields

$$p(\boldsymbol{x}) = \sum_{j=1}^{n} N_j P_j(\boldsymbol{x}). \tag{2.18}$$

Here, particular attention must be paid to the interpolation functions N_j. They are usually chosen to be of very low order in PUFEM due to the fact that the exponential wave functions are already sufficient to capture the oscillating behavior of the wave field. So in this work, we will focus on the lowest order: $n = 3$ in 2D and $n = 4$ for 3D problems.

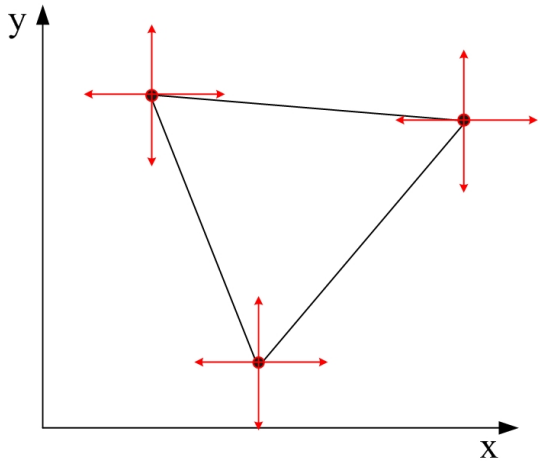

Fig. 2.3 Enriched triangle finite element with 4 plane waves attached to each node.

2.3.1 Selection of the plane waves in 2D

For 2D numerical models, the distribution of the plane wave directions is regularly based on the equal spacing of points on the unit circle, as shown in Figure 2.4. So the wave directions can be formally expressed as $\boldsymbol{d}_{jq} = (\cos(\theta_q), \sin(\theta_q))$, where

$$\theta_q = \frac{2\pi q}{Q_j} \qquad \text{and} \quad q = 1, ..., Q_j. \tag{2.19}$$

It's worth mentioning again that, in classical FEM, the discretization level of finite element space is determined by the h or p-refinement associated with mesh partitioning. However, the discretization level for all wave based methods is mainly dependent on the number of plane wave directions Q_j. For instance, the triangular element in the FEM possesses three degrees of freedom (dof), while the enriched finite element in PUFEM, shown in Figure 2.3, has $3 \times 4 = 12$ number of unknowns. Since we know that at least 10 nodal points per wavelength are required in conventional FEM, it is necessary to set up a similar criteria for the purpose of evaluating the number Q_j in the plane wave enrichment.

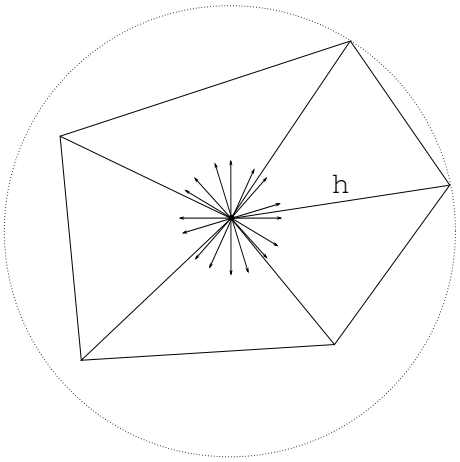

Fig. 2.4 Distribution of plane wave directions in a 2D mesh.

This parameter determines the size and structure of the system matrix which also exert the direct influence on the overall computational costs. In this regard, some research work has been carried out by several authors. Huttunen et al. [68, 64] used nonuniform plane wave basis functions to enhance the applicability of the UWVF with varying element sizes. Vergote et al. [123] proposed an empirical formulation for selecting the number of bending wave functions for plate vibration problems. Hence, we can make the conclusion that the number of plane waves depends mainly on the size of the PUFEM element and the wave frequency. The criteria taken from [64] is adopted to provide a good estimate in 2D:

$$Q_j = \text{round}[\kappa h + C(\kappa h)^{1/3}]. \tag{2.20}$$

Here, h is taken as the longest edge connected to node j, which is specified in Figure 2.4. The constant C can be regarded as a coefficient that usually lies in the interval $C \in [2, 20]$ as indicated in [27]. The value of this coefficient can be adjusted according to the configuration and the expected accuracy that we want to achieve. It has been observed that this number Q_j grows mildly with frequency. For 3D problems, it is found that the choice of number of

plane waves still relies on the wavenumber and the element size as in (2.20), except that the selection criteria for 3D problems is different, and we will address this problem in detail in Chapter 4.

2.3.2 Selection of plane waves in 3D

For 3D problems, the 3-node triangular element becomes a 4-node volume element and the boundary Γ in (2.5) is made of triangular surfaces. It turns out that the wave directions $\boldsymbol{d}_{jq}$ in (2.16) are no longer equally distributed over a unit circle (Figure 2.4), but rather spaced uniformly over a spherical surface, see Figure 2.5. Although this purpose can be achieved through several methods in [41, 53, 95, 114], the involvement of a large number of plane wave directions still poses a great challenge. In this work, we take the Coulomb force method developed by Peake et al. [103] as a solution, it is based on the use of an explicit time stepping scheme to converge to a static equilibrium state for a set of charged particles on a unit spherical surface. In the following, the basic theory about Coulomb force method is introduced, and a dedicated program has been realized in Matlab.

Let us consider a set of particles randomly located on a sphere of unit radius at positions indicated by vectors $\boldsymbol{U}_i$, $i = 1, 2, ..., Q$. Each of these particles has unit mass and unit electrical charge so that they repel each other with Coulomb forces varying like $1/\left|\boldsymbol{r}^2\right|$, where $\boldsymbol{r}_{ij} = \boldsymbol{U}_i - \boldsymbol{U}_j$. The initial setting for the position vectors of all the particles is set as $\boldsymbol{U}_i^0$, the superscript denotes the initial time step when the force begins to act on. The Coulomb force vector $\boldsymbol{F}_i$ at time step t is, therefore, given by

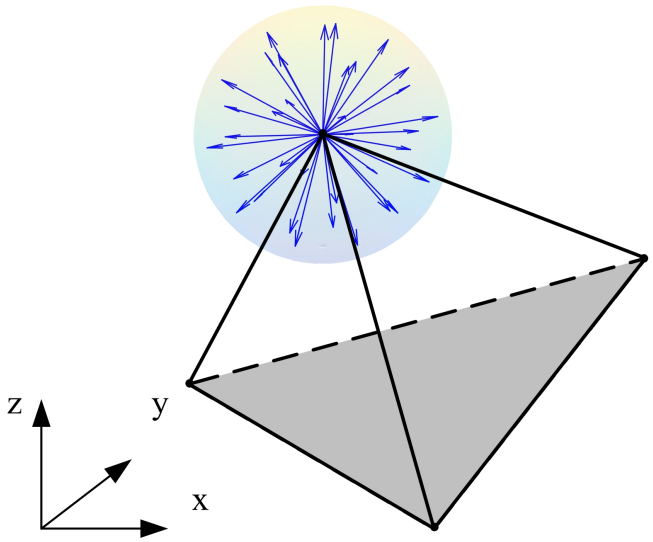

Fig. 2.5 Distribution of plane wave directions in 3D.

$$\boldsymbol{F}_i^t = A\sum_{j=1}^{Q}\frac{(1-\delta_{ij})\times \boldsymbol{r}_{ij}}{|\boldsymbol{r}_{ij}|^3}, \tag{2.21}$$

where A is a scalar multiplier and δ_{ij} is the Kronecker delta which means the force applied on one particle equals to the sum of all the force components resulting from the other particles except for itself. Then, we need to get the vector $\boldsymbol{f}_i^t$ which is taken as the projection vector of resultant force $\boldsymbol{F}_i^t$ on the surface of the sphere and can be expressed as

$$\boldsymbol{f}_i^t = (\boldsymbol{F}_i^t \times \boldsymbol{U}_i^t)\times \boldsymbol{U}_i^t. \tag{2.22}$$

Next, the acceleration $\ddot{\boldsymbol{U}}_i^t$ of each particle is equal to the second derivative of displacement and we have

$$\ddot{\boldsymbol{U}}_i^t = \boldsymbol{f}_i^t - C\dot{\boldsymbol{U}}_i^t, \tag{2.23}$$

where, C represents an equivalent viscous damping coefficient (which avoids numerical oscillations) ranging from 1 to 50, and $\dot{\boldsymbol{U}}_i^t$ is the velocity of the particle. In the time-stepping scheme, we have to get the velocity and position at the subsequent time $t+\Delta t$, both of them can be obtained through

$$\dot{\boldsymbol{U}}_i^{t+\Delta t} = \dot{\boldsymbol{U}}_i^t + \ddot{\boldsymbol{U}}_i^t \Delta t, \tag{2.24}$$

$$\hat{\boldsymbol{U}}_i^{t+\Delta t} = \boldsymbol{U}_i^t + \dot{\boldsymbol{U}}_i^t \Delta t, \tag{2.25}$$

$$\boldsymbol{U}_i^{t+\Delta t} = \frac{\hat{\boldsymbol{U}}_i^{t+\Delta t}}{\left\|\hat{\boldsymbol{U}}_i^{t+\Delta t}\right\|}, \tag{2.26}$$

where (2.26) corresponds to the normalization of the position vector to ensure that the end points always lies on the spherical surface. Next, a stopping criteria among severals needs to be defined properly to make sure the final result converges. Herein, we use the criteria that once the maximum fluctuation of the electron position vector $\boldsymbol{U}_i^{t+\Delta t}$ is smaller than the preset tolerance $\epsilon = 10^{-4}$, we are sure that this time-stepping scheme has converged successfully. Alternatively, the second appropriate option is to assess the evolution of minimum angle ρ between two vectors $\boldsymbol{U}_i$ and $\boldsymbol{U}_j$, which can be computed from

$$\rho = \min(\cos^{-1}\frac{\boldsymbol{U}_i \cdot \boldsymbol{U}_j}{\|\boldsymbol{U}_i\|\,\|\boldsymbol{U}_j\|}), \qquad i = 1,...,Q \quad \text{and} \quad j = 1,...,Q. \tag{2.27}$$

Getting the maximum value of minimum angle ρ permits us to obtain the uniform distribution of electron particles surrounding the spherical surface. Furthermore, we must pay attention to the suitable selection of parameters A, C and Δt. They should be selected properly according

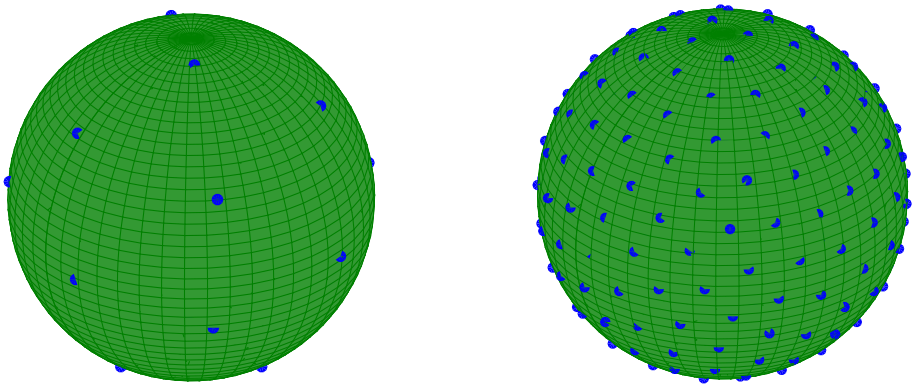

Fig. 2.6 Distribution of wave directions using Coulomb force method: $Q = 20$ plane wave directions (left), $Q = 200$ plane wave directions (right).

to the number of directions Q involved in the PUFEM discretization to avoid excessive time steps or even non-convergence. Numerical experiments show that bigger time steps could be used when there exists a large number of plane wave directions if both A, C are fixed. For example, if we set $A = 100,\ C = 30$ and 500 time steps, then it was found that Δt is required to be less than 3×10^{-3} when $1000 < Q < 1500$, whereas Δt is only required to be less than 3×10^{-2} when $5 < Q < 20$. Figure 2.6 shows different number of wave directions using the Coulomb force distribution method.

Compared to the discretized cube method depicted in Figure 2.7, the use of Coulomb force method allows to obtain uniformly spaced directions, and at the same time, avoid the possibility of a group of plane waves gathering together in a preferred direction which might deteriorate the stability of the PUFEM solution. Through dozens of numerical tests for 3D problems, it was verified that the numerical errors based on the same number of plane waves are not severely influenced by the different distribution schemes. However, the major advantage of Coulomb force method is that an arbitrary number of wave directions can be assigned on each node, which renders the PUFEM method much more flexible.

2.4 PUFEM coefficient matrices

Since we have presented the weak formulation and the discretization procedure for the conventional FEM, and introduced the concept of the enriched approximation finite element space in PUFEM, we now proceed to derive the coefficient matrices. From (2.18), both trial

and test functions are of the following form (we omit the presence of $\boldsymbol{x}_j$ here):

$$p = N_i \exp(\mathrm{i}\kappa \boldsymbol{d}' \cdot \boldsymbol{x}) \quad \text{and} \quad \delta p = N_j \exp(\mathrm{i}\kappa \boldsymbol{d}'' \cdot \boldsymbol{x}), \tag{2.28}$$

where N_i and N_j are the interpolation functions corresponding to the trial and test function, respectively. Indices i and j refer to the node number of the element. Note that we denote by $\boldsymbol{d}'$ the directional vector of the trial function, it is one of the wave directions of the plane wave basis with regard to node i as shown in (2.16). Similarly, $\boldsymbol{d}''$ stands for the wave directions associated with the basis attached to node j. Substituting (2.28) in the weak form of the governing Helmholtz equation (2.7), we arrive at PUFEM matrix coefficients which are of the form:

$$\begin{aligned} A_{pum} = &- \kappa^2 (1 + \boldsymbol{d}' \cdot \boldsymbol{d}'') \int_{\Omega_e} N_i N_j \phi \, \mathrm{d}\Omega + \mathrm{i}\kappa \boldsymbol{d}'' \cdot \int_{\Omega_e} \nabla N_i N_j \phi \, \mathrm{d}\Omega \\ &+ \mathrm{i}\kappa \boldsymbol{d}' \cdot \int_{\Omega_e} \nabla N_j N_i \phi \, \mathrm{d}\Omega + \int_{\Omega_e} \nabla N_i \cdot \nabla N_j \phi \, \mathrm{d}\Omega, \end{aligned} \tag{2.29}$$

where, we introduced

$$\phi = \exp(\mathrm{i}k \boldsymbol{d} \cdot \boldsymbol{x}) \quad \text{with} \quad k = \kappa |\boldsymbol{d}' + \boldsymbol{d}''| \quad \text{and} \quad \boldsymbol{d} = \frac{\boldsymbol{d}' + \boldsymbol{d}''}{|\boldsymbol{d}' + \boldsymbol{d}''|}. \tag{2.30}$$

Figure 2.8 (right) shows the typical pattern of the resulting system matrix, size of which depends on the number of wave directions in the PUFEM basis. To be more specific, if the classical low-order FEM matrices are real-valued, large, frequency independent and sparsely populated with a banded structure, PUFEM is characterized by full block system matrices which are always complex, frequency dependent and generally non-symmetric. The system matrices of PUFEM model are much smaller than the counterpart of low-order FEM

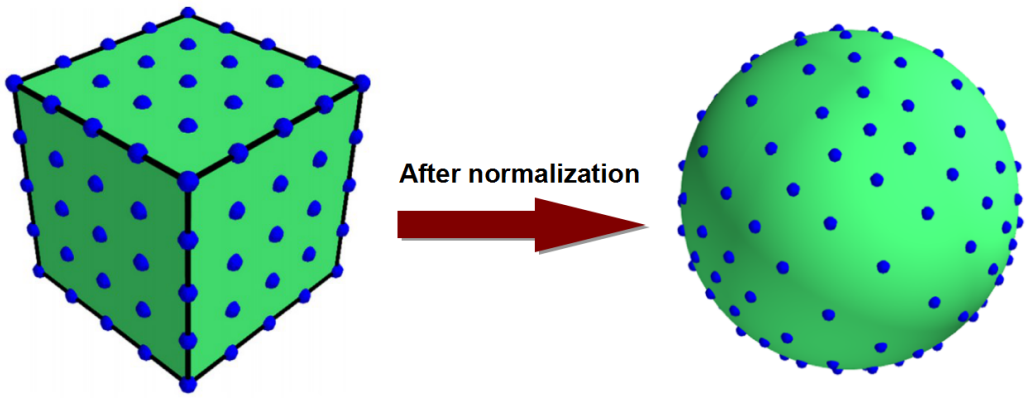

Fig. 2.7 Distribution using the discretized cube method (taken from the reference [103]).

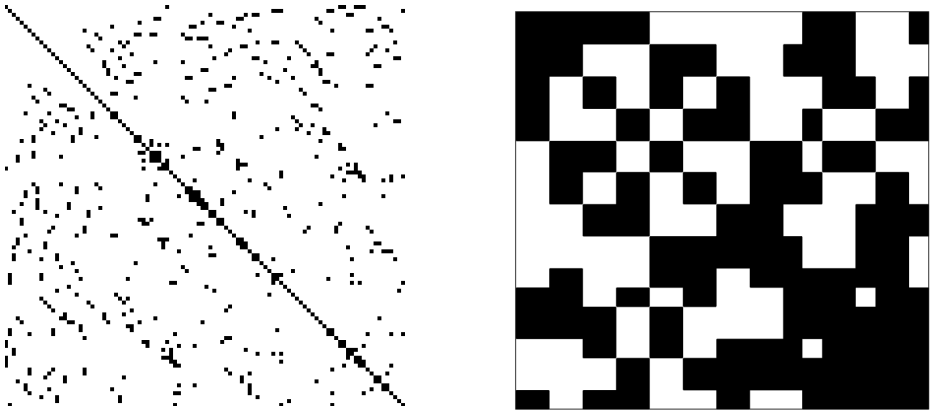

Fig. 2.8 The coefficient system matrix for classical FEM (left) and PUFEM (right).

model for comparable problems. The properties of FEM allow for the reuse of the matrices for different frequencies, leading to an efficient solution, except for some problems (e.g. poroelastic materials featuring complex and frequency dependent properties). In this case, the FE matrices, which are complex, have to be recalculated for each frequency, hampering the efficient solution and also the applicability of modal reduction schemes. In contrast, for PUFEM and all other wave-based approaches, the matrices need to be reconstructed for every frequency of interests. Therefore, the computational performances of the PUFEM are not influenced by the inclusion of localised or complex frequency dependent damping models.

2.5 Some other functions basis for PUFEM

For solving harmonic wave propagation problems, not only the plane wave basis can be used in the enrichment procedure of the finite element space (see(2.16)), but also some other options exist. For example, Bessel functions, Hankel functions, evanescent wave basis functions and Fourier-based functions and so on. The imperative feature of those basis functions is that they are supposed to be the solutions of the homogeneous Helmholtz equation. The decision of which basis function should be used, in fact, depends strongly on the different physical properties and geometries of the problem, as well as some consideration for accuracy, efficiency and computational burden. Clearly, the plane wave basis enjoys the biggest advantage that the integrals of system matrix can be evaluated analytically (this will be shown and illustrated in detail in the next chapters), thus leading to the reduction of numerical cost by eliminating the use of Gaussian quadrature procedures. We shall now briefly present some other alternative PUFEM basis that exist in the literature.

2.5.1 Bessel basis functions

Instead of expanding the nodal value of the pressure according to equation (2.16), this value at each node j is expanded by introducing the Bessel function of the first kind and order l, which is

$$P_j = \sum_{l=0}^{m-1} A_{jl} J_l(\kappa|\boldsymbol{x} - \boldsymbol{x}_j|) e^{\mathrm{i}l\theta}, \tag{2.31}$$

where l is the order of the Bessel function, θ is the polar angle with regard to node $\boldsymbol{x}_j$. Similarly, the A_{jl} corresponds to the amplitude of each radial wave. Herein, the advantages of the Hankel basis over plane wave basis are summarized as follows:

Firstly, a Hankel basis allows greater flexibility than the plane wave basis, the traditional plane wave basis is likely to become close to linearly dependent when a large number of basis functions are used on each element, resulting in the system matrices becoming badly conditioned. According to [61], the Bessel functions basis is less linearly dependent. Secondly, it can be adjusted to capture the singular behavior at corners where a mesh-refinement is usually needed [35]. Thirdly, numerical tests show better performance in the far field of a scattering problem and provides higher accuracy [81]. However, the corresponding integrals for the Bessel basis in PUFEM must be calculated through quadrature methods, so that it becomes much more time-consuming for medium and high frequency problems compared to the plane wave basis. It's suggested that in cases where the requirement for the accuracy is not too high (say around 1%), the plane wave basis is generally a better choice for its efficiency in comparison with Bessel functions.

2.5.2 Polynomials and trigonometric functions

In the work of Ham and Bathe [58], it was shown that the solution field can be discretized with the usual Lagrangian functions augmented with trigonometric functions within the elements. Rather than incorporating the specific wave propagation solutions into the finite element approximation space, they propose to embed the general multiple wave patterns into the solution space based on the fact that we often do not know *a priori* the wave pattern. Therefore, using trigonometric functions seems to be a more systematic way of capturing the unknown wave solutions. The typical solution variable for one-dimensional problems is [58]:

$$P_j = \sum_{\ell=1}^{n} A_{j\ell} \left\{ \cos\left(\frac{2\pi}{\lambda}\ell x\right) + \sin\left(\frac{2\pi}{\lambda}\ell x\right) \right\}, \tag{2.32}$$

where, x denotes the coordinates at any point of the element, λ is the fundamental wavelength, and n is a cutoff number. It can be seen that the nodal value is enriched by trigonometric functions instead of *a priori* analytical solution to the wave equation. Here we considered only one-dimensional problems, an important point is that their enrichment method can, in principle, also be extended to three-dimensional, beam, plate, shell and general nonlinear problems [58].

2.6 Concluding remarks

In this chapter, we have introduced the underlying concept of PUFEM and presented the basic formulation for the acoustical wave propagation problem in a bounded domain. The plane wave enrichment process of PUFEM variables has been illustrated in detail, which incorporates part of the *a priori* analytical solutions of the physical problems. In addition, we showed that the number of plane wave directions depends on the size of the PUFEM element and the wave frequency both in 2D and 3D. The selection approaches for these plane waves were also thoroughly explained. For 3D problems, we have investigated two distribution schemes of plane wave directions which are the discretized cube method and the Coulomb force method. It was shown that the latter allows to get uniformly spaced wave directions and enables us to acquire an arbitrary number of plane waves attached to each node of the PUFEM element.

Chapter 3

PUFEM for 2D acoustic waves

This chapter focuses on the computation of propagating sound fields in two dimensions using the PUFEM technique. As it will be discussed, the heavy computational cost resulting from numerical quadrature of non-polynomial shape functions poses a threshold in terms of efficiency of the PUFEM. Thereby, an Exact Integration Scheme (EIS) for 2D problems is presented and explained in this chapter with all necessary details. This procedure allows us to significantly accelerate the computation of the system coefficient matrices and ease the computational burden. Finally, a numerical model of practical interest is set up for validation purpose. The efficiency of the numerical model developed in this chapter which combines PUFEM and EIS together will be assessed.

3.1 The Exact Integration Scheme (EIS) in 2D

From the previous chapter, we know that the classical low-order FEM produces very sparse matrices whereas PUFEM is characterized by full block matrices. Now, if we want to tackle medium and high frequency problems using wave finite elements, one has to deal with highly oscillatory integrals consisting of the product of polynomials and exponential functions, see equation (2.29). In this context, efficient analytical integration methods have been developed in the literatures [17, 116] for rectangular and triangular elements, and the technique presented here follows a similar approach.

When the wavelength becomes much smaller than the dimension of the PUFEM element, a large number of integration points have to be used in order to attain sufficient accuracy. For the sake of illustration, the Gauss points required to integrate highly-oscillating functions over a triangular element is depicted in Figure 3.1.

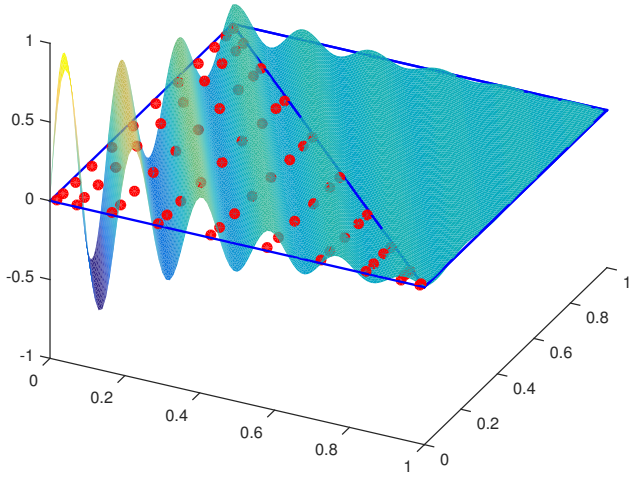

Fig. 3.1 Gauss points needed to integrate a highly oscillating wave function.

The red points depicted in the above figure represent the Gauss-Legendre quadrature points for two dimensional wave problems. The Gauss-Legendre integration over the triangular domain can be implemented by using general Cartesian product rules [74, 105] as:

$$\int_0^1 \int_0^{\zeta_0} F(\zeta_1, \zeta_0) \mathrm{d}\zeta_1 \mathrm{d}\zeta_0 \approx \sum_{i=1}^{n_0} w_i^{(n_0)} t_i^{(n_0)} \sum_{j=1}^{n_{1,i}} w_j^{(n_{1,i})} F(t_i^{(n_0)} t_j^{(n_{1,i})}, t_i^{(n_0)}), \tag{3.1}$$

where $\zeta_0 = \zeta_1 + \zeta_2$ and F is the quantity to be integrated. The set

$$\left\{ w_i^{(n)}; t_i^{(n)}; i = 1, ..., n \right\}$$

are the classical quadrature weights and abscissae obtained from the n-point Gauss-Legendre formula on the interval $[0, 1]$. In order to get a homogeneous distribution of the integration points over a triangular domain, $n_{1,i}$ is generally taken to be linearly varying with the ζ_0-coordinate following the relation $n_{1,i} = [\alpha n_0 t_i^{(n_0)}] + \beta$. In practice, $\alpha = 1$ and $\beta = 10$ is found to be adequate for numerical integration [105].

It is known that the computed results using PUFEM are highly sensitive to each entry of the system matrix due to the ill-conditioned nature of the PUFEM matrix, as shown later. In this context, the expected quadrature accuracy largely depends on: (1) the number of Gauss points and (2) the wavenumber under consideration. As a consequence, we have to inevitably consider the issue of heavy computational cost when standard quadrature methods

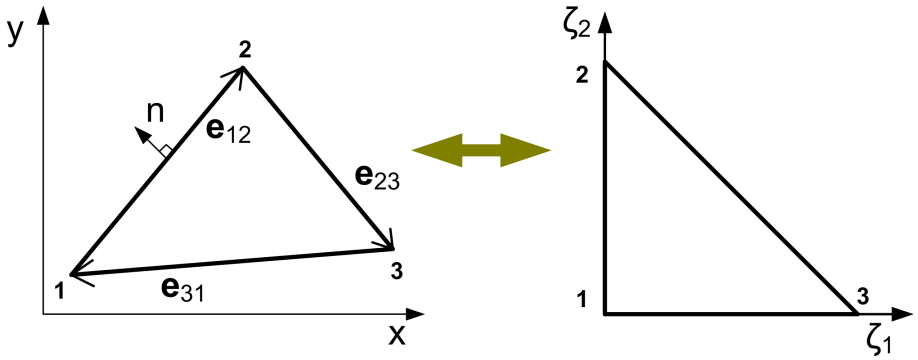

Fig. 3.2 2D coordinates mapping system between real and local element space.

are employed for solving medium or high frequency wave problems.

Let us consider the geometry of the PUFEM element. For the implementation of EIS, it must be ensured that there exists a linear mapping between the local space (ζ_1, ζ_2) and the real space $\boldsymbol{x} = (x, y)$, as shown in Figure 3.2. With the adopted 2D linear shape functions being $N_1 = 1 - \zeta_1 - \zeta_2$, $N_2 = \zeta_1$ and $N_3 = \zeta_2$, the mapping system is, thus, given by

$$\boldsymbol{x} = \boldsymbol{x}_1 N_1 + \boldsymbol{x}_2 N_2 + \boldsymbol{x}_3 N_3, \tag{3.2}$$

where $\boldsymbol{x}_1 = (x_1, y_1)$, $\boldsymbol{x}_2 = (x_2, y_2)$ and $\boldsymbol{x}_3 = (x_3, y_3)$ are the coordinates of the vertices of the triangular element. The Jacobian matrix of the mapping can be simply expressed as

$$\mathbf{J} = \begin{bmatrix} \frac{\partial x}{\partial \zeta_1} & \frac{\partial x}{\partial \zeta_2} \\ \frac{\partial y}{\partial \zeta_1} & \frac{\partial y}{\partial \zeta_2} \end{bmatrix} = \begin{bmatrix} x_2 - x_1 & x_3 - x_1 \\ y_2 - y_1 & y_3 - y_1 \end{bmatrix} = \left[\boldsymbol{e}_{12} \; \boldsymbol{e}_{13} \right],$$

which allows us to write

$$\mathrm{d}x\mathrm{d}y = |\det(\mathbf{J})| \mathrm{d}\zeta_1 \mathrm{d}\zeta_2. \tag{3.3}$$

Moreover, the inverse of the Jacobian matrix $\mathbf{H} = \mathbf{J}^{-1}$ is a constant matrix and we can also obtain the value of the gradients using the following identity (F is arbitrary here):

$$\nabla F = \mathbf{H} \nabla_\zeta F. \tag{3.4}$$

Now, let us recall that the PUFEM coefficient matrices are obtained from equation (2.29). Since the geometric mapping is linear and that shape functions N_i are also linear, some terms

can be moved out of the integral which gives:

$$\begin{aligned} A_{pum} = &- \kappa^2(1 + \boldsymbol{d}' \cdot \boldsymbol{d}'') \int_{\Omega_e} N_i N_j \phi \, \mathrm{d}\Omega + \mathrm{i}\kappa \boldsymbol{d}'' \cdot \nabla N_i \int_{\Omega_e} N_j \phi \, \mathrm{d}\Omega \\ &+ \mathrm{i}\kappa \boldsymbol{d}' \cdot \nabla N_j \int_{\Omega_e} N_i \phi \, \mathrm{d}\Omega + \nabla N_i \cdot \nabla N_j \int_{\Omega_e} \phi \, \mathrm{d}\Omega. \end{aligned} \tag{3.5}$$

We can identify 3 different types of integral:

$$I_2 = \int_{\Omega_e} N_i N_j \, \phi \, \mathrm{d}\Omega, \tag{3.6}$$

$$I_1 = \int_{\Omega_e} N_i \, \phi \, \mathrm{d}\Omega, \tag{3.7}$$

$$I_0 = \int_{\Omega_e} 1 \, \phi \, \mathrm{d}\Omega. \tag{3.8}$$

Clearly, our objective is to develop an efficient 2D exact integration algorithm with respect to above integrals, which can be written in a more general form

$$I = \int_{\Omega_e} F \, \phi \, \mathrm{d}\Omega. \tag{3.9}$$

In order to treat (3.9), the main idea is based on the important feature of the plane wave function $\exp(\mathrm{i}k\boldsymbol{d} \cdot \boldsymbol{x})$, which is denoted by ϕ and satisfies

$$\nabla\phi = \mathrm{i}k\boldsymbol{d} \cdot \phi \qquad \text{and} \qquad \Delta\phi = -k^2\phi. \tag{3.10}$$

With the help of the above properties, we are able to reduce the dimension of the integration domain by applying the Green theorem. If we iterate this procedure, the linear integration will be further reduced to closed-from expressions which involve no integration at all. Finally, only the coordinate information with respect to the three nodes of the element are needed. The first step is to apply the Green theorem iteratively on equation (3.9), so we can transfer the surface integral over Ω_e to its boundary $\Gamma = \partial\Omega_e$ through the infinite series:

$$I = -\int_{\Gamma} (\epsilon F + \epsilon^2 (\boldsymbol{d} \cdot \nabla) F + \epsilon^3 (\boldsymbol{d} \cdot \nabla)^2 F + \cdots) \, \boldsymbol{d} \cdot \boldsymbol{n} \, \phi \, \mathrm{d}\Gamma, \tag{3.11}$$

where, ϵ is equal to i/k. In fact, only the first three terms are involved since the maximum order of polynomial F appearing in (3.9) is 2. In order to get the analytical solutions to the above integral, let us begin by considering the specific case where $F = N_i N_j$, this actually corresponds to (3.6). Thereby, it can be rewritten as

$$I_2 = -(\epsilon G_0 + \epsilon^2 G_1 + \epsilon^3 G_2), \tag{3.12}$$

where, G_m $(m = 0, 1, 2)$ corresponds to three integrals involving gradient operators of different order, and can be summarized as

$$G_m = \int_\Gamma (\boldsymbol{d} \cdot \nabla)^m N_i N_j \, \boldsymbol{d} \cdot \boldsymbol{n} \, \phi \, \mathrm{d}\Gamma, \tag{3.13}$$

where, the derivative terms $(\boldsymbol{d} \cdot \nabla)^m N_i N_j$ obey the following rules:

- for $m = 1$:
$$(\boldsymbol{d} \cdot \nabla) N_i N_j = N_i (\boldsymbol{d} \cdot \nabla)(N_j) + N_j (\boldsymbol{d} \cdot \nabla)(N_i), \tag{3.14}$$
- for $m = 2$:
$$(\boldsymbol{d} \cdot \nabla)^2 N_i N_j = 2(\boldsymbol{d} \cdot \nabla N_i)(\boldsymbol{d} \cdot \nabla N_j). \tag{3.15}$$

Then, equations (3.13), where $m = 0, 1, 2$, become

$$G_0 = \int_\Gamma N_i N_j \, \boldsymbol{d} \cdot \boldsymbol{n} \, \phi \, \mathrm{d}\Gamma, \tag{3.16}$$

$$G_1 = (\boldsymbol{d} \cdot \nabla N_i) \int_\Gamma N_j \, \boldsymbol{d} \cdot \boldsymbol{n} \, \phi \, \mathrm{d}\Gamma + (\boldsymbol{d} \cdot \nabla N_j) \int_\Gamma N_i \, \boldsymbol{d} \cdot \boldsymbol{n} \, \phi \, \mathrm{d}\Gamma, \tag{3.17}$$

$$G_2 = 2(\boldsymbol{d} \cdot \nabla N_i)(\boldsymbol{d} \cdot \nabla N_j) \int_\Gamma \boldsymbol{d} \cdot \boldsymbol{n} \, \phi \, \mathrm{d}\Gamma. \tag{3.18}$$

Three edge integrals are identified:

$$\int_\Gamma N_i N_j \, \boldsymbol{d} \cdot \boldsymbol{n} \, \phi \, \mathrm{d}\Gamma, \quad \int_\Gamma N_i \, \boldsymbol{d} \cdot \boldsymbol{n} \, \phi \, \mathrm{d}\Gamma, \quad \int_\Gamma 1 \, \boldsymbol{d} \cdot \boldsymbol{n} \, \phi \, \mathrm{d}\Gamma. \tag{3.19}$$

Now, we put $\Gamma = \Gamma_{12} \cup \Gamma_{23} \cup \Gamma_{13}$, and the integrals have to be calculated along each edge of the element. As an example, let us consider the case where $i = 1, 2$ and $j = 1, 2$ with respect to the edge Γ_{12} (the other integrals can be easily obtained in the same way). So we arrive at the following 6 line integrals:

$$\begin{aligned}
D_{12}(1) &= \int_{\Gamma_{12}} 1 \, \boldsymbol{d} \cdot \boldsymbol{n} \, \phi \, \mathrm{d}\Gamma, \\
D_{12}(N_2) &= \int_{\Gamma_{12}} N_2 \, \boldsymbol{d} \cdot \boldsymbol{n} \, \phi \, \mathrm{d}\Gamma, \\
D_{12}(N_1) &= \int_{\Gamma_{12}} N_1 \, \boldsymbol{d} \cdot \boldsymbol{n} \, \phi \, \mathrm{d}\Gamma, \\
D_{12}(N_1 N_2) &= \int_{\Gamma_{12}} N_1 N_2 \, \boldsymbol{d} \cdot \boldsymbol{n} \, \phi \, \mathrm{d}\Gamma, \\
D_{12}(N_1^2) &= \int_{\Gamma_{12}} N_1^2 \, \boldsymbol{d} \cdot \boldsymbol{n} \, \phi \, \mathrm{d}\Gamma, \\
D_{12}(N_2^2) &= \int_{\Gamma_{12}} N_2^2 \, \boldsymbol{d} \cdot \boldsymbol{n} \, \phi \, \mathrm{d}\Gamma.
\end{aligned}$$

The analytical solution related to the above integrals can be calculated explicitly. After calculation, we can get

$$D_{12}(1) = \frac{1}{\mathrm{i}k(\boldsymbol{d}\cdot\boldsymbol{e}_{12})}\boldsymbol{d}\cdot\boldsymbol{n}_1\, l_{12}\,(\phi(\boldsymbol{x}_2)-\phi(\boldsymbol{x}_1)), \tag{3.20}$$

$$D_{12}(N_1) = \frac{1}{\mathrm{i}k(\boldsymbol{d}\cdot\boldsymbol{e}_{12})}(-\boldsymbol{d}\cdot\boldsymbol{n}_1\, l_{12}\,(\phi(\boldsymbol{x}_1)+D_{12}(1))), \tag{3.21}$$

$$D_{12}(N_2) = \frac{1}{\mathrm{i}k(\boldsymbol{d}\cdot\boldsymbol{e}_{12})}(\boldsymbol{d}\cdot\boldsymbol{n}_1\, l_{12}\,(\phi(\boldsymbol{x}_2)-D_{12}(1))), \tag{3.22}$$

$$D_{12}(N_1N_2) = \frac{1}{\mathrm{i}k(\boldsymbol{d}\cdot\boldsymbol{e}_{12})}(2D_{12}(N_2)-D_{12}(1)) \tag{3.23}$$

$$D_{12}(N_2^2) = \frac{1}{\mathrm{i}k(\boldsymbol{d}\cdot\boldsymbol{e}_{12})}(\boldsymbol{d}\cdot\boldsymbol{n_1}\, l_{12}\,(\phi(\boldsymbol{x}_2)-2D_{12}(N_2))), \tag{3.24}$$

$$D_{12}(N_1^2) = D_{12}(1)-2D_{12}(N_2)+D_{12}(N_2^2), \tag{3.25}$$

where, $\boldsymbol{x}_i$ is the position vector of node i, and $\boldsymbol{e}_{ij} = \boldsymbol{x}_j - \boldsymbol{x}_i$, and $l_{ij} = |\boldsymbol{e}_{ij}|$. Furthermore, we must take into account the particular case where $\boldsymbol{d}\cdot\boldsymbol{e}_{ij} = 0$, this situation signifies that the directional vector $\boldsymbol{d}$, which corresponds to the sum of two plane wave directions, is perpendicular to the edge of the triangular element. In this case, the analytical solution can be easily obtained as follows:

$$D_{12}(1) = \boldsymbol{d}\cdot\boldsymbol{n}_1 l_{12}(\phi(\boldsymbol{x}_1)), \tag{3.26}$$

$$D_{12}(N_1) = \frac{1}{2}D_{12}(1), \tag{3.27}$$

$$D_{12}(N_2) = \frac{1}{2}D_{12}(1), \tag{3.28}$$

$$D_{12}(N_1N_2) = \frac{1}{6}D_{12}(1). \tag{3.29}$$

Based on the same process, the analytical expressions of the integrals over the other two edges Γ_{23} and Γ_{31} can be derived as well. Consequently, calculation of the exact integration terms in (3.13) is, therefore, achieved. Following the same principle, we can calculate all coefficients G_m appearing in (3.13).

Another particular care must be taken for the case where $\boldsymbol{d} = 0$, which physically means that two plane waves from the PUFEM basis functions happen to propagate totally opposite to each other. In this case, it turns out that the exponential part of the integral in equation (3.6) disappears and only polynomial function is left in the integral, which also can be easily

computed. For instance:

$$I_2 = \int_{\Omega_e} N_1 N_2 \ \mathrm{d}\Omega = \frac{1}{24}|\det(\mathbf{J})|. \tag{3.30}$$

From a numerical point of view, the quantities $\boldsymbol{d}$ and $\boldsymbol{d} \cdot \boldsymbol{e}_{ij}$ are taken to be zero when their Euclidean norm $|\boldsymbol{d} \cdot \boldsymbol{e}_{ij}| \leqslant \epsilon$ and $\|\boldsymbol{d}\| \leqslant \epsilon$, with $\epsilon = 10^{-6}$. This Exact Integration Scheme has been validated thanks to the software Maple. The efficiency of the PUFEM combined with EIS is now shown in the next section.

3.2 Numerical examples

In this section, we aim at investigating the method via a simple numerical model taken form reference [27]. Since the main performances of 2D PUFEM in terms of numerical accuracy and data reduction have been widely studied and the related conclusions can be found in previous works [90, 24, 1, 104], so this will not be the main topic here. The main purpose of this part is, first, to validate the EIS combined with PUFEM. Secondly, to show the computational efficiency (in terms of CPU time) compared to the Gaussian quadrature method. At last, we will also conduct a brief discussion about the numerical performances of PUFEM for solving a standing wave tube problem with porous material. The coupling between porous and air domains and its corresponding numerical implementation is presented in details in Chapter 5 for 3D problems, so this will not be discussed here. The development code is written in Matlab with double precision and accelerated by taking advantage of Fortran, numerical tests are carried out on Xeon X7542 2.67GHz win64 pilcam server.

3.2.1 Numerical model

Figure 3.3 exhibits the geometry of this numerical model where a standing wave tube is presented. The total length of this tube L equals to 0.15 m and is divided into three regions of equal length with $x_1 = L/3$ and $x_2 = 2L/3$. In the first region, a normal velocity boundary condition is prescribed on the left wall. The second region denoted in gray stands for the porous absorber. The last region of the tube consists of an air gap terminated by a rigid wall. Each region has been partitioned into two triangular elements and the related mesh is also shown in Figure 3.3. The analytical solution can be easily obtained. It's worth noting that the characteristic length of the mesh, which is indicated by h_{max}, is chosen to be the longest edge of the PUFEM mesh. Here, $h_{max} = \sqrt{0.05^2 + 0.03^2} \approx 0.06$ m and the width of the tube is equal to 0.03 m.

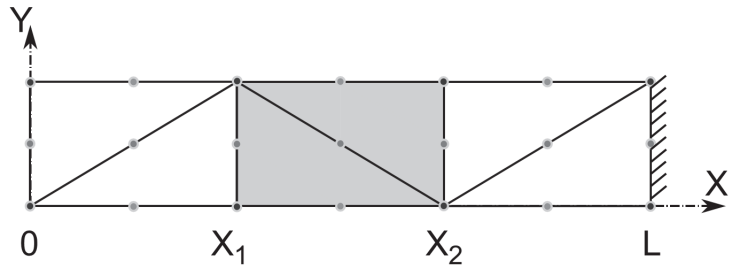

Fig. 3.3 The standing wave tube test and mesh partition

3.2.2 Definition of variables and parameters

Before we proceed to the analysis of the numerical performance, it's necessary to properly define several important parameters. Here, we denote by κ_a and κ_p the wavenumber in air and the porous material, here an artificial value for the porous wavenumber as $\kappa_p = \kappa_a(1 + \chi \mathrm{i})$ is adopted where χ is defined as the ratio between the imaginary and the real part of κ_p. It's important to observe that, with this definition, the wavelength $\lambda = 2\pi/\kappa_a$ is identical in both domains. Moreover, in order to simplify the analysis, we shall take the density values for both regions to be equal, which means $\rho_p = \rho_a$. In addition, with the aim of presenting how many wavelengths are contained in one single finite element, we define the quantity β as:

$$\beta = \frac{h_{max}}{\lambda}. \tag{3.31}$$

Recall that h_{max} is the characteristic length of the mesh. The coefficient C from equation (2.20) is chosen to be 3 in order to provide enough plane wave directions and ensure that results are sufficiently accurate. Moreover, we propose to introduce the average discretization level n_λ which is defined as the number of variables needed to capture a single wavelength, and it can be evaluated via

$$n_\lambda = \lambda \sqrt{\frac{N_{dof}}{\int_\Omega \mathrm{d}\Omega}}, \tag{3.32}$$

where N_{dof} is the total number of the degrees of freedom. In the conventional finite element discretization, the golden rule is that at least 10 degrees of freedom per wavelength ($n_\lambda = 10$) are required to ensure acceptable accuracy. The discretization level can be much smaller in PUFEM, it's already been reported in reference [80] that a substantial gain can be observed if the element size spans over few wavelengths and a discretization level less than 3 degrees of freedom per wavelength is normally sufficient to ensure a converged solution.

From the relation indicated in (2.20), the average discretization level with regard to the

ideal case of a regular triangular mesh of infinite extent in PUFEM is given by [27]

$$n_{\lambda}^{ideal} = \frac{\lambda}{a}\sqrt{Q} = \frac{1}{\beta}\sqrt{4\pi\beta + 2C(2\pi\beta)^{1/3}}, \tag{3.33}$$

in which, a refers to the edge length of an ideal mesh of infinite extent, see Figure 3.4. Most importantly, we can notice that if β is very large, the average discretization level tends to 0, which means, in theory, that very high frequency problems could be solved with nearly 0 degree of freedom per wavelength!

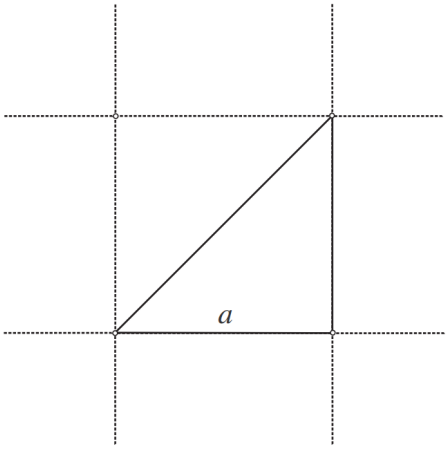

Fig. 3.4 Ideal mesh of infinite extent.

3.2.3 Performance of the method

Figure 3.5 shows the computed acoustic pressure (in dB) with respect to the horizontal axis of the test tube. In this example, the wavenumber κ is chosen to be equal to κ_a. This is a high frequency problem with non-dimensional quantity $\kappa_a h_{max} = 50$ which corresponds to the frequency $f \approx 45,000$ Hz. It can be evaluated that around eight wavelengths are included per element in the given mesh grid, namely, $\beta \approx 8$. It can be observed from Figure 3.6 that the sound pressure decreases to a certain level which is close to 0 dB after propagating through the porous region, note that these results correspond to $\kappa_p = \kappa_a(1+0.1\mathrm{i})$ in this case.

We can also observe from Figure 3.5 and 3.6 that the computed results based on PUFEM are almost identical to the analytical solution. Detailed analysis of the convergence rate offered by the PUFEM has been the subject of previous research work. The main concern here is to compare the EIS with standard quadrature method. The analysis is performed on the same mesh grid ($h_{max} \approx 0.06$ m) for both cases. We can distinguish low frequency applications

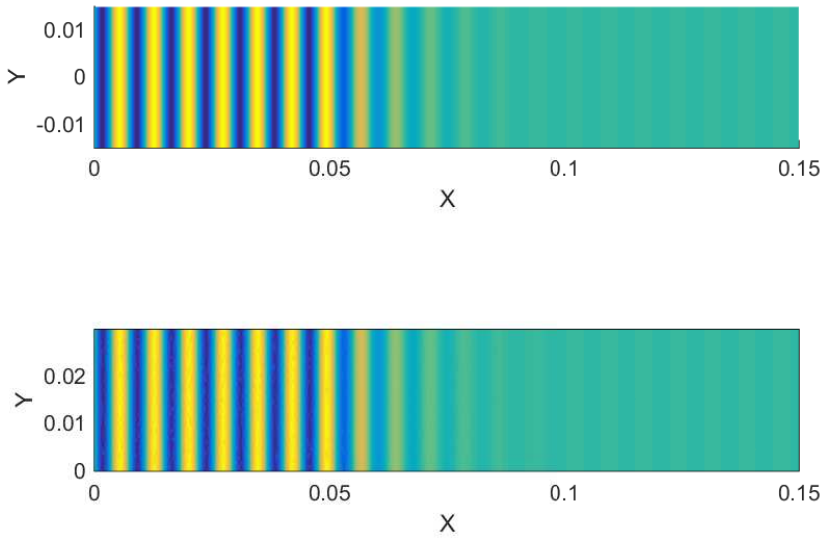

Fig. 3.5 Computed acoustic pressure for standing wave tube test with porous material in the middle region, for $\kappa h_{max} = 50$ and $f \approx 45,000$ Hz. Analytical solution (top) and PUFEM solution (bottom).

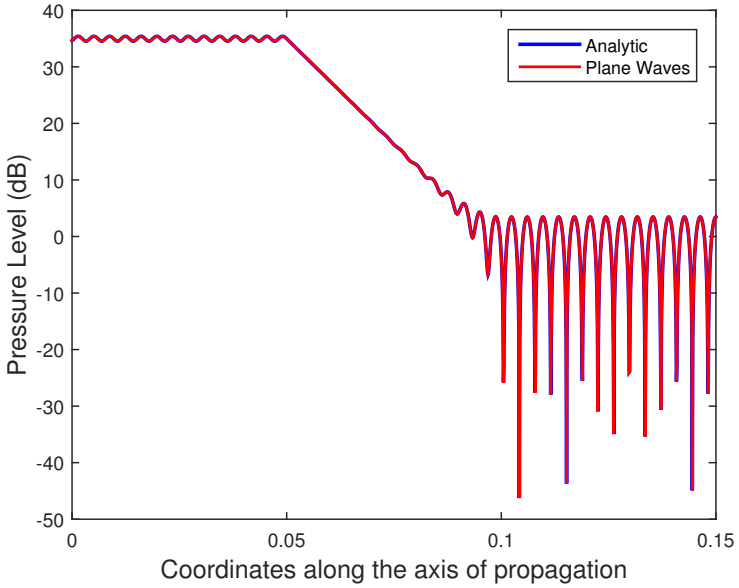

Fig. 3.6 Sound pressure level in (dB) for standing wave tube test with porous material in the middle region, for $\kappa h_{max} = 50$ and $f \approx 45,000$ Hz: analytical solution (blue curve) and PUFEM solution (red curve).

κh_{max}	f(Hz)	Q_{max}	N_{dof}	h_{max}/λ	ngauss (elem)
1	900	4	64	0.16	60
2	1800	6	96	0.32	72
3	2700	7	112	0.48	100
4	3600	9	144	0.63	116
5	4500	10	160	0.79	150
10	9000	16	256	1.59	326
15	13500	22	352	2.39	566
20	18000	28	448	3.18	870
25	22500	34	544	3.98	1238
30	27000	39	624	4.77	1670
35	31500	45	720	5.57	2166
40	36000	50	800	6.37	2726
45	40500	56	896	7.16	3350
50	45000	61	976	7.96	4038

Table 3.1 Parameters for the PUFEM model.

and high frequency applications: $1 \leq \kappa h_{max} \leq 5$ and $10 \leq \kappa h_{max} \leq 50$, which are related to the frequencies of 900 Hz $\leq f \leq 4500$ Hz and $9,000$ Hz $\leq f \leq 45,000$ Hz, respectively. For the sake of fairness, both integration methods are applied to the same PUFEM matrix. Besides, at least 10 Gauss points per wavelength are used for the numerical quadrature of equation (3.1). The parameters for the PUFEM model are reported in Table 3.1, the last column shows the number of Gauss points used for a single element.

Figure 3.7 shows that, for the relatively low frequency range ($\kappa h_{max} \leq 5$), the exact integration scheme is not as efficient as Gauss-Legendre quadrature method because very few gauss points are required for low frequency integrals which is enough to provide high quality results. When the frequency increases, the elapsed time with regard to EIS remains at a relatively low level in comparison with the quadrature method. This great benefit is due to the fact that EIS is frequency-independent. The rise of CPU time for EIS merely stems from the growth of plane wave directions. On the contrary, the consuming time for the quadrature method increases at a high rate when a growing number of gauss points are used. It is expected that the computational burden should grow quadratically with the frequency. To illustrate this, the time ratio between the two methods is given in Figure 3.9, here the number of Gauss points (horizontal-axis) corresponds to the number of points n_0 used along one edge (see (3.1)).

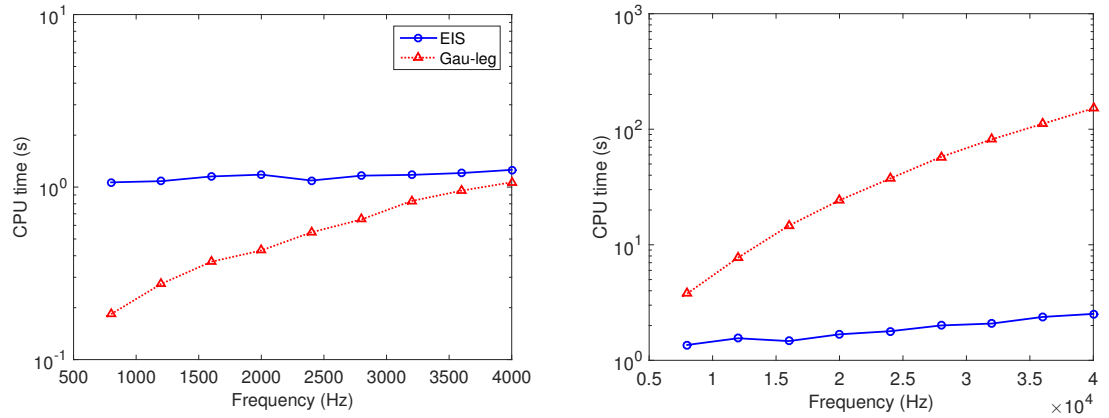

Fig. 3.7 Elapsed CPU time for computing and assembling the system matrices: using EIS (blue curve) and Gauss-Legendre quadrature (red curve) .

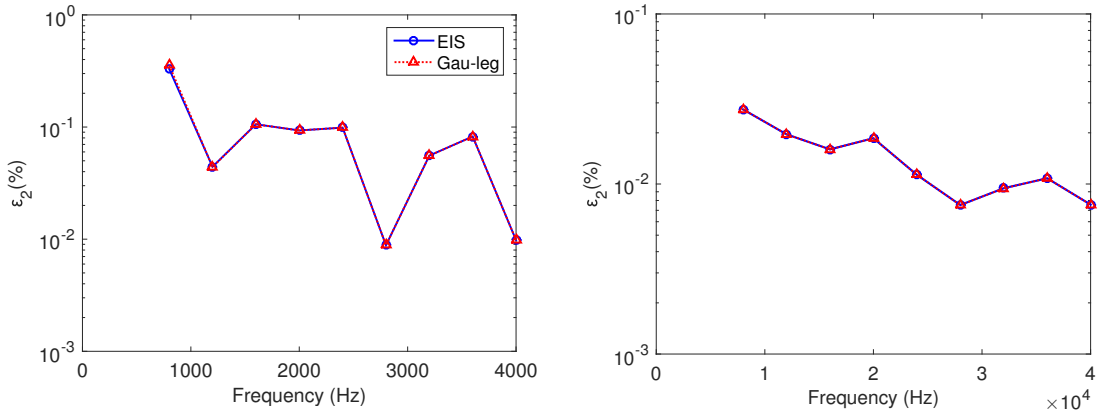

Fig. 3.8 L_2 Error as a function of the frequency: using EIS (blue curve) and Gauss-Legendre quadrature (red curve).

The L_2 error is employed to measure the level of accuracy of the PUFEM solutions, which is defined as:

$$\varepsilon_2(\%) = \frac{\|p_{ex} - p_{pum}\|_{L_2(\Omega)}}{\|p_{ex}\|_{L_2(\Omega)}} \times 100. \tag{3.34}$$

Figure 3.8 plots all the numerical errors with respect to various frequencies (recall the number of plane waves in evaluated from equation (2.20), with $C = 3$). It is obvious that two curves are almost in coincidence with each other for the whole frequency domain. This implies that solution with sufficient precision can be achieved through both methods. It can be noticed that the error remains at a certain level which primary results from the PUFEM approximation procedure rather than the integration error. As the exact solution can be expressed as the sum of two horizontal plane waves propagating in opposite directions, all calculations were

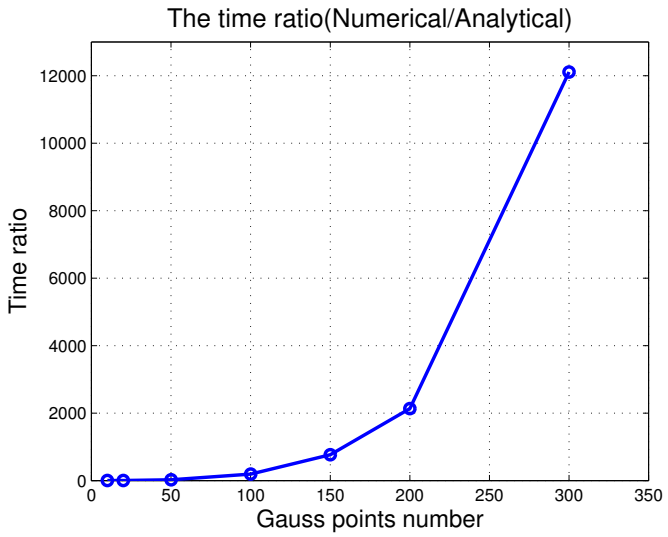

Fig. 3.9 The time ratio between Exact Integration Scheme and Gauss-Legendre quadrature.

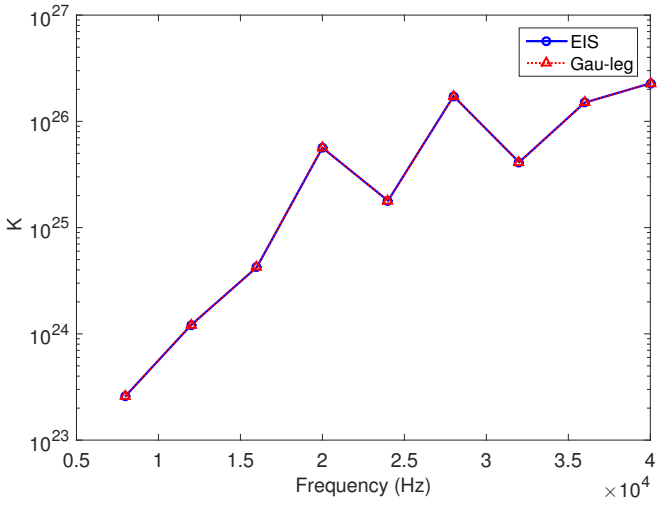

Fig. 3.10 The condition number of the PUFEM matrix.

performed without the horizontal directions in order to ensure that the exact solution is not included in the plane wave basis. Provided that one plane wave direction of PUFEM basis happens to be quite close to the horizontal one, the error might improve drastically and that partly explain the fluctuation of the error. In addition, the numerical error can also be affected by round-off errors due to the ill-conditioned nature of the PUFEM matrix, which is reported in Figure 3.10.

3.3 Concluding remarks

In this chapter, numerical simulation of 2D acoustic waves is performed using PUFEM. An Exact Integration Scheme has been put forward and presented with all necessary details, allowing us to access to a fast integration algorithm for computing system coefficient matrices while maintaining sufficient accuracy. We also took advantage of the 2D PUFEM element to solve an acoustic transmission problem in which porous material is present. The obtained results have been verified and validated by comparing with analytical solutions. Numerical performances of the Exact Integration Scheme have been compared with classical Gauss-Legendre quadrature method.

Chapter 4

PUFEM for 3D acoustic waves

In this chapter, the full development of the PUFEM for 3D acoustical problems is presented. The three critical aspects of the method are investigated in detail and they are organized as follows. First, in Section 4.1, we explain the underlying theory of the Exact Integration Scheme (EIS) as well as the associated algorithm for 3D tetrahedron PUFEM element. Then, in Sections 4.2 and 4.3, we focus on investigating several numerical aspects of 3D PUFEM including error estimation, convergence rate and computational cost. Thirdly, some numerical examples including the response of a point source in a 3D cavity are shown in Section 4.4. Finally, the concluding remarks are given in Section 4.5.

4.1 Exact Integration Scheme (EIS) for 3D PUFEM

As explained in the previous chapter, it is imperative to develop an efficient three-dimensional integration scheme for addressing the computation of 3D highly oscillatory wave integrals. Typically, the computational burden stemming from the huge amounts of integration gauss points will be inevitable if standard quadrature methods are used. This is well illustrated in Figure 3.1 except that one more dimension needs to be taken into account in 3D. In order to alleviate this limitation, an advanced exact integration scheme is, therefore, developed and presented in this section. The core idea of EIS for solving 3D problems is similar to its 2D counterpart and is summarized herein. Through the application of Green theorem, the volume integral can be reduced to its surface integrals. Then, by iterating the same strategy, the integration domain can be further simplified from the triangular surfaces to their edges. Finally, the volume integrals can be fully expressed via analytical formulas that require the values of the wave functions at the 4 vertices of the PUFEM element.

4.1.1 Applying Green theorem to the volume integral

Let us recall that the PUFEM coefficient matrices can be obtained from (2.29) in Chapter 2, which is of the form:

$$\begin{aligned} A_{pum} = &-\kappa^2(1+\boldsymbol{d}'\cdot\boldsymbol{d}'')\int_{\Omega_e} N_iN_j\phi\,\mathrm{d}\Omega + \mathrm{i}\kappa\boldsymbol{d}''\cdot\int_{\Omega_e}\nabla N_iN_j\phi\,\mathrm{d}\Omega \\ &+\mathrm{i}\kappa\boldsymbol{d}'\cdot\int_{\Omega_e}\nabla N_jN_i\phi\,\mathrm{d}\Omega + \int_{\Omega_e}\nabla N_i\cdot\nabla N_j\phi\,\mathrm{d}\Omega. \end{aligned} \tag{4.1}$$

Following the same analysis as for the 2D problem, we also consider a linear mapping system between real and local coordinate, as shown in Figure 4.1. The linear shape functions are of the form: $N_1=\zeta_1$, $N_2=\zeta_2$, $N_3=\zeta_3$ and $N_4=1-\zeta_1-\zeta_2-\zeta_3$, and we can write explicitly the linear mapping between real space (x,y,z) and local space $(\zeta_1,\zeta_2,\zeta_3)$ as

$$\boldsymbol{x}=\sum_{i=1}^{4}N_i\boldsymbol{x}_i=\boldsymbol{x}_4+\zeta_1\boldsymbol{e}_{41}+\zeta_2\boldsymbol{e}_{42}+\zeta_3\boldsymbol{e}_{43}. \tag{4.2}$$

Here, note that we adopt the notation $\boldsymbol{e}_{ij}=\boldsymbol{x}_j-\boldsymbol{x}_i$, so that the Jacobian matrix can be written by

$$\mathbf{J}=\begin{bmatrix}\boldsymbol{e}_{41} & \boldsymbol{e}_{42} & \boldsymbol{e}_{43}\end{bmatrix}^{\top}. \tag{4.3}$$

Its inverse $\mathbf{H}=\mathbf{J}^{-1}$ is then can be easily calculated, which allows us to get the transformation formulas for the gradient and Laplace operators:

$$\nabla F=\mathbf{H}\nabla_{\zeta}F \qquad \text{and} \qquad \triangle F=H_{il}H_{ij}\partial_{\zeta_l\zeta_j}F. \tag{4.4}$$

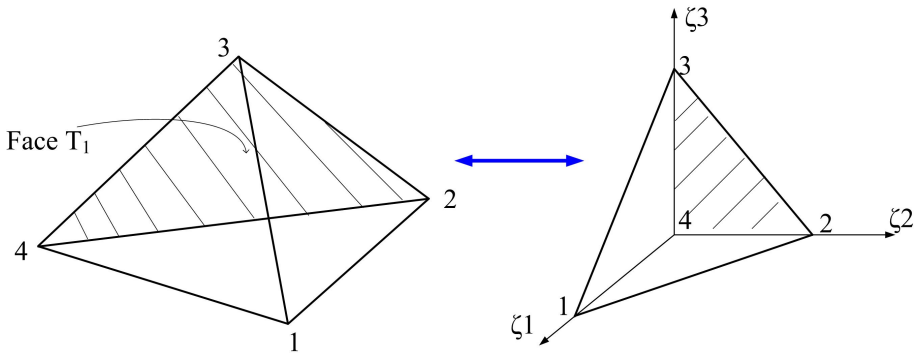

Fig. 4.1 3D coordinates systems in real and local element space.

Since the geometric mapping is linear and the shape functions N_i are also linear, some terms can be moved out of the integrals in (4.1), which results in

$$\begin{aligned} A_{pum} = &- \kappa^2(1 + \boldsymbol{d}' \cdot \boldsymbol{d}'') \int_{\Omega_e} N_i N_j \phi \,\mathrm{d}\Omega + \mathrm{i}\kappa \boldsymbol{d}'' \cdot \nabla N_i \int_{\Omega_e} N_j \phi \,\mathrm{d}\Omega \\ &+ \mathrm{i}\kappa \boldsymbol{d}' \cdot \nabla N_j \int_{\Omega_e} N_i \phi \,\mathrm{d}\Omega + \nabla N_i \cdot \nabla N_j \int_{\Omega_e} \phi \,\mathrm{d}\Omega, \end{aligned} \tag{4.5}$$

where we can find that three volume integrals from equation (4.5) are of the form

$$\int_{\Omega_e} N_i N_j \phi \,\mathrm{d}\Omega, \quad \int_{\Omega_e} N_i \phi \,\mathrm{d}\Omega \quad \text{and} \quad \int_{\Omega_e} \phi \,\mathrm{d}\Omega. \tag{4.6}$$

Meanwhile, the above integrals can be written into a general type, which gives rise to

$$\int_{\Omega_e} F \phi \,\mathrm{d}\Omega. \tag{4.7}$$

The use of Green theorem yields:

$$\int_{\Omega_e} F \,\phi \mathrm{d}\Omega = - \int_{\partial\Omega_e} (\epsilon F \boldsymbol{d} + \epsilon^2 \nabla F + \epsilon^3 \triangle F \boldsymbol{d} + \cdots) \cdot \boldsymbol{n} \,\phi \,\mathrm{d}(\partial\Omega), \tag{4.8}$$

where $\epsilon = \mathrm{i}/k$. The important feature of the linear mapping signifies that the maximum order of the polynomial F in the above volume integrals is quadratic, so only the first three terms of the series are kept. Note that the above equation is just an alternative formulation to equation (3.11), but more convenient to derive analytical formulas in the context of 3D PUFEM element. In the following, we define the notation:

$$\partial\Omega_e = \bigcup_{\alpha=1}^{4} T_\alpha, \tag{4.9}$$

to represent all surfaces of the tetrahedron element, where T_α denotes each surface of the element, and it's important to keep in mind that α stands for the node number of the element which lies opposite to the surface. For the sake of illustration, T_1 is highlighted in Figure 4.1, where we can see that it refers to the surface opposite to node 1. Moreover, it is understood that the term F in (4.7) represents three different kinds of polynomials which are $N_i N_j$, N_i and 1, respectively. Applying (4.8), we get

$$\begin{aligned} \int_{\Omega_e} N_i N_j \phi \,\mathrm{d}\Omega = &- \sum_{\alpha=1}^{4} \boldsymbol{d} \cdot \boldsymbol{n}_\alpha \left(\epsilon \int_{T_\alpha} N_i N_j \phi \,\mathrm{d}S + \epsilon^3 \triangle (N_i N_j) \int_{T_\alpha} \phi \,\mathrm{d}S \right) \\ &- \epsilon^2 \sum_{\alpha=1}^{4} \boldsymbol{n}_\alpha \cdot \nabla N_i \int_{T_\alpha} N_j \phi \,\mathrm{d}S - \epsilon^2 \sum_{\alpha=1}^{4} \boldsymbol{n}_\alpha \cdot \nabla N_j \int_{T_\alpha} N_i \phi \,\mathrm{d}S, \end{aligned} \tag{4.10}$$

and

$$\int_{\Omega_e} N_j \phi \,\mathrm{d}\Omega = -\sum_{\alpha=1}^{4} \boldsymbol{d}\cdot\boldsymbol{n}_\alpha \epsilon \int_{T_\alpha} N_j \phi \,\mathrm{d}S, -\epsilon^2 \sum_{\alpha=1}^{4} \boldsymbol{n}_\alpha \cdot \nabla N_j \int_{T_\alpha} \phi \,\mathrm{d}S, \tag{4.11}$$

and

$$\int_{\Omega_e} \phi \,\mathrm{d}\Omega = -\sum_{\alpha=1}^{4} \boldsymbol{d}\cdot\boldsymbol{n}_\alpha \epsilon \int_{T_\alpha} \phi \,\mathrm{d}S. \tag{4.12}$$

For the above equations, we must pay attention to the direction of normal vectors $\boldsymbol{n}_\alpha$, they have to point out of the surfaces of each element. At this stage, we can identify three types of surface integrals, namely:

$$\int_{T_\alpha} \phi \,\mathrm{d}S, \quad \int_{T_\alpha} N_i \phi \,\mathrm{d}S \quad \text{and} \quad \int_{T_\alpha} N_i N_j \phi \,\mathrm{d}S. \tag{4.13}$$

Operating an appropriate change of variable from the real space T_α to the local coordinate system (note that the reference triangle domain is denoted by $\triangle$ here) gives (start with the first integral):

$$\begin{aligned}\int_{T_1} \phi \,\mathrm{d}S &= \int_{T_1} \exp(\mathrm{i}k\boldsymbol{d}\cdot(\boldsymbol{x}_4 + \zeta_2\boldsymbol{e}_{42} + \zeta_3\boldsymbol{e}_{43}))\,\mathrm{d}S \\ &= 2A_1\,\mathrm{e}^{\omega_4}\int_{\triangle} \exp(\zeta_2(\omega_2-\omega_4)+\zeta_3(\omega_3-\omega_4))\,\mathrm{d}\zeta_2\mathrm{d}\zeta_3 \\ &= 2A_1\,\mathrm{e}^{\omega_4} I_{00}^{\triangle}(\boldsymbol{a}) \quad \text{and} \quad \boldsymbol{a} = (\omega_2-\omega_4, \omega_3-\omega_4),\end{aligned} \tag{4.14}$$

$$\begin{aligned}\int_{T_2} \phi \,\mathrm{d}S &= \int_{T_2} \exp(\mathrm{i}k\boldsymbol{d}\cdot(\boldsymbol{x}_4 + \zeta_1\boldsymbol{e}_{41} + \zeta_3\boldsymbol{e}_{43}))\,\mathrm{d}S \\ &= 2A_2\,\mathrm{e}^{\omega_4}\int_{\triangle} \exp(\zeta_1(\omega_1-\omega_4)+\zeta_3(\omega_3-\omega_4))\,\mathrm{d}\zeta_1\mathrm{d}\zeta_3 \\ &= 2A_2\,\mathrm{e}^{\omega_4} I_{00}^{\triangle}(\boldsymbol{a}) \quad \text{and} \quad \boldsymbol{a} = (\omega_1-\omega_4, \omega_3-\omega_4),\end{aligned} \tag{4.15}$$

$$\begin{aligned}\int_{T_3} \phi \,\mathrm{d}S &= \int_{T_3} \exp(\mathrm{i}k\boldsymbol{d}\cdot(\boldsymbol{x}_4 + \zeta_1\boldsymbol{e}_{41} + \zeta_2\boldsymbol{e}_{42}))\,\mathrm{d}S \\ &= 2A_3\,\mathrm{e}^{\omega_4}\int_{\triangle} \exp(\zeta_1(\omega_1-\omega_4)+\zeta_2(\omega_2-\omega_4))\,\mathrm{d}\zeta_1\mathrm{d}\zeta_2 \\ &= 2A_3\,\mathrm{e}^{\omega_4} I_{00}^{\triangle}(\boldsymbol{a}) \quad \text{and} \quad \boldsymbol{a} = (\omega_1-\omega_4, \omega_2-\omega_4),\end{aligned} \tag{4.16}$$

$$\begin{aligned}\int_{T_4}\phi\,\mathrm{d}S &= \int_{T_4}\exp(\mathrm{i}k\boldsymbol{d}\cdot(\boldsymbol{x}_3+\zeta_1\boldsymbol{e}_{31}+\zeta_2\boldsymbol{e}_{32}))\,\mathrm{d}S\\ &= 2A_4\,\mathrm{e}^{\omega_3}\int_{\triangle}\exp(\zeta_1(\omega_1-\omega_3)+\zeta_2(\omega_2-\omega_3))\,\mathrm{d}\zeta_1\mathrm{d}\zeta_2\\ &= 2A_4\,\mathrm{e}^{\omega_3}I_{00}^{\triangle}(\boldsymbol{a})\quad\text{and}\quad\boldsymbol{a}=(\omega_1-\omega_3,\omega_2-\omega_3).\end{aligned}\tag{4.17}$$

Here, we define:

$$\omega_\alpha=\mathrm{i}k\boldsymbol{d}\cdot\boldsymbol{x}_\alpha\quad\text{and}\quad A_\alpha=\int_{T_\alpha}\mathrm{d}S,\quad\alpha=1,...,4.$$

Thus, the above 4 surface integrals can be rewritten in a compact form:

$$\int_{T_\alpha}\phi\,\mathrm{d}S=2A_\alpha\mathrm{e}^{\omega_{\alpha-1}}\int_{\triangle}\exp(x(\omega_{\alpha+1}-\omega_{\alpha-1})+y(\omega_{\alpha+2}-\omega_{\alpha-1}))\,\mathrm{d}x\mathrm{d}y,\tag{4.18}$$

with the convention that $\omega_{\alpha+4}=\omega_\alpha$ (α can be regarded as an arbitrary integer). Equivalently, we shall write

$$\int_{T_\alpha}\phi\,\mathrm{d}S=2A_\alpha\mathrm{e}^{\omega_{\alpha-1}}I_{00}^{\triangle}(\boldsymbol{a})\quad\text{with}\quad\boldsymbol{a}=(\omega_{\alpha+1}-\omega_{\alpha-1},\omega_{\alpha+2}-\omega_{\alpha-1}).\tag{4.19}$$

By following the same principle, the other integrals presented in (4.13) can also be expressed in a compact form using the reference coordinates system. Let us continue with the second integral:

$$\begin{aligned}\int_{T_\alpha}N_i\phi\,\mathrm{d}S &= 2A_\alpha\mathrm{e}^{\omega_m}\int_{\triangle}N_i\exp(x(\omega_i-\omega_m)+y(\omega_n-\omega_m))\,\mathrm{d}x\mathrm{d}y\\ &= 2A_\alpha\mathrm{e}^{\omega_m}I_{10}^{\triangle}(\boldsymbol{a})\quad\text{with}\quad\boldsymbol{a}=(\omega_i-\omega_m,\omega_n-\omega_m).\end{aligned}\tag{4.20}$$

At this point, it's useful to introduce a set of integers $\mathcal{S}$ which contains the four node numbers associated with the element, that is

$$\mathcal{S}=\{1,2,3,4\}.\tag{4.21}$$

So, in formula (4.20), the set of indices α, i, n and m must constitute the set $\mathcal{S}$, namely,

$$\{\alpha,i,n,m\}=\mathcal{S},\tag{4.22}$$

which signifies that α, i, n, m must be all different. Otherwise, the value of the integral will be equal to zero (this happens when $\alpha = i$). Similarly, the last integral in (4.13) becomes:

$$\begin{aligned}\int_{T_\alpha} N_i N_j \phi \,\mathrm{d}S &= 2A_\alpha \mathrm{e}^{\omega_r} \int_{\triangle} N_i N_j \exp(x(\omega_i - \omega_r) + y(\omega_j - \omega_r)) \,\mathrm{d}x\mathrm{d}y \\ &= 2A_\alpha \mathrm{e}^{\omega_r} I_{11}^{\triangle}(\boldsymbol{a}) \quad \text{with} \quad \boldsymbol{a} = (\omega_i - \omega_r, \omega_j - \omega_r),\end{aligned} \tag{4.23}$$

where

$$\{i, j, \alpha, r\} = \mathcal{S}. \tag{4.24}$$

Otherwise, the value of the integral will be equal to zero (this happens when $\alpha = i$ or $\alpha = j$). For particular case where $i = j$, we have

$$\int_{T_\alpha} N_i^2 \phi \,\mathrm{d}S = 2A_\alpha \mathrm{e}^{\omega_m} I_{20}^{\triangle}(\boldsymbol{a}) \quad \text{with} \quad \boldsymbol{a} = (\omega_i - \omega_m, \omega_n - \omega_m). \tag{4.25}$$

4.1.2 Integration over the reference triangle

By summarizing equations (4.19)-(4.25), we have introduced:

$$I_{mn}^{\triangle}(\boldsymbol{a}) = \int_{\triangle} x^m y^n \hat{\phi} \,\mathrm{d}x\mathrm{d}y, \tag{4.26}$$

where $\hat{\phi} = \exp(ax + by)$ and the vector $\boldsymbol{a} = (a, b)$. The new indices m, n are only varying from 0 to 2. Figure 4.2 shows the reference triangular domain. Since the dimension of the integral domain can be further reduced from surface to its edges by applying Green theorem as in formula (4.8), the surface integrals, therefore, become:

$$I_{mn}^{\triangle}(\boldsymbol{a}) = \frac{1}{\boldsymbol{a}^2} \Big[\underbrace{\boldsymbol{a} \cdot \int_\gamma x^m y^n \,\hat{\phi}\, \hat{\boldsymbol{n}} \,\mathrm{d}x\mathrm{d}y}_{I_{mn}^{\triangle 1}(\boldsymbol{a})} - \underbrace{\int_\gamma \nabla(x^m y^n) \cdot \hat{\boldsymbol{n}} \,\hat{\phi} \,\mathrm{d}x\mathrm{d}y}_{I_{mn}^{\triangle 2}(\boldsymbol{a})} + \underbrace{\frac{\boldsymbol{a}}{\boldsymbol{a}^2} \cdot \triangle(x^m y^n) \int_\gamma \hat{\phi}\, \hat{\boldsymbol{n}} \,\mathrm{d}x\mathrm{d}y}_{I_{mn}^{\triangle 3}(\boldsymbol{a})} \Big], \tag{4.27}$$

in which, the first line integral can be written in its closed-form expression:

$$\begin{aligned} I_{mn}^{\triangle 1}(\boldsymbol{a}) &= \sum_{\beta=1}^{3} \boldsymbol{a} \cdot \hat{\boldsymbol{n}}_\beta \int_{\gamma_\beta} x^m y^n \hat{\phi} \,\mathrm{d}x\mathrm{d}y \\ &= -b \int_{0[y=0]}^{1} x^m y^n \mathrm{e}^{ax} \,\mathrm{d}x - a \int_{0[x=0]}^{1} x^m y^n \mathrm{e}^{by} \,\mathrm{d}y + (a+b)\mathrm{e}^b \int_0^1 x^m (1-x)^n \mathrm{e}^{sx} \,\mathrm{d}x \\ &= -b I_{m,0}(a)\, \delta_{n,0} - a I_{n,0}(b)\, \delta_{m,0} + (a+b)\mathrm{e}^b I_{m,n}(s), \end{aligned} \tag{4.28}$$

in which $s = a - b$. The closed-form expression for the second integral can be expressed as

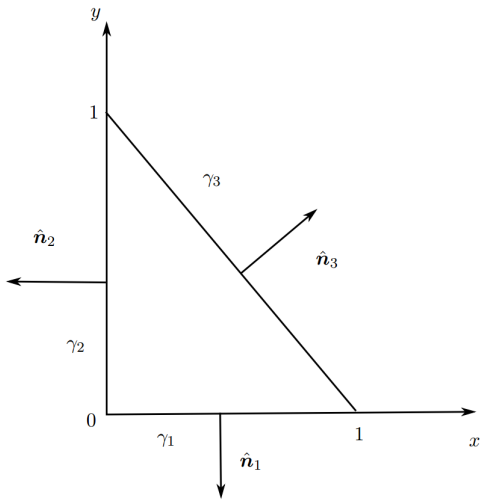

Fig. 4.2 The integration domain of the reference triangle in the local coordinates system.

$$
\begin{aligned}
I_{mn}^{\triangle 2}(\boldsymbol{a}) &= \sum_{\beta=1}^{3} \int_{\gamma_\beta} \nabla(x^m y^n) \cdot \hat{\boldsymbol{n}}_\beta \hat{\phi} \, \mathrm{d}x\mathrm{d}y \\
&= -\int_0^1 n x^m y^{n-1} \mathrm{e}^{ax} \, \mathrm{d}x - \int_0^1 m x^{m-1} y^n \mathrm{e}^{by} \, \mathrm{d}y \\
&\quad + \mathrm{e}^b \int_0^1 [n x^m (1-x)^{n-1} + m x^{m-1} (1-x)^n] \mathrm{e}^{sx} \, \mathrm{d}x \\
&= -I_{m,0}(a) \, \delta_{n,1} - I_{n,0}(b) \, \delta_{m,1} + \mathrm{e}^b [n I_{m,n-1}(s) + m I_{m-1,n}(s)].
\end{aligned} \tag{4.29}
$$

The closed-form expression of third integral can be derived based on the previous calculated integrals, which is given by

$$
I_{20}^{\triangle 3}(\boldsymbol{a}) = I_{02}^{\triangle 3}(\boldsymbol{a}) = \frac{2}{\boldsymbol{a}^2} I_{00}^{\triangle 1}(\boldsymbol{a}). \tag{4.30}
$$

To summarize, we have:

$$
I_{00}^{\triangle 1}(\boldsymbol{a}) = -bI_{0,0}(a) - aI_{0,0}(b) + (a+b)\mathrm{e}^b I_{0,0}(s) \tag{4.31}
$$

$$
I_{10}^{\triangle 1}(\boldsymbol{a}) = -bI_{1,0}(a) + (a+b)\mathrm{e}^b I_{1,0}(s), \tag{4.32}
$$

$$
I_{20}^{\triangle 1}(\boldsymbol{a}) = -bI_{2,0}(a) + (a+b)\mathrm{e}^b I_{2,0}(s), \tag{4.33}
$$

$$
I_{01}^{\triangle 1}(\boldsymbol{a}) = -aI_{1,0}(b) + (a+b)\mathrm{e}^b I_{0,1}(s), \tag{4.34}
$$

$$
I_{02}^{\triangle 1}(\boldsymbol{a}) = -aI_{2,0}(b) + (a+b)\mathrm{e}^b I_{0,2}(s), \tag{4.35}
$$

$$
I_{11}^{\triangle 1}(\boldsymbol{a}) = (a+b)\mathrm{e}^b I_{1,1}(s), \tag{4.36}
$$

and

$$I_{00}^{\triangle 2}(\boldsymbol{a}) = 0, \tag{4.37}$$
$$I_{10}^{\triangle 2}(\boldsymbol{a}) = -I_{0,0}(b) + \mathrm{e}^b I_{0,0}(s), \tag{4.38}$$
$$I_{20}^{\triangle 2}(\boldsymbol{a}) = 2\mathrm{e}^b I_{1,0}(s), \tag{4.39}$$
$$I_{01}^{\triangle 2}(\boldsymbol{a}) = -I_{0,0}(a) + \mathrm{e}^b I_{0,0}(s), \tag{4.40}$$
$$I_{02}^{\triangle 2}(\boldsymbol{a}) = 2\mathrm{e}^b I_{0,1}(s), \tag{4.41}$$
$$I_{11}^{\triangle 2}(\boldsymbol{a}) = -I_{1,0}(a) - I_{1,0}(b) + \mathrm{e}^b[I_{1,0}(s) + I_{0,1}(s)], \tag{4.42}$$

and

$$I_{00}^{\triangle 3}(\boldsymbol{a}) = I_{10}^{\triangle 3}(\boldsymbol{a}) = I_{01}^{\triangle 3}(\boldsymbol{a}) = 0, \tag{4.43}$$
$$I_{20}^{\triangle 3}(\boldsymbol{a}) = I_{02}^{\triangle 3}(\boldsymbol{a}) = \frac{2}{\boldsymbol{a}^2} I_{00}^{\triangle 1}(\boldsymbol{a}). \tag{4.44}$$

The line integrals expressed by the notation $I_{m,n}$ can be calculated explicitly as:

$$I_{0,0}(a) = \int_0^1 \mathrm{e}^{ax}\mathrm{d}x = \frac{(-1+\mathrm{e}^a)}{a}, \tag{4.45}$$
$$I_{1,0}(a) = \int_0^1 x\cdot\mathrm{e}^{ax}\mathrm{d}x = \frac{(1-\mathrm{e}^a+a\cdot\mathrm{e}^a)}{a^2}, \tag{4.46}$$
$$I_{2,0}(a) = \int_0^1 x^2\cdot\mathrm{e}^{ax}\mathrm{d}x = \frac{(-2+2\mathrm{e}^a-2a\cdot\mathrm{e}^a+\mathrm{e}^a\cdot a^2)}{a^3}, \tag{4.47}$$
$$I_{0,1}(a) = \int_0^1 (1-x)\cdot\mathrm{e}^{ax}\mathrm{d}x = \frac{-(1-\mathrm{e}^a+a\cdot\mathrm{e}^a)}{a^2}, \tag{4.48}$$
$$I_{0,2}(a) = \int_0^1 (1-x)^2\cdot\mathrm{e}^{ax}\mathrm{d}x = \frac{(-2a-a^2-2+2\mathrm{e}^a)}{a^3}, \tag{4.49}$$
$$I_{1,1}(a) = \int_0^1 (1-x)\cdot x\cdot\mathrm{e}^{ax}\mathrm{d}x = \frac{(a+2+a\cdot\mathrm{e}^a-2\mathrm{e}^a)}{a^3}. \tag{4.50}$$

For the purposes of avoiding round off errors, enhancing the numerical stability as well as saving computational time, Evans and Webster [42, 43] have shown that (4.45)–(4.47) can be obtained with the recurrence:

$$Q_n = \int_0^1 x^n\mathrm{e}^{ax}\mathrm{d}x, \tag{4.51}$$

$$Q_n = \left[\mathrm{e}^a - nQ_{n-1}(a)\right]/a, \tag{4.52}$$

where $Q_0 = (\mathrm{e}^a-1)/a$ and $Q_n(0) = 1/(n+1)$ when $a = 0$. The other integrals (4.48)–(4.50) can be easily recovered once all monomials have been computed.

4.1.3 Limit cases

During the process of deriving the closed-form expression for the integrals, it's imperative to consider exceptional cases that might lead to wrong results corrupted by round-off errors. In this section, three cases belonging to this category are pointed out. Meanwhile, the corresponding procedures for enhancing the robustness and accuracy of our algorithm are provided.

(a). For $k \approx 0$, this case physically means that two plane waves of the PUFEM basis happen to propagate in an opposite direction because $k = \kappa|\boldsymbol{d}' + \boldsymbol{d}''|$. In this case, the EIS is no longer suitable to calculate the integrals expressed in (4.1). Since integrals involved in (4.1) do not contain oscillating terms, standard Gauss-Legendre quadrature method becomes sufficient to accomplish the computational task. In fact, this particular case can be eliminated by carefully choosing the plane wave directions and taking into account small random variation, such that two wave directions will never be exactly opposite to each other.

(b). For $\boldsymbol{a} \approx 0$ in equation (4.26), this case characterizes the fact that the resulting plane wave direction is orthogonal to one of the surfaces of the PUFEM element. To tackle this problem, one approach is to use Taylor series expansion, which gives

$$
\begin{aligned}
I_{00}^{\triangle}(\boldsymbol{a}) &\approx \frac{1}{2} + \frac{a+b}{6} + \frac{a^2+b^2+ab}{24}, \\
I_{10}^{\triangle}(\boldsymbol{a}) &\approx \frac{1}{6} + \frac{b+2a}{24} + \frac{a^2}{40} + \frac{b^2}{120} + \frac{ab}{60}, \\
I_{20}^{\triangle}(\boldsymbol{a}) &\approx \frac{1}{12} + \frac{b+3a}{60} + \frac{a^2}{60} + \frac{b^2}{360} + \frac{ab}{120}, \\
I_{01}^{\triangle}(\boldsymbol{a}) &\approx \frac{1}{6} + \frac{2b+a}{24} + \frac{b^2}{40} + \frac{a^2}{120} + \frac{ab}{60}, \\
I_{02}^{\triangle}(\boldsymbol{a}) &\approx \frac{1}{12} + \frac{3b+a}{60} + \frac{a^2}{360} + \frac{b^2}{60} + \frac{ab}{120}, \\
I_{11}^{\triangle}(\boldsymbol{a}) &\approx \frac{1}{24} + \frac{a+b}{60} + \frac{a^2+b^2}{240} + \frac{ab}{180}.
\end{aligned}
$$

Alternatively, the second approach is to use numerical quadrature methods. Here, we favored the second approach for the following reasons: (1) Taylor series is not as stable as quadrature methods because the expected accuracy of Taylor series relies heavily on the number of terms in the expansion, (2) the oscillatory behavior of the plane waves is negligible when the plane waves are nearly orthogonal to the triangular surfaces, so quadrature methods are competent enough to address this scenario, (3) some highly efficient quadrature methods over the triangular domain, such as Wandzura's method (which is presented in Appendix B),

can be used to improve the computational efficiency.

(c). For $a \approx 0$ or $b \approx 0$ or $s \approx 0$ in equations (4.45) – (4.50), this case signifies that the resulting plane wave direction is orthogonal to one edge of the integration domain. Again, two numerical approaches can be employed to cope with this problem, namely, the Gauss quadrature and the use of the Taylor expansion. The performance of these two approaches is now discussed.

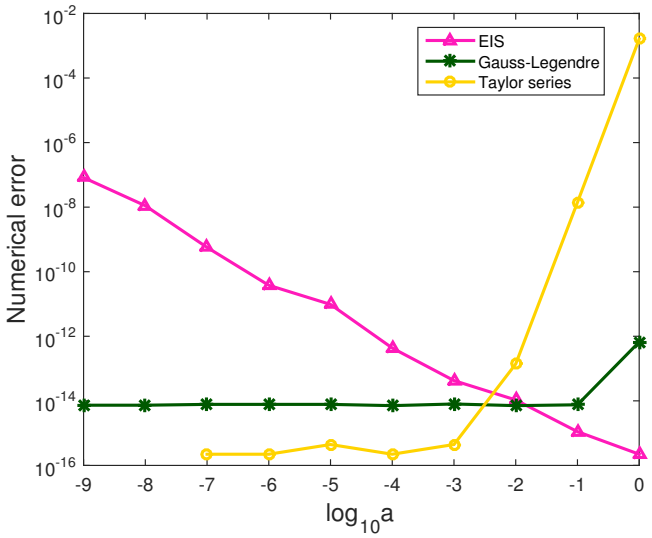

Fig. 4.3 The numerical error performances of three methods which are: Exact Integration Scheme (EIS), Taylor series expansion and Gauss-Legendre quadrature.

First, how to properly define the criteria of "close to zero" as above-mentioned is of great importance. For the sake of illustration, let us take one example of equation (4.48). Here, we need to compute:

$$I_{2,0}(a) = \int_0^1 x^2 \cdot \mathrm{e}^{ax} \mathrm{d}x. \tag{4.53}$$

We try to evaluate the accuracy performance related to the three methods which are EIS, Taylor series expansion and Gauss-Legendre quadrature, respectively. As shown in Figure 4.3, EIS provides an accuracy that decreases steadily when a goes to zero due to calculation errors and loss of significant digits. In contrast, the errors for the other approaches are maintained at a low level when a goes to 0. Most importantly, the intersection points among all these curves just provide the proper definition of "close to zero", which serves as a criteria to decide the most appropriate method to be used. In this example, it is shown in Figure 4.3 that the quadrature method takes precedence over the EIS when $a < 10^{-2}$, providing us with a stable accuracy level around 10^{-14}. By following this criteria, we can make sure that all

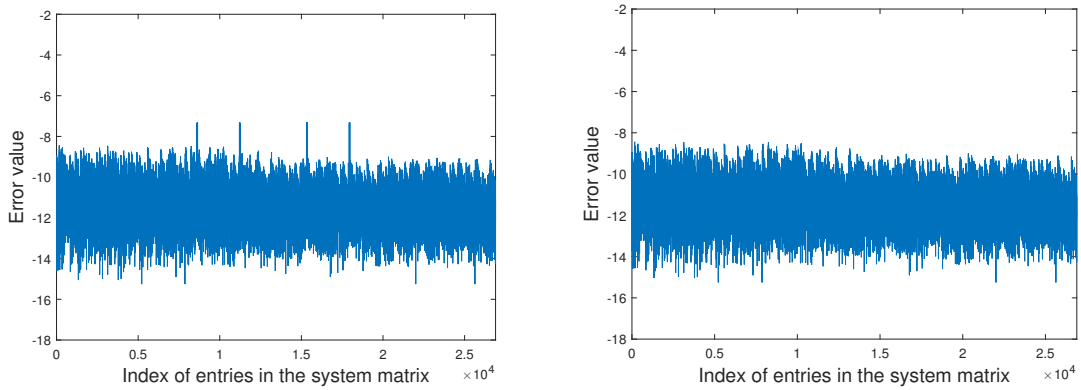

Fig. 4.4 Error value for all the entries of system matrix A obtained via the algorithm without considering the limit cases (Left), considering the limit cases (Right).

integrals involved can be computed with sufficient accuracy.

In order to verify the improvement in terms of accuracy of the resulting system matrix A, let us consider the case of a single element. The precision of the computed system matrix A is shown in Figure 4.4, here horizontal-axis represents each entry of the matrix, and vertical-axis corresponds to the level of accuracy which is evaluated via

$$\text{Error}(i,j) = |\mathsf{A}_{ij}^{comp} - \mathsf{A}_{ij}^{exact}|, \tag{4.54}$$

where, A_{ij}^{comp} refers to the computed entries of A, and A_{ij}^{exact} is simply computed via the Gauss-Legendre quadrature method that involves a sufficiently large number of gauss points, so that the values of A_{ij}^{exact} can be regarded as exact.

This investigation shows that, after the treatment of the particular limit cases, several numerical inaccuracies that may occur during the computational procedure have been successfully excluded. The whole computed PUFEM system matrix can be considered as nearly exact with errors that do not exceed 10^{-9}. It's worth stressing that a single bad entry of the system matrix can deteriorate the final solution. Now, it can be ensured that the developed 3D linear tetrahedron PUFEM element combining with 3D exact integration scheme is robust enough to provide highly accurate and stable numerical solutions for 3D acoustic problems.

4.1.4 Complexity estimation

The running time of the proposed algorithm should increase quadratically with Q (assuming the same number of plane waves per node). This is confirmed in Figure 4.5 (note calculations were performed on calcul.supmeca.fr, so running time is different from Table 4.2).

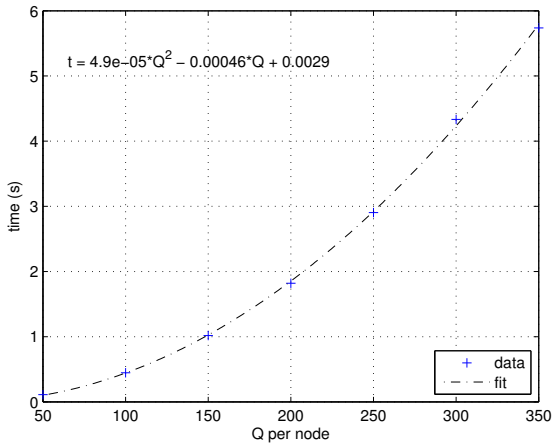

Fig. 4.5 Running time according to the plane wave number per node Q for one thread.

The analysis of the computational complexity of the PUFEM matrix can be done for the case of single regular tetrahedron. In the following, $N = Q^2$ corresponds to the total number of plane waves involved for a pair of indices (i, j). The computational cost depends on the number of faces (f) required in the volume integral and on the number of blocks (b) in the elementary matrix:

$$\mathsf{A}_{\mathsf{pum}} = \begin{pmatrix} \times & \times & \times & \times \\ & \times & \times & \times \\ & & \times & \times \\ & & & \times \end{pmatrix}. \tag{4.55}$$

There are 6 off-diagonal and 4 diagonal blocks. Note if $i = j$, only the upper part of the symmetric block matrix is computed with $N' = \frac{1}{2}Q(Q-1) + Q$ entries.

All details are presented in Table 4.1 and expressed in terms of the number of edge integral computation (eic) in (4.52). The integers appearing in Table 4.1 stems from the selection rule of equations (4.22) and (4.24). Besides, all recombination steps are omitted which renders a comparison with Gabard[43] easier. The author also presented an integration algorithm in the real coordinate system (which renders the algorithm quite different from the one developed here).

int.	Number of eic	eic calls for $Q = 50$
$\int_{\Omega_e} \phi \mathrm{d}\Omega$	$(6b \cdot N + 4b \cdot N') \cdot 4f \cdot 3e$	241 200
$\int_{\Omega_e} N_i \phi \mathrm{d}\Omega$	$(6b \cdot N + 4b \cdot N') \cdot 3f \cdot 3e$	180 900
$\int_{\Omega_e} N_j \phi \mathrm{d}\Omega$	$(6b \cdot N + 4b \cdot N') \cdot 3f \cdot 3e$	180 900
$\int_{\Omega_e} N_i^2 \phi \mathrm{d}\Omega$	$4b \cdot N' \cdot 3f \cdot 3e$	45 900
$\int_{\Omega_e} N_i N_j \phi \mathrm{d}\Omega$	$6b \cdot N \cdot 2f \cdot 3e$	90 000
	Total (in eic)	**738 900**

Table 4.1 Computational cost of the different volume integrals, expressed as number of call of the edge integral computation (e=edge, f=face, b=block) (Note the limit cases listed in Section 4.1.3 are ignored here).

4.1.5 Implementation and parallelism

The implemented version of the algorithm follows the description of the previous section : the *volume integral* is converted into *surface integral* over the reference triangle and then converted into *line integrals* where a closed-form solution is available. To speed up the integration, a fortran version has been implemented and linked as a mexfile to matlab core. This version takes advantage of multithread capability of modern CPU with openMP shared memory parallelism.

The double loop over the tetrahedron vertices is distributed over the available threads. This loop leads to 10 independent blocks when using the symmetry of the matrix $\mathsf{A}_{\mathsf{pum}}$. Note that the diagonal blocks are symmetric and only the half of the block matrix is computed. Each block has almost the same complexity and this simple approach leads to a rather good load balance between the threads. This approach is faster than using threaded version of BLAS3.

For a significant number of plane wave (say $Q > 150$), when the overhead time become small in comparison with the computational time, the scaling is almost linear up to 5 threads but suboptimal due to the overhead. As shown in Fig.4.6, with 5 threads, it takes less than 1 s per tetrahedron for 250 plane waves per node (test ran on calcul.supmeca.fr with 4 Intel(R) Xeon(R) CPU E5-2670 @ 2.60GHz with 16 core and 32 threads available).

A profile (valigrind/cachegrind) indicates that around 14% of CPU time is spent in the computation. The reminder of the computational time is spend mostly for the recombination.

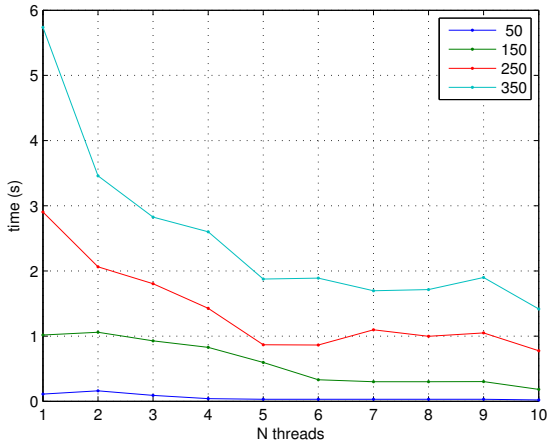

Fig. 4.6 Running time for several plane waves per node Q (50, 150, 250 and 350).

4.2 Convergence test

In this section, we shall investigate the numerical performance of the PUFEM in terms of accuracy and data reduction. Here the idea is to test the convergence of the method without modifying the coarse PUFEM mesh. In other words, we perform a q-refinement as opposed to a h-refinement. Through numerous numerical tests, it was observed that the PUFEM accuracy depends mainly on 2 parameters: the element size, call it h_j which is defined as the longest edge attached to node j and the number of wavelengths spanned by the element. In the following, we may assume that the number of plane waves attached to each node should vary quadratically like $(\kappa h_j)^2$, as in [64], so we put

$$Q_j = C(\kappa h_j)^2. \tag{4.56}$$

Coefficient C can also be viewed as a function of κh_j and it must be adjusted according to the configuration and expected accuracy. The behavior of C with respect to the non-dimensional frequency κh_j can be found by taking advantage of an artificial wave propagation problem for which the analytical solution is easily available. To do this, we consider an arbitrary incident plane wave propagating inside a single regular tetrahedron (the 4 edges are all of equal length $(h = h_j,\ j = 1, \cdots, 4)$). The boundary condition applied on each face is given by

$$\frac{\partial p}{\partial n} = \mathrm{i}\kappa(p - p_{inc}) + \frac{\partial p_{inc}}{\partial n}. \tag{4.57}$$

To be fair in our convergence test, the incident plane wave direction is always chosen as far as possible from the plane waves directions of the PUFEM basis, so that peculiar behaviors can be avoided. Otherwise, the computational error will move back and forth severely because

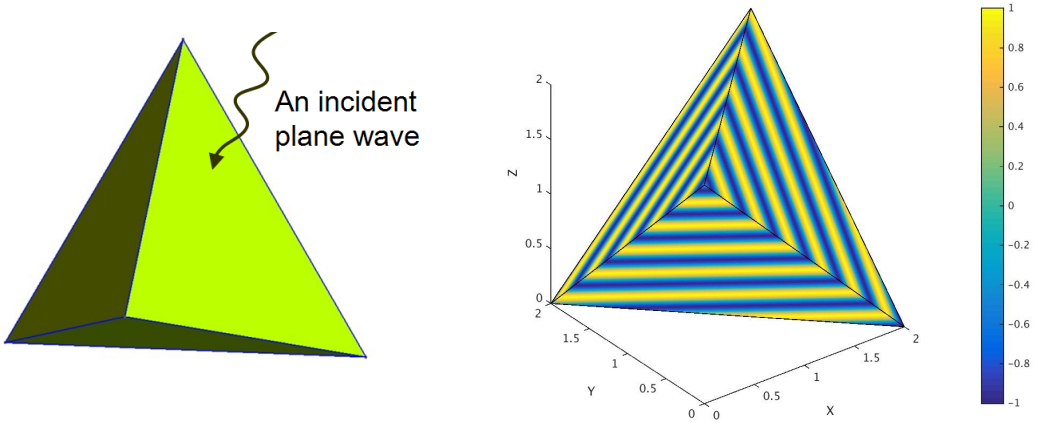

Fig. 4.7 The model (left), PUFEM solution (right), $\kappa h = 50$ and Q=276.

the final numerical solution that might be contained in the plane wave basis will give rise to excessive accuracy and vice versa. Figure 4.7 illustrates the PUFEM solution for $\kappa h = 50$ and the number of plane wave directions Q associated to each node is selected to be 276 (in total, $4 \times 276 = 1104$ are used to simulate the arbitrary plane wave in the element). We should be aware that the plane wave directions are computed through the algorithm presented in Section 2.3.2, with the aim to ensure a regularly spaced distribution. The numerical error is evaluated via L_2 error criteria on the boundary of the domain (here we have simply: $\Gamma = \partial\Omega_e$, as there is a single element, and $p_{ex} = p_{inc}$)

$$\varepsilon_2(\%) = \frac{\|p_{ex} - p_{pum}\|_{L_2(\Gamma)}}{\|p_{ex}\|_{L_2(\Gamma)}} \times 100. \tag{4.58}$$

The numerical error for the above-mentioned particular case ($\kappa h = 50$) is around 3%, which is satisfying for engineering purposes. In Table 4.2, we listed other cases with different parameters, all of them have been carried out to test the convergence behavior and verify the effectiveness of the method. Note that: (1) the condition number $Cond$ is estimated with Matlab by using the command `Condest`, and (2) the CPU time includes the computation of A and its inversion. Moreover, we also introduce the average discretization level n_λ in the context of 3D PUFEM, n_λ describes the number of variables needed to capture a single wavelength. For 3D problems, it is evaluated via:

$$n_\lambda = \lambda \left(\frac{N_{dof}}{\int_{\Omega_e} \mathrm{d}\Omega_e} \right)^{1/3}. \tag{4.59}$$

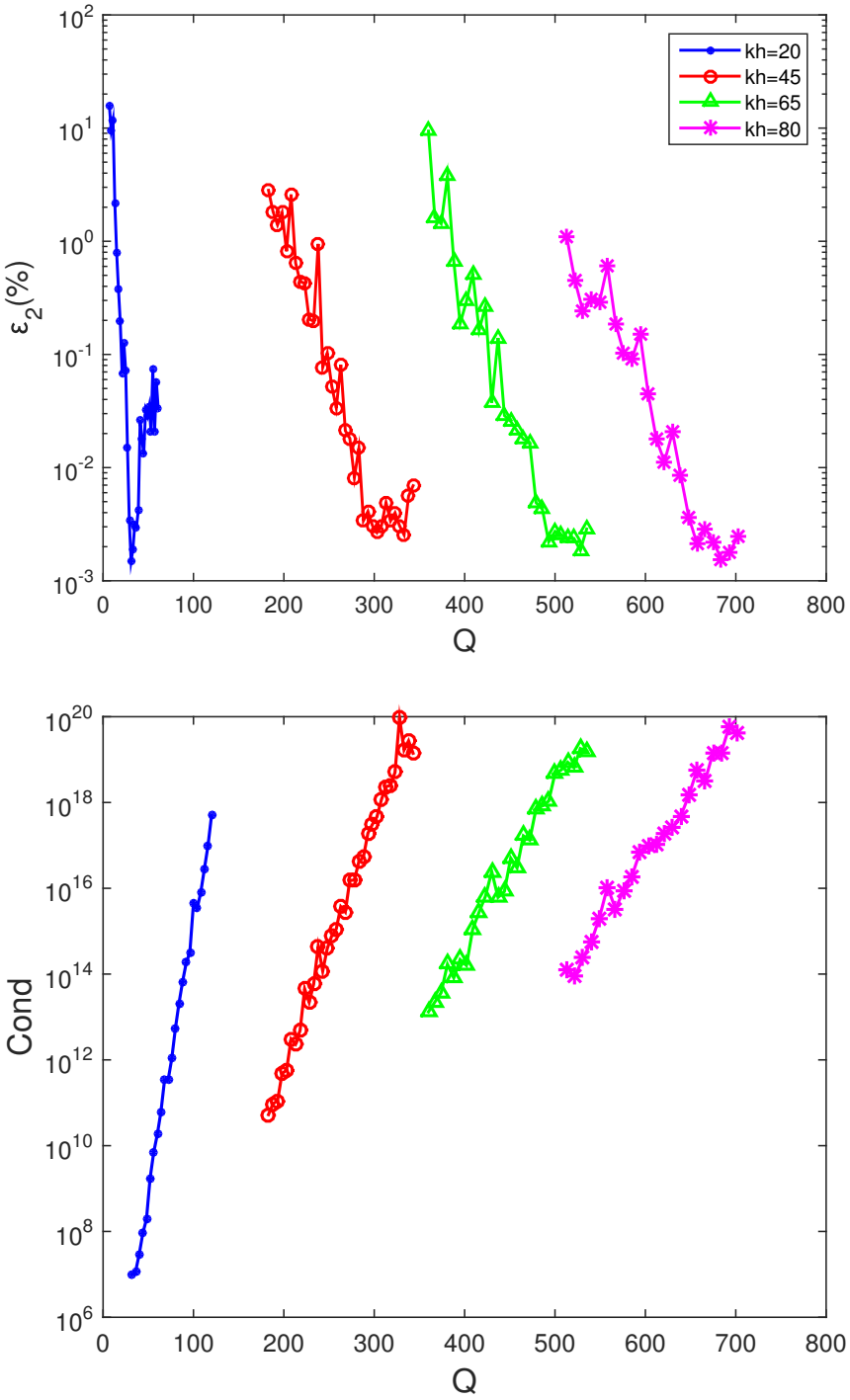

Fig. 4.8 The relative error (top), condition number (bottom), with respect to κh.

κh	C	Q	n_λ	h/λ	$\log_{10}$(Cond)	$\varepsilon_2(\%)$	CPU Time (s)
20	0.080	32	2.04	3.18	6.99	86.59	0.9
	0.130	52	2.39	3.18	9.24	9.21	1.3
	0.180	72	2.67	3.18	11.53	0.42	2.0
	0.230	92	2.89	3.18	14.26	0.020	3.4
	0.280	112	3.09	3.18	16.44	0.0036	4.5
	0.300	120	3.16	3.18	17.70	0.0057	5.1
45	0.090	183	1.62	7.16	10.72	2.82	10.9
	0.105	213	1.70	7.16	12.37	0.64	14.5
	0.120	243	1.78	7.16	14.07	0.077	18.5
	0.135	273	1.85	7.16	16.19	0.018	24.1
	0.150	303	1.91	7.16	17.67	0.0027	27.9
	0.164	333	1.98	7.16	19.23	0.0025	34.0
65	0.085	360	1.40	10.35	13.12	9.41	38.4
	0.094	395	1.45	10.35	14.33	0.19	45.8
	0.102	430	1.49	10.35	16.39	0.037	53.1
	0.110	465	1.53	10.35	17.22	0.018	63.6
	0.118	500	1.56	10.35	18.68	0.0027	74.3
	0.127	535	1.60	10.35	19.20	0.0029	85.2
80	0.080	513	1.28	12.73	14.09	1.08	77.7
	0.086	549	1.31	12.73	15.30	0.29	88.9
	0.091	585	1.34	12.73	16.28	0.092	100.2
	0.097	621	1.37	12.73	17.29	0.011	111.4
	0.103	657	1.39	12.73	18.75	0.0021	124.8
	0.108	693	1.42	12.73	19.78	0.0018	140.1

Table 4.2 Parameters for the performance analysis of the PUFEM (calculation ran on pilcam server at UTC).

After running a series of numerical tests, we managed to obtain the error performance with respect to different values of the non-dimensional parameter κh, varying from 5 to 80. For the sake of clarity, only four of them are displayed in Figure 4.8. We can observe that the region of convergence, once it begins, is relatively narrow, and the error drops abruptly until it reaches a plateau. This is mainly caused by the large condition number inherent to PUFEM with plane waves. A closer analysis reveals that the plateau is reached as soon as the condition number exceeds 10^{16} or 10^{17}.

Interestingly, if we draw a horizontal line corresponding to a specified error level (say 1% for instance), then the intersection points with all curves will give the required number of plane wave directions to attain this accuracy. Hence, by inverting formula (4.56), we

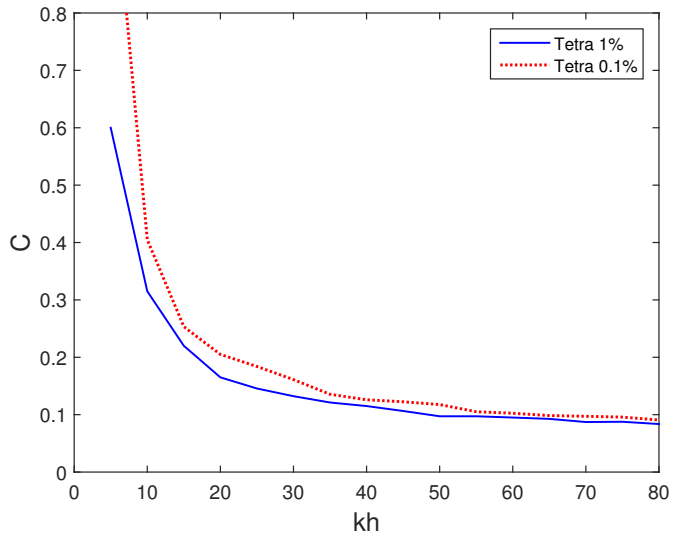

Fig. 4.9 Coefficient C and κh_j for 1% and 0.1% error range

can deduce the value of coefficient C that guarantees a certain prescribed accuracy. Values of coefficient C are reported in Figure 4.9 for 2 prescribed accuracies of $\varepsilon_2 = 1\%$ and $\varepsilon_2 = 0.1\%$. It can be observed that the value of C decreases and converges to a certain value around 0.1 for high frequency. More precisely, the curves show similar asymptotic behavior as $Q_j \sim 0.1(\kappa h_j)^2$ and the coefficient C ranges between 0.1 and 0.7 as long as the frequency is sufficiently high compared to the element length (i.e., $\kappa h > 10$). Therefore, the convergence of our PUFEM element has now been validated and verified.

The last observation suggests that an unreasonable number of plane waves are needed for small value of κh. In practice, it shows that PUFEM is not efficient enough for the "low-frequency" scenario when $\kappa h < 10$. In this case, the use of classical piecewise polynomial functions would be a better option. For sufficiently large frequency, or more precisely when $\kappa h > 10$, the PUFEM clearly outperforms standard piecewise polynomial FEM. From results of Figure 4.9, we can anticipate that the number of plane waves should vary quadratically with respect to κh as:

$$Q_j \approx (1 + D(\kappa h_j)^{-1}) \frac{(\kappa h_j)^2}{10}. \tag{4.60}$$

Since the number of degrees of freedom required by the PUFEM should grow cubically with frequency, the computational gain is expected to be very substantial at high frequency.

4.3 Note on SVD truncation for relatively low frequency

In this section, we shall focus specifically on the low frequency regime, that is when $\kappa h \leq 10$ (recall that h can be regarded as a characteristic length of the PUFEM element). This regime should be avoided, if possible, because the PUFEM performances in terms of data reduction are not optimal. Another important characteristic is that the numerical accuracy for the low frequency regime is usually more sensitive to the ill-conditioned nature of the PUFEM matrix. To identify this, we consider the model problem of the previous section with $\kappa h = 10$.

The error obtained with respect to the number of wave directions Q is shown in Figure 4.10 (left). The error decreases with Q as expected. However, the degradation of error can be observed when Q exceeds 30. In Figure 4.10 (right) is plotted the associated conditioning number of the system matrix, allowing us to identify more clearly the accumulation of round-off errors when the conditioning number exceeds 10^{16}. This is a typical feature of all wave-based methods. Fortunately, this issue can be mitigated by using SVD technique. Recall that we want to solve the complex algebraic system of the form,

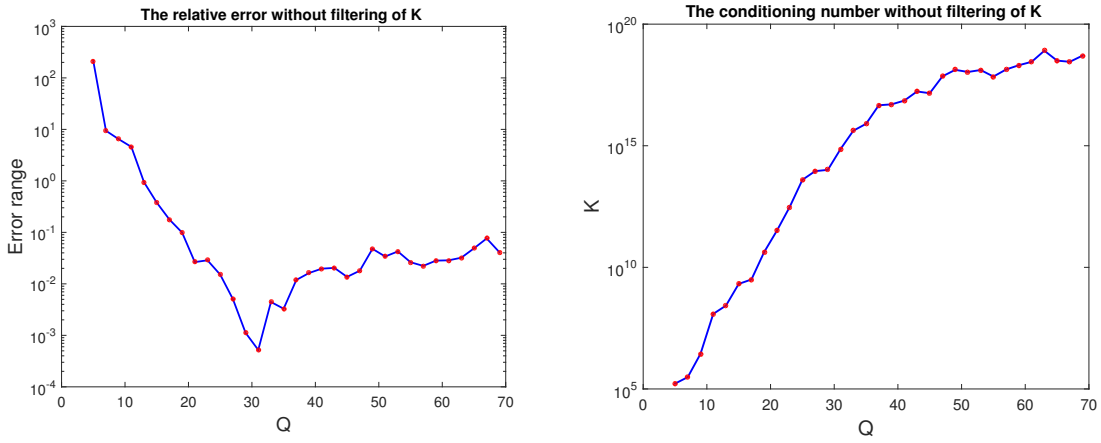

Fig. 4.10 The relative error $\varepsilon_2(\%)$ (left), condition number (right), for $\kappa h = 10$ in tetrahedron element

$$\mathsf{A}\mathsf{x} = \mathsf{b}. \tag{4.61}$$

The SVD decomposition consists in writing the matrix $\mathsf{A} = \mathsf{U}\mathsf{S}\mathsf{V}^{\mathsf{H}}$ where $(\mathsf{S})_{ii} = \sigma_i > 0$ are the singular values. The solution can be formally obtained as,

$$\mathsf{x} = \sum_{i \geq 1}^{N} \frac{\hat{b}_i}{\sigma_i} \mathsf{V}_i, \tag{4.62}$$

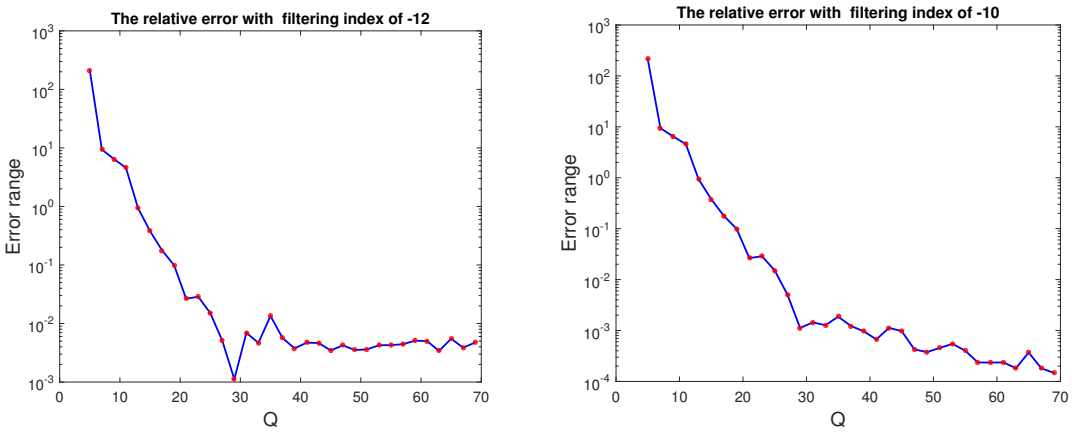

Fig. 4.11 The relative error after filtering process with $\delta = 10^{-14}$ (left), with $\delta = 10^{-12}$ (right), for $\kappa h = 10$ of the tetrahedron case.

where $\hat{b}_i = (\mathsf{U}^{\mathsf{H}}\mathsf{b})_i$ are the coordinates of the source vector in the orthogonal basis U. We recall that:

$$\mathrm{cond}_2(\mathsf{A}) = \|\mathsf{A}\|_2 \cdot \left\|\mathsf{A}^{-1}\right\|_2 = \sigma_1/\sigma_N. \tag{4.63}$$

The ill-conditioning of the matrix results from the accumulation of singular values that can be extremely small and will, therefore, affect the quality of the solution in equation (4.62). Thanks to a filtering process, we can access to a solution that is likely to be less corrupted by round-off errors:

$$\mathsf{x}_\delta = \sum_{i=1}^{r} \frac{\hat{b}_i}{\sigma_i}\mathsf{V}_i, \tag{4.64}$$

here, r corresponds to the rank of the filtered matrix:

$$\mathsf{A}_\delta = \mathsf{U}\mathsf{S}_\delta\mathsf{V}^{\mathsf{H}}, \tag{4.65}$$

and is defined so that $\sigma_{r+1} \leq \delta\sigma_1 < \sigma_r$. The thresholding parameter δ should be in accordance with the precision of matrix A. For an "exact" matrix, namely, calculated according to the machine precision, the most frequent proposed thresholding level is $\delta \sim 10^{-12}$. The lost of information caused by the truncation is tolerable as long as the coefficients $\hat{b}_{i>r}$ are negligible. Effect of the filtering can be seen in Figure 4.11, indicating that a threshold of about $\delta = 10^{-12}$ allows to reach $10^{-4}\%$ accuracy instead of around $10^{-1}\%$ accuracy with no filtering.

4.4 Numerical examples

As model problems,we shall consider a cubic-shaped cavity as shown in Figure 4.12. The first example concerns that of a prescribed velocity boundary condition on part of the wall cavity. Then, we shall investigate the effect of a monopole source located in the cavity. Two different numerical models are tested for the source point, and their numerical performance are compared. Finally, we shall also examine the effect of the location of the point source (which could be extremely close to the corner of the cavity) on the accuracy. In all cases, the cavity is a cube of size 2 m $\times$2 m $\times$2 m with the longest edge $h_{max} = 2$ m, and the model is partitioned into 24 PUFEM elements and 14 nodes (see Figure 4.12).

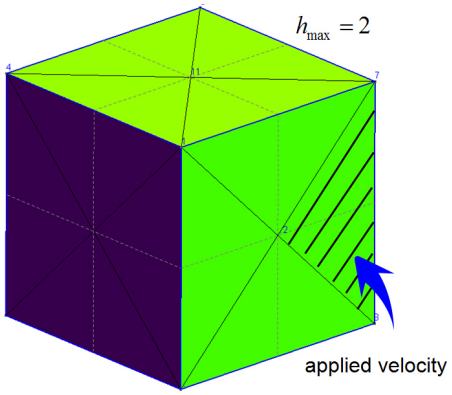

Fig. 4.12 The model problem.

4.4.1 Response to a prescribed velocity at the wall

In the first numerical example shown in Figure 4.12, we apply a velocity boundary condition $\partial p/\partial n = 1$ on a triangular area of a specified surface of the cube. Here, an initial guess for the number of plane wave functions Q can be taken by following the selection criteria (4.56), where the coefficient C can be evaluated through the two curves of Figure 4.9. By choosing the curve pertaining to an expected accuracy (here 0.1 % and 1%), we can anticipate that the numerical solution should be delivered with similar precision. For the sake of illustration, Figure 4.13 displays both the real and imaginary part of the computed fluid pressure for the non-dimensional value $\kappa h_{max} = 60$. This result was computed by taking $Q_{max} = 958$ (this corresponds to the number of plane waves attached to the 8 vertices of the cube, whereas the other 6 nodes only involve 476 plane wave directions).

This particular example does not possess an analytical solution and the numerical error can not be estimated with sufficient confidence through the ideal criteria (4.58). Considering the fact that the exact solutions to this problem is purely real, we, therefore, propose an new estimation of the error which is to examine the imaginary part of the numerical solution. As shown in Figure 4.13, the correctness of the results can be verified if the imaginary part is nearly equal to 0. Hence, the imaginary part can be treated as an error indicator and we introduce:

$$\varepsilon(\%) = \frac{\|p_{imag}\|_{L_2(\Gamma)}}{\|p_{real}\|_{L_2(\Gamma)}} \times 100, \tag{4.66}$$

where, p_{imag} and p_{real} refer to the imaginary and the real part of the computed pressure, respectively. In this example, it can be checked that the relative error is around 0.6% by using this new error indicator (4.66) (we will compare this error indicator with the former criteria (4.56) in the next example).

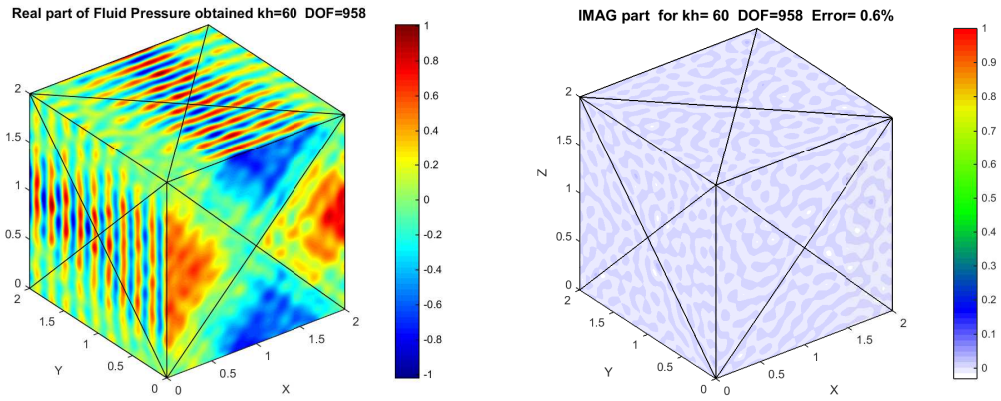

Fig. 4.13 High frequency solution with $\kappa h_{max} = 60,\ Q_{max} = 958$: PUFEM solution (left), the imaginary part of the numerical solution serves to indicate the accuracy of the result (right).

Here, only around $15,000$ dof are used in our PUFEM numerical model for $\kappa h_{max} = 60$, which signifies that around 10 wavelengths are spanned in the element because $h_{max}/\lambda \approx 10$. Therefore, if we use classical FEM which adopts piecewise linear or quadratic interpolation to deal with the same case containing around 10 wavelengths, then at least $(10n_\lambda)^3$ dof are required to attain sufficient accuracy level of the solution, here n_λ is the number of dof necessary to capture one wavelength in traditional FEM. For instance, taking $n_\lambda = 15$ leads to an estimate of more than two millions FE nodes!

4.4.2 Response to a point source

The second example is related to the simulation of a sound field caused by a monopole source placed in the cavity, as shown in Figure 4.14 (left). The boundary Γ is assumed to be a rigid wall, on which $\partial p/\partial n = 0$ is prescribed. In this case, the numerical tests are carried out based on two different numerical models and their performance and advantage are compared. The analytical solution to this problem is available in reference [62].

Model 1: computation of the total field

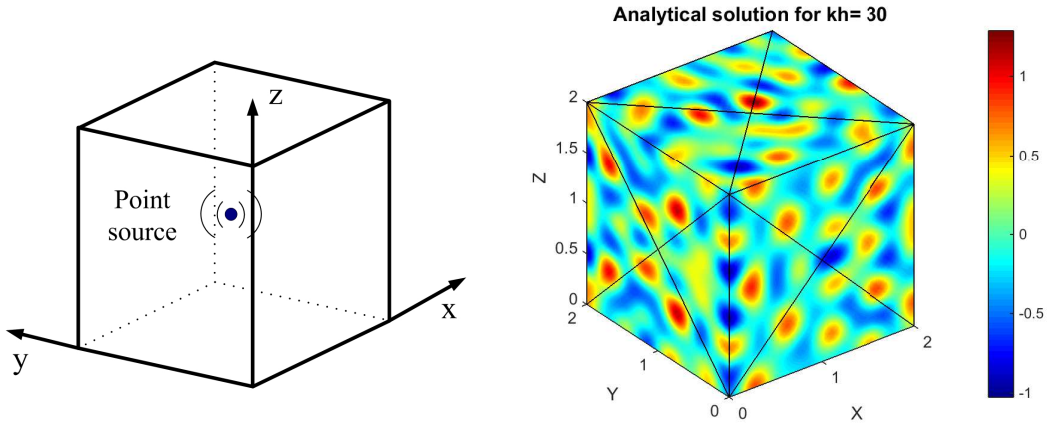

Fig. 4.14 The building model (left), and its analytical solution for $\kappa h_{max} = 30$ (right).

In this first model, we attempt to solve the point source problem by simply taking into account the Dirac function on the right-hand side of the wave equation. Hence, we seek for the total pressure field satisfying,

$$\Delta p + \kappa^2 p = A\delta(\boldsymbol{x} - \boldsymbol{x}_0), \tag{4.67}$$

where A is the amplitude of the monopole source and $\boldsymbol{x}_0$ stands for the source position inside the cube. In this example, we set $\boldsymbol{x}_0 = (0.9, 0.8, 1)$ which is near the center of the cavity. The analytical solutions to this physical model is shown in Figure 4.14.

To evaluate the computational performance of the first model, we consider the case where $\kappa h_{max} = 30$ and three numerical tests are investigated by taking respectively $Q_{max} = 278$, 417 and 556 plane wave directions. Results are conveniently displayed in Figure 4.15. They show poor convergence and it was observed that errors can not go below 20% regardless of the number of wave directions. This limiting factor which prevents us from obtaining a converged result stems from the inability of the plane wave basis to simulate a singular sound

field. The next model will be devoted to tackle this issue. Note that the error is measured by using criteria (4.58), the imaginary part allows us to visualize the numerical error in the computational domain.

Model 2: computation of the scattered field

The main idea of the alternative model is to split the pressure p into two terms: $p = p_i + p_{sc}$ where p_i and p_{sc} represent the incident wave pressure and the scattered wave pressure, respectively. The modified governing equations and boundary conditions can then be formulated as:

$$\begin{cases} \Delta p_i + \kappa^2 p_i = A\delta(\boldsymbol{x} - \boldsymbol{x}_0) & \text{in } \Omega, \\ \Delta p_{sc} + \kappa^2 p_{sc} = 0 & \text{in } \Omega, \\ \dfrac{\partial p_{sc}}{\partial n} = -\dfrac{\partial p_i}{\partial n} & \text{on } \Gamma. \end{cases} \tag{4.68}$$

The first equation describes the incident sound field p_i caused by a monopole source, which is represented by applying a Dirac function at position $\boldsymbol{x}_0$ on the right side of the inhomogeneous Helmholtz equation. Here, we shall take the free-field Green function:

$$p_i = A\,\frac{\mathrm{e}^{\mathrm{i}\kappa r}}{4\pi r}. \tag{4.69}$$

Now, applying PUFEM for the scattered field leads to a boundary term of the form,

$$\int_\Gamma \frac{\partial p_{sc}}{\partial n} \cdot \delta p \, d\Gamma = -\int_\Gamma \frac{\partial p_i}{\partial n} \cdot \delta p \, d\Gamma, \tag{4.70}$$

The boundary integral involves the normal direction of the incident field,

$$\frac{\partial p_i}{\partial n} = A\,\frac{\mathrm{e}^{\mathrm{i}\kappa r}}{4\pi r}(\mathrm{i}\kappa - \frac{1}{r})\frac{\boldsymbol{x} - \boldsymbol{x}_0}{r} \cdot \boldsymbol{n}, \tag{4.71}$$

where r is the distance from source point $\boldsymbol{x}_0$ to the point $\boldsymbol{x}$, and the amplitude of point source A is chosen to be 1.

To evaluate the computational performance of this model, we consider the case where $\kappa h_{max} = 30$ which is identical to the previous model, and three numerical tests are carried out by taking $Q_{max} = 139$, 278 and 417, respectively. All the computed results are depicted in Figure 4.16. Clearly, the second numerical model shows a much better performance and

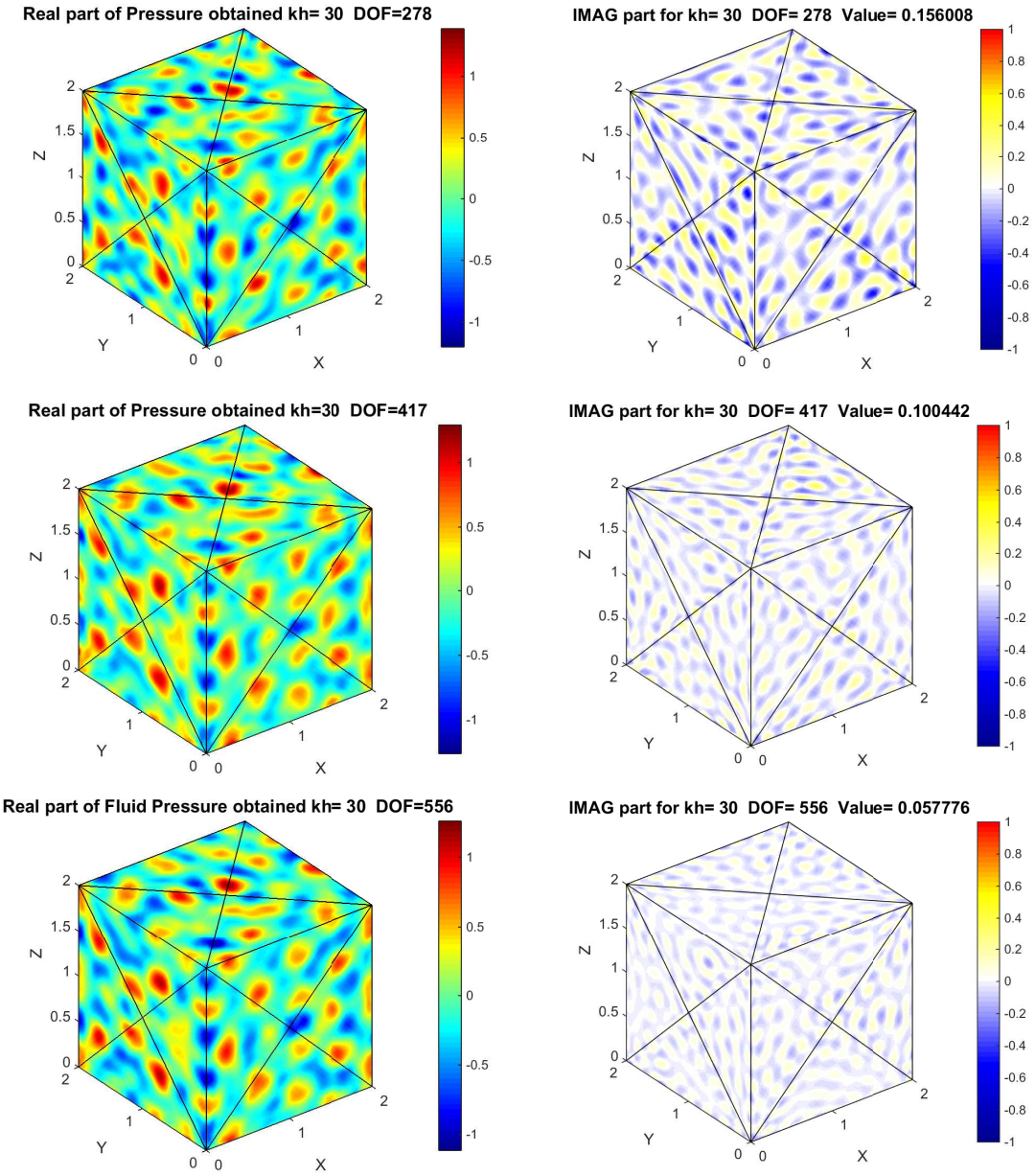

Fig. 4.15 Response in the cavity due to a point source represented by directly applying a Dirac function: PUFEM solution with $Q_{max} = 278$ and $\varepsilon_2 = 51\%$ (top), PUFEM solution with $Q_{max} = 417$ and $\varepsilon_2 = 39\%$ (middle), PUFEM solution with Q_{max}=556 and $\varepsilon_2 = 28\%$ (bottom).

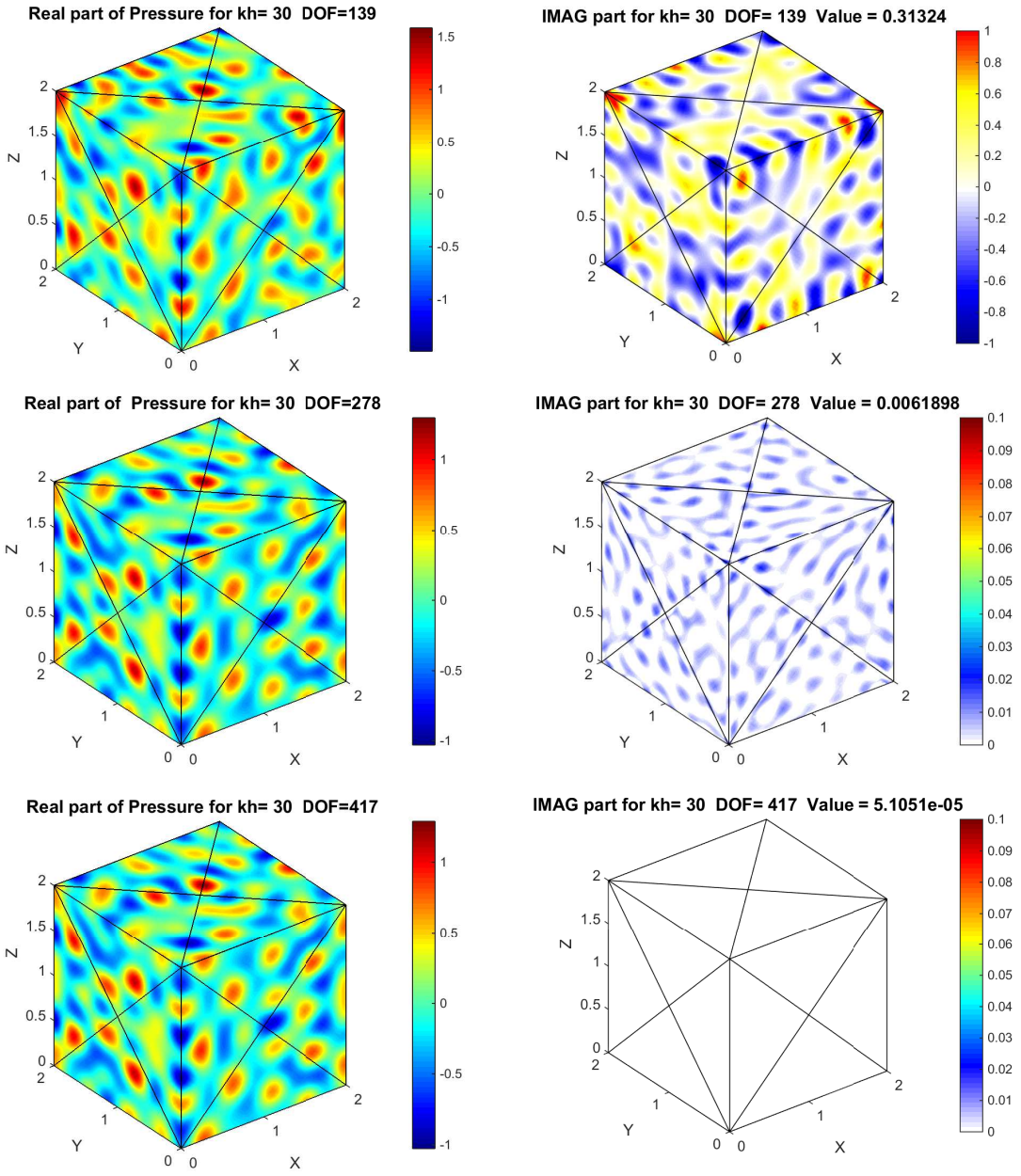

Fig. 4.16 Response in the cavity due to a point source by splitting the total pressure p into p_i and p_{sc}: PUFEM solution with $Q_{max} = 139$ and $\varepsilon_2 = 212\%$ (top), PUFEM solution with $Q_{max} = 278$ and $\varepsilon_2 = 0.93\%$ (middle), PUFEM solution with $Q_{max} = 417$ and $\varepsilon_2 = 0.29\%$ (bottom).

very fast convergence rate. In order to better illustrate this, the comparison between the two models is made and shown in Figure 4.17.

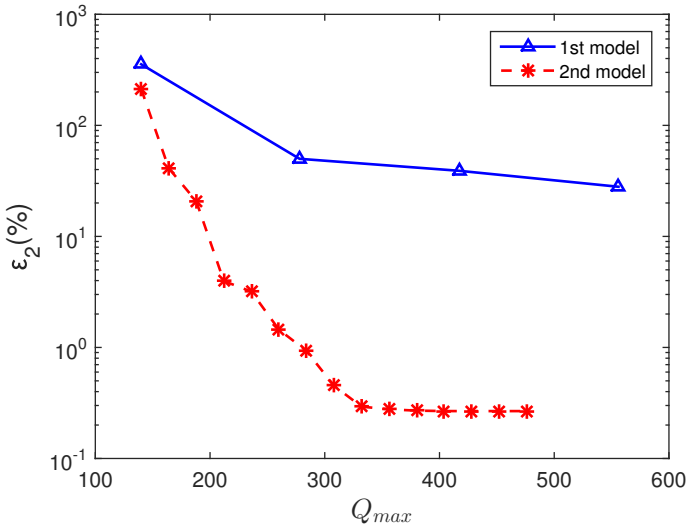

Fig. 4.17 The accuracy performance using two different numerical models for the interior point source problem with $\kappa h_{max} = 30$.

It can be seen from Figure 4.17 that the numerical error for both models is decreasing with respect to the number of plane wave directions. However, the first model presents a much slower convergence rate due to the shortcomings of the model mentioned above. Only $Q_{max} = 169$ wave directions are required to reach 30% of accuracy for the second model while at least, more than 556 directions are needed for the first model to achieve the same accuracy. It may also be observed that the error reaches a plateau around 0.3% regardless of the number of wave directions. This error stems simply from the fact that the "exact" solution p_{ex} is calculated with a finite number of cavity modes [62]. So the analytical solution is not exact.

To verify this, we shall now adopt the error indicator given by equation (4.66). The computed results, given in Figure 4.18, demonstrate the true performance of the PUFEM (red curve) and that the indicator based on the imaginary part provides a very good estimation of the error. In principle, this indicator can be used whenever the solution to the problem is purely real.

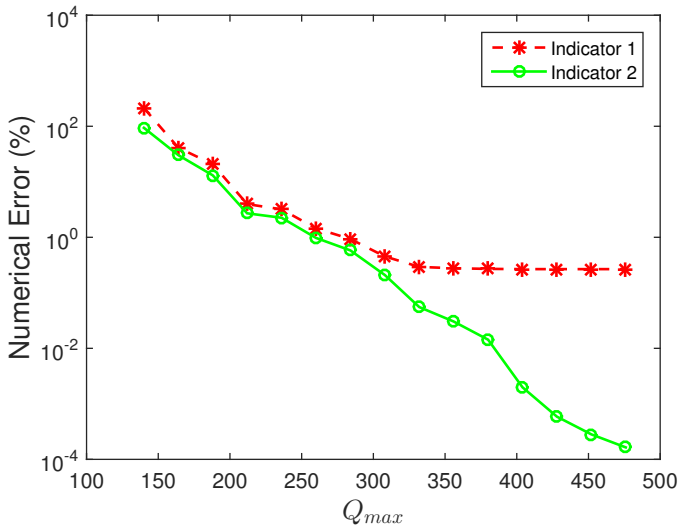

Fig. 4.18 The accuracy performance using two different error indicators (indicator 1 (4.58), indicator 2 (4.66)) for the interior point source problem with $\kappa h_{max} = 30$.

4.4.3 Criteria for more realistic problems

The aim of this subsection is to come up with a confident criteria for the plane wave enrichment. In section 4.2, it was advocated that the number of wave directions attached to node j should vary quadratically as $Q_j = C(\kappa h_j)^2$. In the context of a simple artificial problem, the coefficient C reported in Figure 4.9 was found to behave like equation (4.60). For more realistic problems such as those of section 4.4, it is useful to provide similar formulas. To achieve this, a series of numerical tests have been carried out for the cubic cavity problem. In Figure 4.19 are reported the values of coefficient C with respect to κh_j to ensure that the numerical error should be around 1%.

The observation is that, although the enrichment criteria depends on the problem, the three curves show very similar tendencies. The biggest derivation comes from the interior point source problem, for which the number of wave directions must be doubled compared to the ideal scenario. For a given coarse mesh, the enrichment criteria given by Figure 4.19 can be used to provide an "initial enrichment strategy" as numerical examples of the next sections will show.

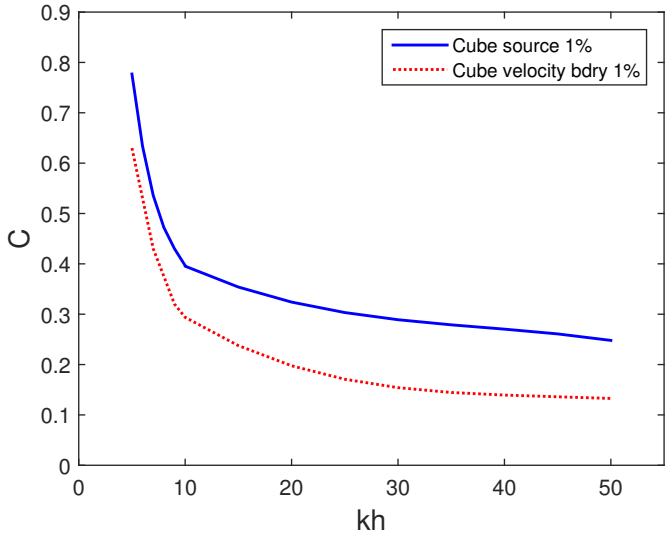

Fig. 4.19 Coefficient C with respect to κh_{max}: the monopole source in the cubic cavity with 1% error range (blue curve), the prescribed velocity boundary condition with 1% error range (red curve).

4.5 Concluding remarks

In this chapter, a 3D Exact Integration Scheme is presented for the accelerated and accurate computation of highly oscillatory integrals arising from the PUFEM matrix coefficients associated with the 3D Helmholtz equation. It's shown that, through successive use of Green's theorem, volume integrals have closed-form expressions in which no integration is involved. Through convergence tests, a criteria for selecting the number of plane waves is proposed. It is shown that this number only grows quadratically with the frequency thus leading to a drastic reduction in the total number of degrees of freedoms in comparison to classical FEM. The method has been verified for two numerical examples. In both cases, the method is shown to converge to the exact solution. For the cavity problem with a monopole source located inside, we tested two numerical models to assess their relative performance. In this scenario where the exact solution is singular, the number of wave directions has to be chosen sufficiently high to ensure that results have converged. The numerical model which consists in separating the total pressure p into a singular incident field p_i and a more regular scattered field p_{sc} allow us to circumvent this limiting factor. Finally, we proposed enrichment strategies based on the criteria (4.66).

Chapter 5

PUFEM with porous absorbers

A wide range of applications of absorbing materials can be found in the building sector, the aviation and vehicle industries and so on, in order to control the inevitable sound and noise issues. Optimum efficiency and flexible solutions are often regarded as the important standards in the designs and applications of porous materials. In this chapter, we focus on the application of the PUFEM element combined with EIS for the analysis of interior sound field problems where absorbers are present. The outline of this chapter is organized as follows:

Section 5.1 briefly reviews several common models of absorbing materials usually encountered. Section 5.2 presents the application of the PUFEM for a cavity problem with acoustically treated walls (surface impedance). In Section 5.3, the PUFEM is extended further to simulate the acoustic waves in a porous material modeled as a equivalent homogeneous fluid. The numerical performances and efficiency are also analyzed. Concluding remarks are given in Section 5.4.

5.1 Absorbing material

5.1.1 Acoustic surface impedance

Definition

Impedance is one of the most important concepts in acoustics. In the mechanical field, the common definition of the impedance refers to the ratio of the complex amplitude of a sinusoidally varying force, moment or couple, to the complex amplitude of the resulting velocity at a point on a vibrating object. This specific ratio also can be called the mechanical impedance in a driving mechanical system. It's usually a function of frequency and consists

of a complex number of which the real part origins from the damping or friction system and the imaginary part results from the stiffness and mass systems. Similarly, the acoustic surface impedance represents the ratio between the complex amplitude of harmonic fluid pressure (associated force acting on a surface) to the normal fluid particle velocity or volume velocity passing through that surface. This ratio is generally complex and conventionally denoted by Z. Under the assumption of plane wave motion in which both quantities are uniformly distributed over the cross-section of the tube, the specific acoustic impedance over a unit-area surface can be defined as

$$Z = \frac{p}{v_n}, \tag{5.1}$$

where v_n is the normal component of the fluid velocity directed into the surface. It physically describes how much sound pressure acting on the wave over a unit-area is needed for driving the fluid particle to attain a unit velocity.

Boundary representations of porous absorbers

Typically, there exists several different boundary representations of porous absorbers in the field of room acoustic simulation according to the properties and geometries of the porous material, this includes the simplest impedance boundary condition as well as the more complicated Biot's model taking into account skeleton and fluid phase motions. The use of acoustic surface impedance to simulate the sound field in an enclosed cavity with porous absorber materials on its boundary is only appropriate under some specific conditions. It has been widely acknowledged in the acoustic community that the acoustic reflection characteristics of room boundary can be fully described by its acoustic surface impedance Z if the boundary is "locally reacting". According to Mechel [87], the absorber can be viewed as "locally reacting" if it satisfies the following conditions:

- The interaction between the incident sound and absorber is fully described by the absorber characteristics at the specific location where we observe p and v_n,
- Sound propagation inside the absorber is only possible in the normal direction to the boundary surface.

Under these assumptions, the acoustic surface impedance Z can be specified as a boundary condition for the Helmholtz equation, and it is totally independent of the incident sound field and its angle of incidence. In practice, the given absorber can be regarded as "locally reacting" when the porous material possesses high flow resistivity, or in the case of a perforated plate backed with honeycomb structures for instance. Otherwise, the response of the porous absorbers will depend on the angle of incidence and show a growing damping once the

incident angle increases. This problem can be partly overcome in the context of a diffuse field as shown [60]. The use of a diffuse field impedance indicates that we take into account the special behavior of the laterally reacting material, so the average damping of the porous absorber will not be underestimated in comparison with the normal incidence impedance.

5.1.2 Equivalent Homogeneous Fluid (EHF)

A common and practical approach adopted by many researchers for describing the porous material is to regard it as an equivalent homogeneous fluid (or EHF), this concept was first proposed by Rayleigh [109] who considered the porous material as a rigid or motionless frame with parallel and identical cylindrical pores. This idea was further worked out and extended in the work of Zwikker and Kosten [130], Attenborough [6], Champoux and Stinson [25]. The basic assumption is that only one longitudinal sound wave can propagate through this porous material model with very stiff skeleton. In other words, porous absorber behaves like the fluid with an adjusted density and bulk modulus, and the elastic and inertial contribution of the solid phase are not taken into account. The quantities of the fluid density ρ_p and the dynamic fluid bulk modulus K_p used to describe the remaining fluid phase in our study are calculated form the frequency-dependent Johnson-Champoux-Allard's expression [2] (which is presented in Appendix A).

5.1.3 Biot's model

However, the EHF assumption is not suitable for a certain category of absorbent materials such as polymer foams whose solid structure possess a finite stiffness, if the sound absorbing materials has a high flow resistivity and a high decoupling frequency, or the absorbing materials are coupled to a vibrating structure. In these cases, the elasticity of the skeleton cannot be neglected due to the fact that there exists various interaction between the solid phase and fluid phase. Therefore, a set of coupled differential equations which describe the movement of both phases and their interaction have to be considered.

The model based on the Biot theory [19] is of great value. It fully describes the propagation of elastic and pressure waves in porous materials, mainly stating that a transversal wave and a longitudinal wave can exist in an isotropic solid and a longitudinal wave can propagate in the fluid. More detailed information and discussion can be found in the book of Allard and Atalla [2].

The numerical solution of Biot's equations is usually achieved with the finite element method

(FEM) and this has been extensively used by many researchers [102, 5, 4]. In this regard, the mixed $(\boldsymbol{u}, p_p)$ formulation of Atalla et al. [5] offers the great computational advantage of reducing the number of degrees of freedom as well as easing the transmission conditions at the air-porous interface. The numerical simulation of Biot's waves in poroelastic materials has also been investigated in the context of wave-based methods [44, 37, 36, 100, 28] (see Chapter 1), though these developments are restricted to two-dimensional domains.

5.2 PUFEM with surface impedance

Two numerical examples involving porous absorbers are considered. The first example is concerned with a reverberant room where we use a normal surface impedance boundary to represent the absorber material on the roof. We attempt to investigate the wave propagation field inside the reverberant room incited by a monopole source which is placed near the center of the room. We use a simplified geometrical model of the reverberant room shown in Figure 5.1, and the porous absorber is assumed to be "locally reacting". This numerical model involves 19 nodes and is partitioned into 37 tetrahedron elements, here the characteristic length is still set to be longest edge of the PUFEM mesh which is $h_{max} \approx 3.27$ m.

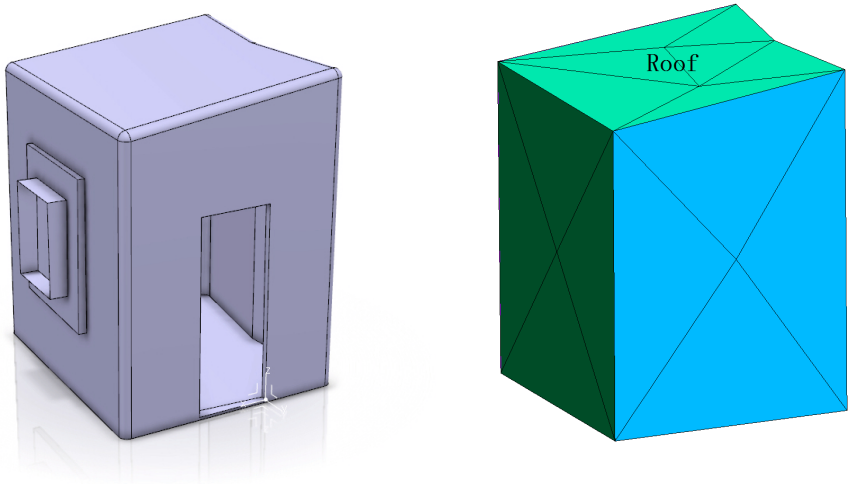

Fig. 5.1 The physical and numerical models of reverberant room: the realistic geometry (left), and the simplified numerical model with PUFEM mesh (right).

The governing equations and boundary conditions is given in terms of the scattered pressure p_{sc}:

$$\begin{cases} \Delta p_{sc} + \kappa^2 p_{sc} = 0 & \text{in } \Omega, \\ \dfrac{\partial p_{sc}}{\partial n} = \tilde{Y} p_i + \tilde{Y} p_{sc} - \dfrac{\partial p_i}{\partial n} & \text{on } \Gamma_1, \\ \dfrac{\partial p_{sc}}{\partial n} = -\dfrac{\partial p_i}{\partial n} & \text{on } \Gamma_2, \end{cases} \tag{5.2}$$

where, the p_i represents the incident pressure due to a point source, Γ_1 refers to the roof surface where porous absorber are used, and Γ_2 are the remaining rigid surfaces. In these equations, $\tilde{Y}$ corresponds to the normalized surface admittance, $\tilde{Y} = \mathrm{i}\kappa Z_0/Z$ where Z is the surface impedance, here $Z_0 = \rho_0 c_0$ stands for the characteristic acoustic impedance of the air. Note that the two surface integrals (see equations (4.69) and (4.71)) due to the Neumann boundary condition on Γ_1 and Γ_2 do not have closed-form expressions, and the Gaussian quadrature method must be employed (see Appendix B).

5.2.1 Numerical results

Since the analytical solution is impossible to obtain, the error evaluation criteria proposed in Chapter 4 without involving exact analytical solution becomes the only option, this criteria is reminded here:

$$\varepsilon(\%) = \frac{\|p_{imag}\|_{L_2(\Gamma)}}{\|p_{real}\|_{L_2(\Gamma)}} \times 100. \tag{5.3}$$

However this error estimate is limited to the problems with real-valued solutions. These solutions, although not physical because there is no absorption, shall serve to evaluate the PUFEM numerical error. To illustrate this, let us consider a point source at $\boldsymbol{x}_0 = (0, 0, 0.5)$ (which is near the center of the room) and a surface impedance $Z = Z_0(2 + 2\mathrm{i})$. The first step is to consider the real-valued version to this problem by taking a purely imaginary impedance $Z = Z_0 2\mathrm{i}$. Numerical results are shown in Figure 5.2 by increasing the number of wave directions per node (here $\bar{Q}$ indicates the average value over the whole PUFEM mesh). The error indicators are also reported showing very good convergence as expected.

Figure 5.3 shows the absolute values of the pressure corresponding to an absorbing impedance condition $Z = Z_0(2 + 2\mathrm{i})$ with the same PUFEM parameters ($\bar{Q} = 133$ and $\bar{Q} = 177$). When $\bar{Q} = 177$, the results have clearly converged (this was checked by increasing $\bar{Q}$), and it is anticipated that errors should be comparable as for the real-valued solution of Figure 5.2.

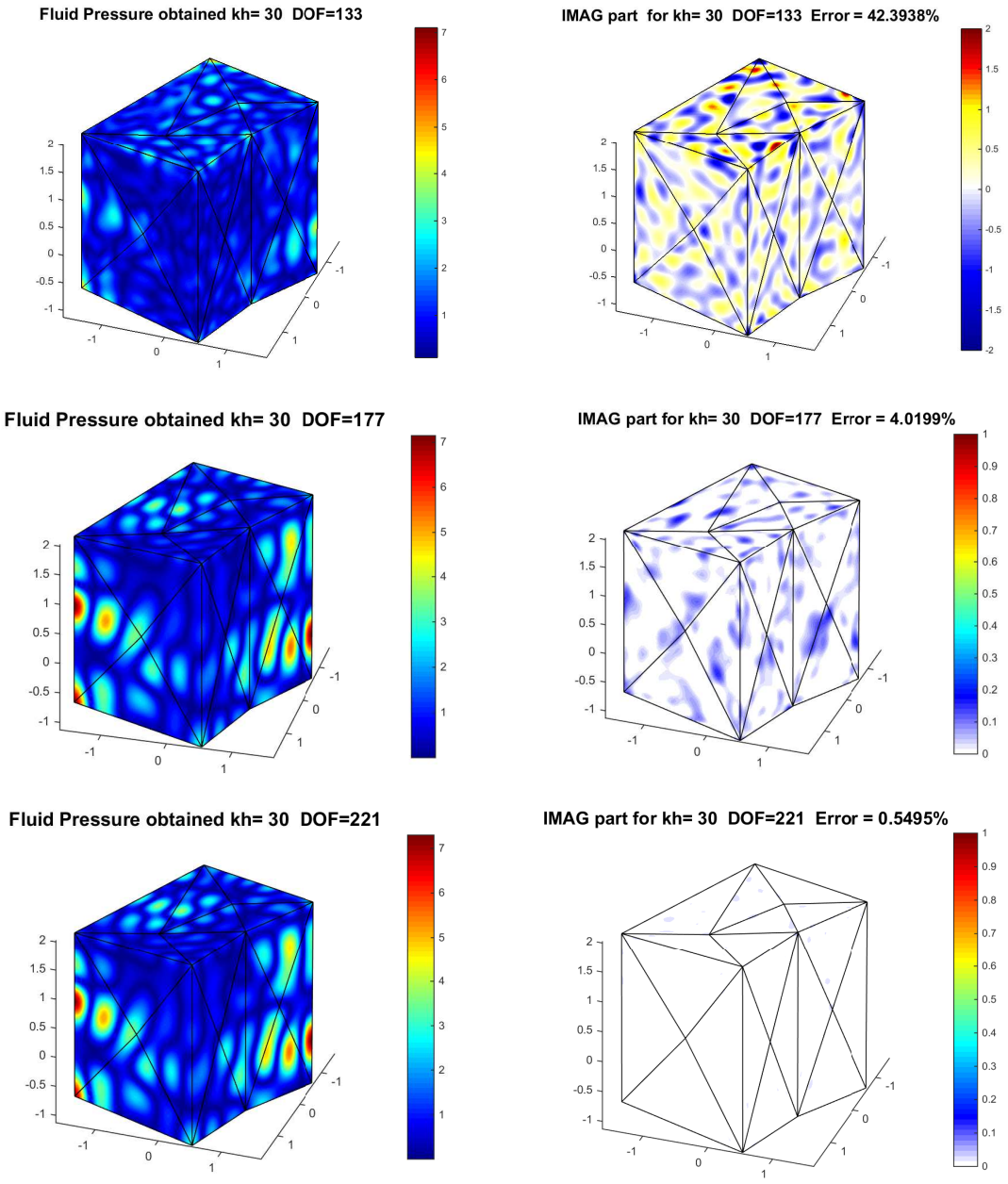

Fig. 5.2 Pressure response in the reverberant room due to a point source near the center of the room for $\kappa h_{max} = 30$, with $Z = Z_0 2\mathrm{i}$: PUFEM solution with $\bar{Q}$=133, $\varepsilon \approx 42.39\%$ (top), PUFEM solution with $\bar{Q}$=177, $\varepsilon \approx 4.02\%$ (middle), PUFEM solution with $\bar{Q}$=221, $\varepsilon \approx 0.55\%$ (bottom).

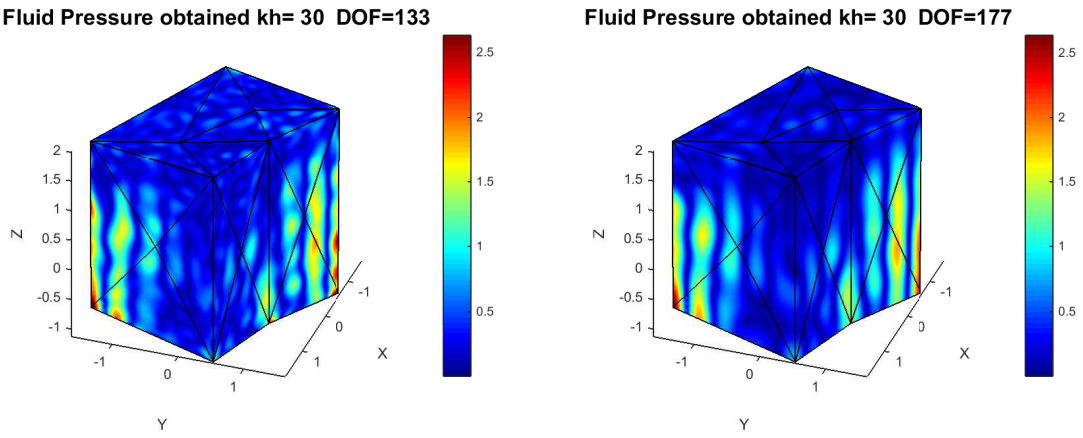

Fig. 5.3 Pressure response in the reverberant room due to a point source near the center of the room for $\kappa h_{max} = 30$, with $Z = Z_0(2 + 2i)$ prescribed on the roof, using $\bar{Q} = 133$ (left) and $\bar{Q} = 177$ (right).

5.2.2 Impact of the source position

In this section, we shall investigate the effect of the position of source point on the numerical error. It can be observed from Figure 5.4 that the point source is shifted from the room center to a position $\boldsymbol{x}_0 = (1.73, 0.54, 2.00)$ which is extremely close to one of the top corners of the reverberant room. To be more precise, the distance between the source and the top corner is set to be $d = 5.5 \times 10^{-3}$ m, which also corresponds to the non-dimensional parameter $\kappa d = 4.95 \times 10^{-2}$. The related sound pressure is shown in Figure 5.4 for three different PUFEM enrichments. If we compare the imaginary part with the previous case where the point source is located near the room center, we can easily find that, for the the same PUFEM parameters (say $\bar{Q} = 177$), the level of numerical error is much higher than the counterpart of the previous case.

In order to better illustrate this point of view, we plot two curves with respect to the relative errors in Figure 5.5. It can be clearly observed that the numerical errors are significantly influenced by the position of the source. More plane wave directions are required if we attempt to reach the same accuracy level when the source is placed near the corner of the reverberant room. This phenomenon probably stems from the amplified sound pressure due to the surrounding solid walls. Nevertheless, both curves demonstrate that the PUFEM results converge well.

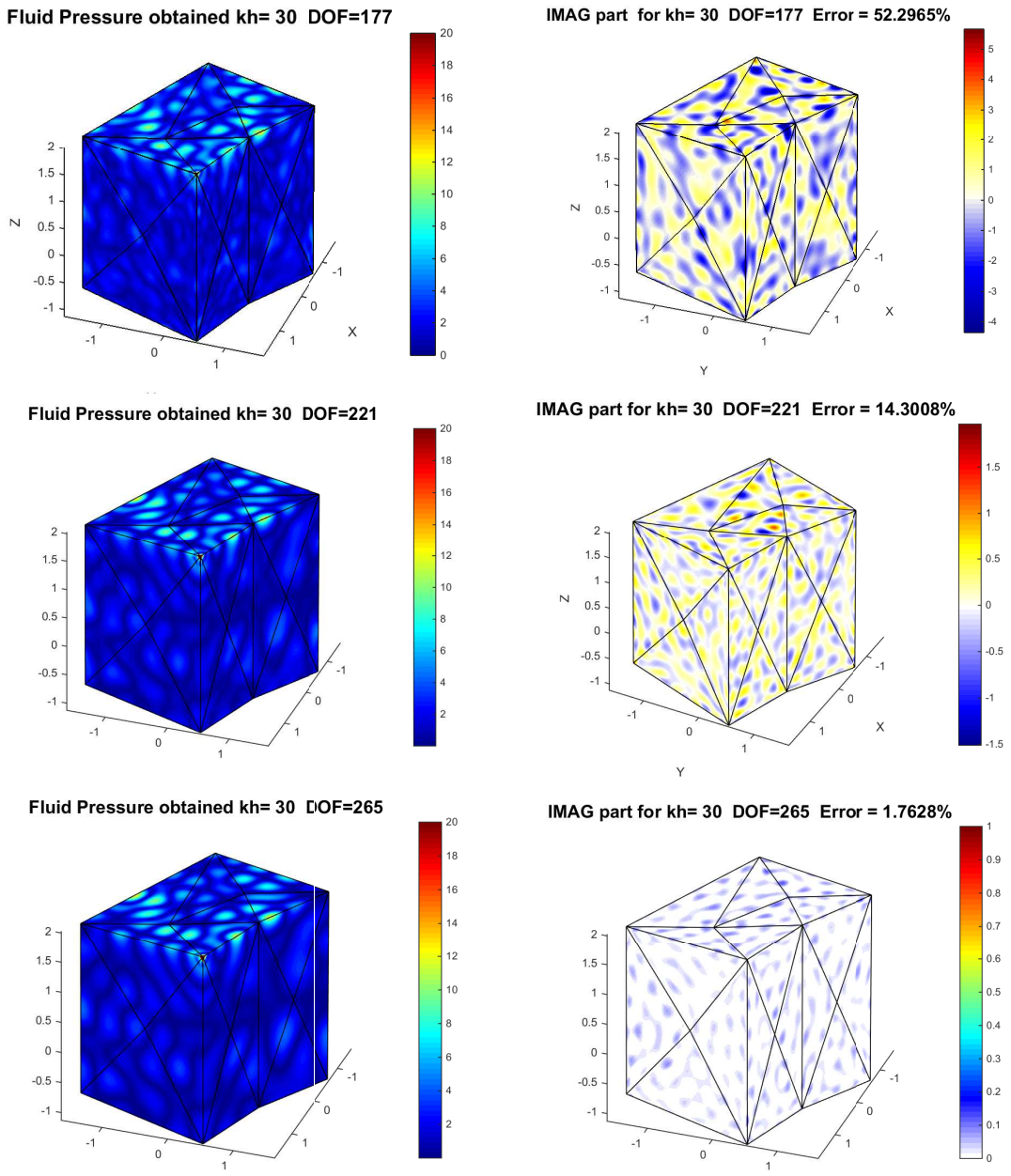

Fig. 5.4 Pressure response in the reverberant room due to a point source near the top corner of the room for $\kappa h_{max} = 30$: PUFEM solution with $\bar{Q}$=177, $\varepsilon \approx 52.30\%$ (top), PUFEM solution with $\bar{Q}$=221, $\varepsilon \approx 14.30\%$ (middle), PUFEM solution with $\bar{Q}$=265, $\varepsilon \approx 1.76\%$ (bottom).

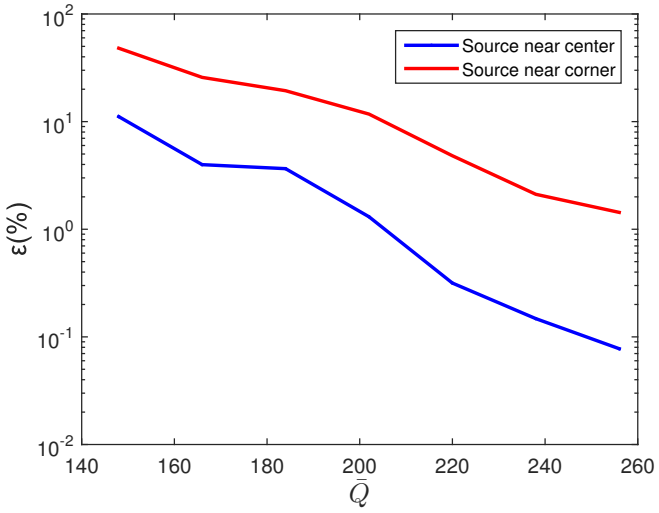

Fig. 5.5 Accuracy performance with regard to different positions of the point source: near the center (blue), near the corner (red).

5.2.3 Re-entrant corner

In this example, we shall consider a cavity problem in the presence of a re-entrant corner, where the sound field is produced by a monopole source placed inside the cavity. In Figure 5.6, it can be seen that a small cube of size 1m $\times$ 1m $\times$ 1m is cut out from the original cubic cavity of dimension 2m $\times$ 2m $\times$ 2m. Similar to the reverberant room case, we also apply a surface impedance boundary condition $Z = Z_0(2 + 2i)$ on the roof of the cavity. The characteristic length of this cavity is $h_{max} = 2$ m. The position of the point source $\boldsymbol{x}_0 = (0.99, 0.99, 1.01)$ is located very close to the re-entrant corner of the cavity, with the distance $d \approx 1.73 \times 10^{-2}$ m. Results (viewed from a given observing angle) are shown in Figure 5.7.

For the purpose of comparison, we investigate the accuracy performance with respect to three different cases where the monopole sources are respectively put near the normal corner (vertices of the cavity), re-entrant corner, and far from the corner. The curves plotted in Figure 5.8 reveal that the error can be affected by the location of the monopole source. The measured numerical error is relative larger when the monopole source is placed near a normal corner (vertex of the cavity) in comparison with the other two cases. This increased error probably stems from the amplified sound pressure which is caused by the surrounding solid walls. These curves also show that the numerical error is not sensitive to the re-entrant corner.

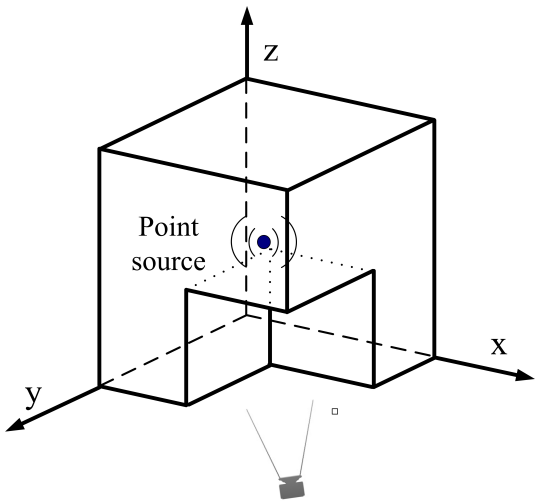

Fig. 5.6 The building model with re-entrant corner.

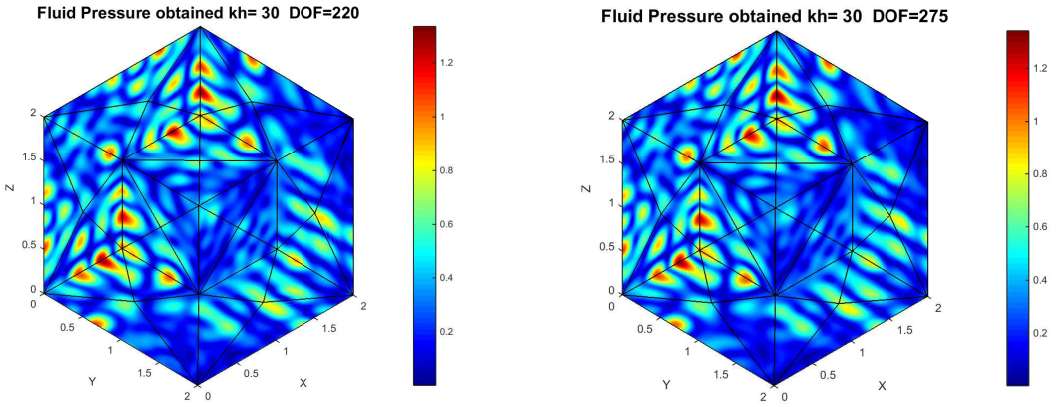

Fig. 5.7 Numerical solutions due to a point source near the re-entrant corner of the room with surface impedance $Z = Z_0(2 + 2\mathrm{i})$ applied on the roof for $\kappa h_{max} = 30$: using $\bar{Q} = 220$ (left), using $\bar{Q} = 275$ (right).

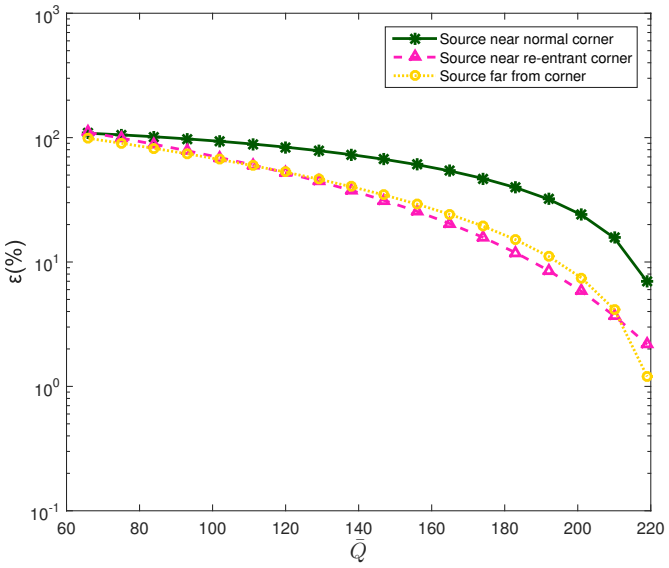

Fig. 5.8 Accuracy performance with regard to the location of the point source: near the center (blue), near the corner (red).

5.3 PUFEM with EHF

5.3.1 Formulation for the air and absorbing media

The general interior acoustic problem is sketched in Figure 5.9. It consists of two domains, $\Omega = \Omega_a \bigcup \Omega_p$, where Ω_a represents the air-filled cavity and Ω_p denotes the porous absorber. For the sake of clarity, all quantities associated with the air domain are denoted by the subscript a while the porous domain is referred by the subscript p. We consider that the porous media can be modeled as an equivalent homogeneous fluid so the governing equations

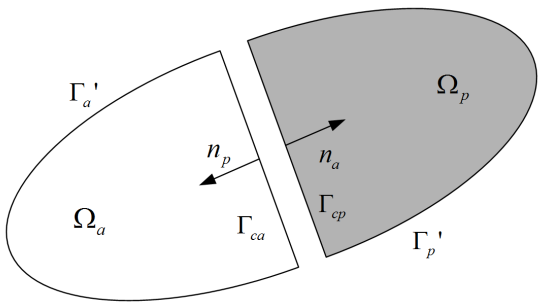

Fig. 5.9 General interior case and variables notation.

in each domain are given by the Helmholtz equation:

$$\Delta p_a + {\kappa_a}^2 p_a = 0 \qquad \text{in } \Omega_a, \tag{5.4}$$

$$\Delta p_p + {\kappa_p}^2 p_p = 0 \qquad \text{in } \Omega_p. \tag{5.5}$$

Recall that $\kappa_a = \omega/c_a$ stands for the wavenumber in the air domain as mentioned above,and $\kappa_p = \omega(\rho_p/K_p)^{1/2}$, where the quantities such as mean density and dynamic bulk modulus can be calculated through Johnson-Champoux Allard's model described in Appendix A. The coupling condition at the interface boundary Γ_{ca} and Γ_{cp} (see Figure 5.9) has to satisfy the continuity of pressure and normal velocity, which gives

$$p_p = p_a, \tag{5.6}$$

and

$$\frac{\phi}{\rho_p}\frac{\partial p_p}{\partial n_p} = -\frac{1}{\rho_a}\frac{\partial p_a}{\partial n_a}. \tag{5.7}$$

Here, n_p and n_a are the outward normals of porous and air domain with the convention that $n_p = -n_a$, ϕ is the porosity of the absorber. On the other part of the boundary of the air cavity Γ'_a, a prescribed normal velocity v_a is imposed:

$$\frac{\partial p_a}{\partial n_a} = \mathrm{i}\rho_a\omega v_a \qquad \text{in } \Gamma'_a, \tag{5.8}$$

whereas the porous absorber is assumed to be in contact with rigid walls, which reads

$$\frac{\partial p_p}{\partial n_p} = 0 \qquad \text{in } \Gamma'_p. \tag{5.9}$$

By following the steps of the work published in reference [80], we now introduce Λ, the Lagrange multiplier defined as the normal derivative of the acoustical pressure at the air-porous interface. The variational formulation for the air domain writes

$$\int_{\Omega_a}\left(\nabla p_a \cdot \nabla(\delta p_a) - \kappa_a^2 p_a \delta p_a\right)\mathrm{d}\Omega - \int_{\Gamma_{ca}} \delta p_a \Lambda \mathrm{d}\Gamma = \mathrm{i}\rho_a\omega \int_{\Gamma'_a} v_a \delta p_a \mathrm{d}\Gamma. \tag{5.10}$$

And similarly, for the porous domain, it writes

$$\frac{\phi\rho_a}{\rho_p}\int_{\Omega_p}\left(\nabla p_p \cdot \nabla(\delta p_p) - \kappa_p^2 p_p \delta p_p\right)\mathrm{d}\Omega + \int_{\Gamma_{cp}} \delta p_p \Lambda \mathrm{d}\Gamma = 0. \tag{5.11}$$

Applying standard Lagrange multiplier techniques, the continuity condition of pressure across the air-porous interface which is weakly enforced as

$$\int_{\Gamma_c} (p_p - p_a)\, \delta\Lambda \mathrm{d}\Gamma = 0, \tag{5.12}$$

where $\delta\Lambda$ stands for an appropriate weight function and Γ_c denotes the air-porous common interface. Similar to the strategy for the approximation of the potential p_a and p_p which is presented in equation (2.18), the Lagrange multiplier Λ is approximated by using real plane waves having the highest oscillations to make sure that the wave pattern at the interface is well captured. Hence, the Lagrange multiplier takes the form

$$\Lambda(\boldsymbol{x}) = \sum_{j=1}^{3} N_j \sum_{q=1}^{Q_j} \Lambda_{jq} \exp(\mathrm{iRe}(\kappa_p)\boldsymbol{d}_{jq} \cdot (\boldsymbol{x} - \boldsymbol{x}_j)), \tag{5.13}$$

where amplitudes Λ_{jq} are the unknown coefficients, N_j are the classical linear shape functions on triangular elements at the interface. Through the use of Galerkin method, we can finally obtain the coefficient matrices for the multiple subdomains problems. Note that the weight functions $\delta p_\alpha (\alpha = a, p)$ and $\delta\Lambda$ are selected from the plane wave basis indicated in equation (2.18). The above steps gives rise to the following symmetric system:

$$\begin{pmatrix} \mathbf{K}_a & 0 & -\mathbf{C}_a \\ 0 & \mathbf{K}_p & \mathbf{C}_p \\ -\mathbf{C}_a^T & -\mathbf{C}_p^T & 0 \end{pmatrix} \begin{pmatrix} \mathbf{A}_a \\ \mathbf{A}_p \\ \mathbf{\Lambda} \end{pmatrix} = \mathrm{i}\rho_a\omega \begin{pmatrix} \mathbf{V}_a \\ 0 \\ 0 \end{pmatrix}. \tag{5.14}$$

Here, $\mathbf{K}_\alpha$ $(\alpha = a, p)$ are the plane wave finite element matrices for the Helmholtz problem, $\mathbf{C}_\alpha$ denote the coupling matrices, vectors $\mathbf{A}_\alpha$ and $\mathbf{\Lambda}$ contain the plane wave amplitudes in formulas (2.18) and (5.13). It should be aware that the wavelength in the porous domain is usually much smaller than its counterpart in the acoustic domain, so the PUFEM element associated with the porous domain will span more wavelengths and lead to a higher computational cost. The 3D PUFEM element combined with exact integration scheme is used here to perform the analytical integrations of the PUFEM matrix coefficients.

5.3.2 3D standing wave tube test

This example is carried out to investigate the numerical performance of the PUFEM element for solving the acoustic transmission and coupling problem. Note that the absorbing materials are treated as an equivalent homogeneous fluid, and the corresponding acoustic properties of the sound absorbing porous material are taken from [40, 110] and reported in

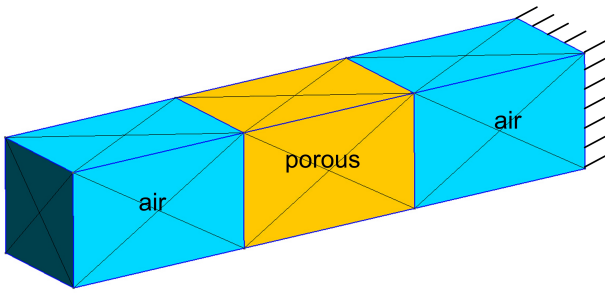

Fig. 5.10 The geometry and PUFEM mesh of the model.

Appendix A. In fact, the geometry and boundaries are similar to the 2D standing wave tube test introduced in Chapter 3. The additional dimension (width of the tube) is set to be 0.03 m, so the dimensions are 0.03 m $\times 0.03$m $\times 0.15$m. As shown in Figure 5.10, the whole length of the tube L is divided into three regions of equal length, and the porous absorber is placed in the middle region and represented in yellow. This numerical model is partitioned into 72 PUFEM element and contains 32 nodes in total. For this configuration, the characteristic length of the mesh which is still assigned to be the longest edge of the partitioning mesh, is $h_{max} = \sqrt{0.05^2 + 0.03^2 + 0.03^2} \approx 0.066$ m.

Recall that, in Chapter 3, we used an artificial value for the porous wavenumber. However, in the 3D standing wave tube test, the porous absorber is made of a realistic material A (acoustic properties of the materials used in this work are given in Appendix A). In this example, we apply the prescribed velocity boundary condition, $\frac{\partial p_a}{\partial n_a} = 1$, on the front surface of the tube, and the end of the tube is a rigid wall. Figure 5.11 and 5.12 exhibits both the analytical and numerical solutions for $\kappa_a h_{max} = 30$ (this corresponds to a frequency of about $21,000$ Hz). In this example, the numerical error is around 1% when the average plane wave directions per node $\bar{Q}$ is 305, and this corresponds to a total number of degrees of freedom $N_{dof} = 12784$ (including the Lagrange multipliers) and $n_\lambda = 2.25$ (this value is estimated by considering the wavelength in the air). From Figure 5.13, we may note that the solution in the "quiet zone" is typical of a stationary wave and the accuracy is excellent.

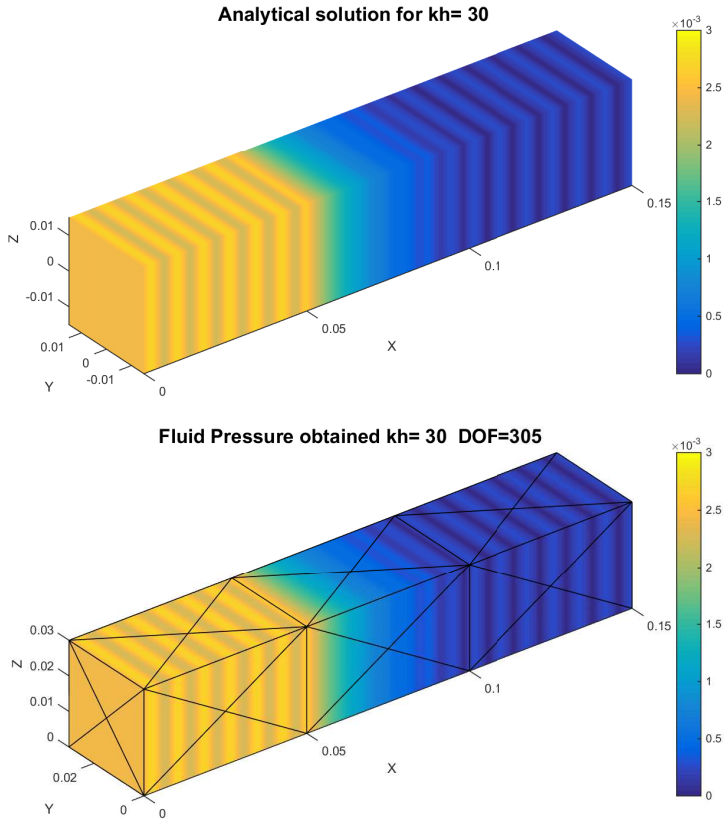

Fig. 5.11 Pressure response (absolute value) in the standing wave tube with material A (see Appendix A): analytical solution for $\kappa_a h_{max} = 30$ (top), PUFEM solution with $\bar{Q} = 305$ (bottom).

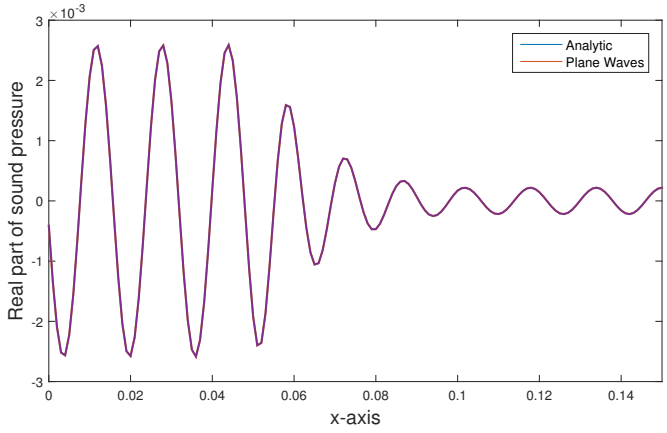

Fig. 5.12 Real part of the sound pressure field in the standing wave tube with material A, $\kappa_a h_{max} = 30$: analytical solution (blue curve) and PUFEM results (red curve).

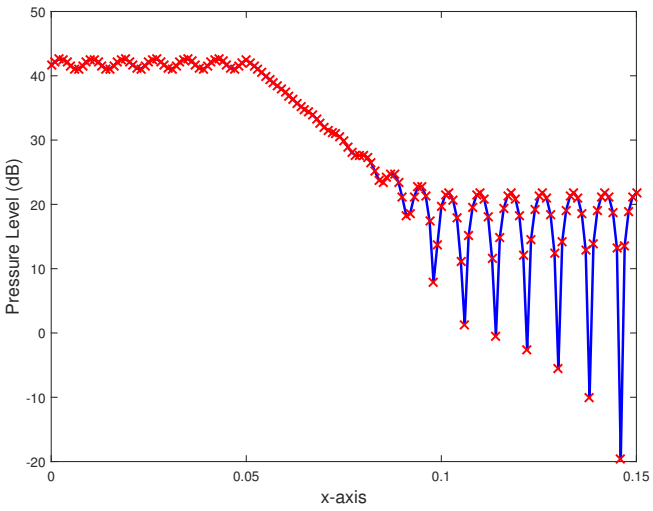

Fig. 5.13 The sound pressure field (in log scale) in the standing wave tube with material A, $\kappa h_{max} = 30$: analytical solution (blue curve) and PUFEM results (red cross symbol).

5.3.3 3D standing wave tube test with geometric singularity

This last example is carried out to illustrate the performance of the PUFEM element for tackling geometric singularities, the geometry and mesh of the standing wave tube with variable backing is shown in Figure 5.14, where 41 nodes and 101 PUFEM elements are included in this numerical model in total. In Figure 5.15, we display the sound pressure level in the tube for $\kappa_a h_{max} = 30$ and no material is present. It can be observed that the scattering of waves by the edge singularity generates a transverse mode in the tube. On the contrary, this mode can not be observed when a porous absorber is placed in the middle region of the tube, as shown in Figure 5.16. The adopted average number of plane waves per node $\bar{Q}$ in these two models (with and without porous material) are both equal to 308, giving the total number of dof, $N_{dof} = 15676$.

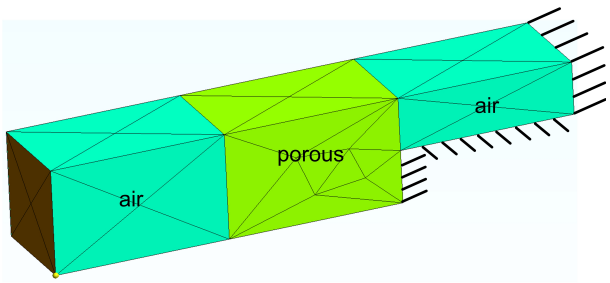

Fig. 5.14 The geometry and the PUFEM mesh of the model with geometric singularity.

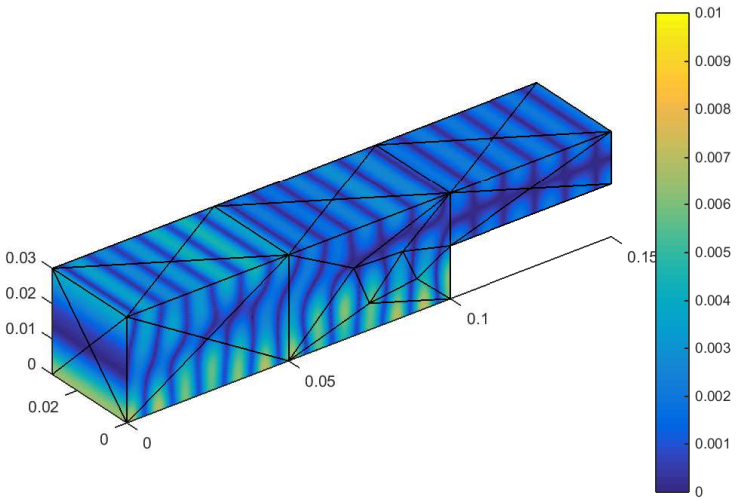

Fig. 5.15 Pressure response (absolute value) in the standing wave tube without porous material, for $\kappa_a h_{max} = 30$.

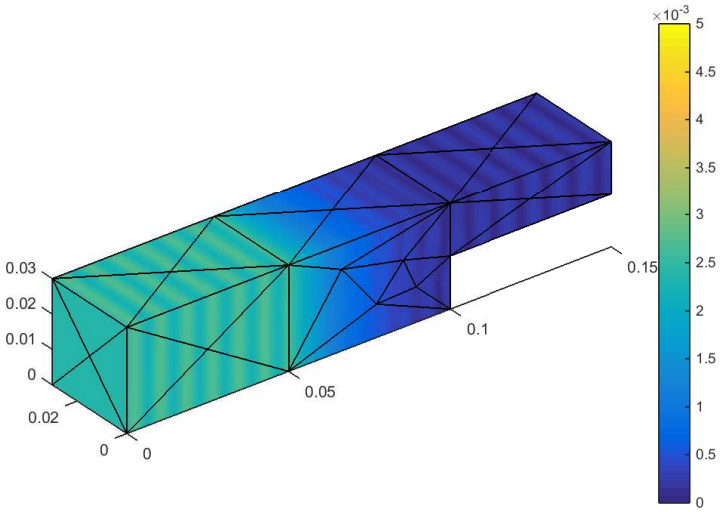

Fig. 5.16 Pressure response (absolute value) in the standing wave tube with material B (see Appendix A) placed in the middle region, for $\kappa_a h_{max} = 30$.

5.4 Concluding remarks

This chapter has investigated the numerical performances of the PUFEM for solving 3D interior sound fields and wave transmission problems in which absorbing materials are present. In the specific case of a locally reacting material modeled by a surface impedance, the numerical error can be easily estimated via equation (5.3) by simply considering a purely imaginary impedance which is known to produce real-valued solutions. Based on this error estimate, it has been shown that the PUFEM can provide accurate solutions at a relatively low computational cost, and around 2 degrees of freedom per wavelength are found to be sufficient. In the last section of the chapter, we extended the PUFEM for solving wave transmission problems between the air and a porous material modeled as an equivalent homogeneous fluid. A simple 1D problem was tested (standing wave tube) and the PUFEM solutions were found to be around 1% error which is sufficient for engineering purposes.

Chapter 6

Conclusion and perspectives

In this work, we have introduced the underlying concept of PUFEM and the basic formulation related to the Helmholtz equation in a bounded domain. The plane wave enrichment process of PUFEM variables was shown and explained in detail. The main idea is to include *a priori* knowledge about the local behavior of the solution into the finite element space by using a set of wave functions that are solutions to the partial differential equations. In this study, the use of plane waves propagating in various directions was favored as it leads to efficient computing algorithms. In addition, we showed that the number of plane wave directions depends on the size of the PUFEM element and the wave frequency both in 2D and 3D. The selection approaches for these plane waves were also illustrated. For 3D problems, we have investigated two distribution schemes of plane wave directions which are the discretized cube method and the Coulomb force method. It has been shown that the latter allows to get uniformly spaced wave directions and enables us to acquire an arbitrary number of plane waves attached to each node of the PUFEM element, making the method more flexible.

In Chapter 3, we investigated the numerical simulation of propagating waves in two dimensions using PUFEM. The main priority of this chapter is to come up with an Exact Integration Scheme (EIS), resulting in a fast integration algorithm for computing system coefficient matrices with high accuracy. The 2D PUFEM element was then employed to solve an acoustic transmission problem involving porous materials. Results have been verified and validated through the comparison with analytical solutions. Comparisons between the Exact Integration Scheme (EIS) and Gaussian quadrature showed the substantial gain offered by the EIS in terms of CPU time.

A 3D Exact Integration Scheme was presented in Chapter 4, in order to accelerate and compute accurately (up to machine precision) of highly oscillatory integrals arising from the

PUFEM matrix coefficients associated with the 3D Helmholtz equation. Through convergence tests, a criteria for selecting the number of plane waves was proposed. It was shown that this number only grows quadratically with the frequency thus giving rise to a drastic reduction in the total number of degrees of freedoms in comparison to classical FEM. The method has been verified for two numerical examples. In both cases, the method is shown to converge to the exact solution. For the cavity problem with a monopole source located inside, we tested two numerical models to assess their relative performance. In this scenario where the exact solution is singular, the number of wave directions has to be chosen sufficiently high to ensure that results have converged. The numerical model which consists in separating the total pressure p into a singular incident field p_i and a more regular scattered field p_{sc} allows us to circumvent this limiting factor. In the last part of this chapter, enrichment strategies based on the criteria (4.66) have been proposed.

In the last Chapter, we have investigated the numerical performances of the PUFEM for solving 3D interior sound fields and wave transmission problems in which absorbing materials are present. For the specific case of a locally reacting material modeled by a surface impedance, a numerical error estimation criteria is proposed by simply considering a purely imaginary impedance which is known to produce real-valued solutions. Based on this error estimate, it has been shown that the PUFEM can achieve accurate solutions while maintaining a very low computational cost, and only around 2 degrees of freedom per wavelength were found to be sufficient. We also extended the PUFEM for solving wave transmission problems between the air and a porous material modeled as an equivalent homogeneous fluid. A simple 1D problem was tested (standing wave tube) and the PUFEM solutions were found to be around 1% error which is sufficient for engineering purposes.

To the best knowledge of the author, the development and application of PUFEM for solving three-dimensional acoustical problems have been the subject of rather limited research work. Some potential developments of 3D PUFEM could be carried out in any of the following 3 relevant aspects: the selection of wave basis, the speed up process for integration and the hybrid approaches. Some suggestions and perspectives concerning future research topics are given herein:

1. As we have introduced in Chapter 2, some other wave functions could be adopted to enrich the finite element space. They could take precedence over the performance of plane wave basis under some certain circumstances. Although some of them might have been studied in other wave-based methods, there still exists great potential of their applications in the context of PUFEM, especially in 3D. For the plane wave basis,

the distribution of plane wave directions could be further extended by introducing an external charge in order to cluster the wave directions towards a desired orientation. This kind of effort could give rise to a higher convergence rate of the method as well as a reduction of the computational load.

2. For the 3D Exact Integration Scheme, some other approaches could be used to avoid redundant edges integral evaluation, we can first compute all the unique and then to recombine them. However this approach requires the storage of a large number of values and may lead to the issue of memory consuming. Another way of improvement can be obtained is by using tensorization. For instance if elements are similar (in the volume core) the same plane wave can be used and most of elementary computation can be performed only once. The development of PUFEM curved element should also be investigated.

3. To increase the applicability of PUFEM method to tackle realistic configurations, the development towards the hybrid approaches (e.g. FEM and PUFEM combined together) represents an interesting direction. This hybrid framework takes benefits from the best properties of two numerical approaches, which allows us to alleviate the restrictions of geometrical complexity of the problem while maintaining the high efficiency for solving large domain or high frequency problems.

References

[1] A. Moiola, R. Hiptmair, I. P. (2011). Plane wave approximation of homogeneous helmholtz solutions. *Zeitschrift fur Angewandte Mathematik und Physik*, 62:809–837.

[2] Allard, J. F. and Atalla, N. (2009). *Propagation of Sound in Porous Media: Modelling Sound Absorbing Materials*. JJohn Wiley and Sons, New Jersey.

[3] Anderson, S. J. (2013). Optimizing hf radar siting for surveillance and remote sensing in the strait of malacca. *Geoscience and Remote Sensing, IEEE Transactions on*, 51(3):1805–1816.

[4] Atalla, N., Hamdi, M. A., and Panneton, R. (2001). Enhanced weak integral formulation for the mixed (u,p) poroelastic equations. *J. Acoust. Soc. Am.*, 109:3065–3068.

[5] Atalla, N., Panneton, R., and Debergue, P. (1998). A mixed displacement-pressure formulation for poroelastic materials. *J. Acoust. Soc. Am.*, 104:1444–1452.

[6] Attenborough, K. (2006). Acoustic characteristics of rigid fibrous absorbents and granular materials. *J. Acoust. Soc. Am.*, 73:785–799.

[7] Babuška, I. and Guo, B. Q. (1992). The h, p and h-p version of the finite element method: basis theory and applications. *Advances in Engineering Software*, 15(3-4):159–174.

[8] Babuška, I., Ihlenburg, F., Paik, E. T., and Sauter, S. A. (1995). A generalized finite element method for solving the helmholtz equation in two dimensions with minimal pollution. *Comput. Methods Appl. Mech. Engrg.*, 128:325–359.

[9] Babuška, I. and Melenk, J. M. (1997). The partition of unity method. *Int. J. Numer. Meth. Engng.*, 40:727–758.

[10] Babuška, I. and Sauter, S. A. (2000). Is the pollution effect of the fem avoidable for the helmholtz equation considering high wave numbers? *SIAM Journal on Numerical Analysis*, 34:2392–2423.

[11] Barrick, D. E., Evans, M. W., and Weber, B. L. (1977). Ocean surface currents mapped by radar. *Science*, 198(4313):138–144.

[12] Bayliss, A., Goldstein, C. I., and Turkel, E. (1985). On accuracy conditions for t he numerical computation of waves. *J. Comput. Phys.*, 59:396–404.

[13] Bayliss, A., Gunzburger, M., and Turkel, E. (1982). Boundary conditions for the numerical solution of elliptic equations in exterior regions. *SIAM Journal on Applied Mathematics*, 42:430–451.

[14] Berenger, J. P. (1994). A perfectly matched layer for the absorption of electro-magnetic waves. *J. Comput. Phys.*, 114:185–200.

[15] Bergen, B., Genechten, B. V., Vandepitte, D., and Desmet, W. (2010). An efficient trefftz-based method for three-dimensional helmholtz problems in unbounded domains. *Comput. Model. Engrg. Sci.*, 61:155–175.

[16] Bettess, P. (1992). *Infinite Elements*. Penshaw Press, U.K.

[17] Bettess, P., Shirron, J., Laghrouche, O., Peseux, B., Sugimoto, R., and Tevelyan, J. (2003). A numerical integration scheme for special finite elements for the helmholtz equation. *Int. J. Numer. Meth. Engng.*, 56:531 – 552.

[18] Billingham, J. and King, A. C. (2001). *Wave motion*. Cambridge University Press, 1st Edition, Cambridge.

[19] Biot, M. A. (1956). Theory of propagation of elastic waves in a fluid-saturated porous solid. *J. Acoust. Soc. Am.*, 28(2):168–191.

[20] Blackstock, D. T. (2000). *Fundamentals of physical acoustics*. Wiley-Interscience Publication, New York.

[21] Bouillard, P. and Ihlenburg, F. (1999). Error estimation and adaptivity for the finite element method in acoustics: 2d and 3d applications. *Computer Methods in Applied Mechanics and Engineering*, 176:147–163.

[22] Brebbia, C. A., Telles, J. C. F., and Wrobel, L. C. L. (1984). *Boundary Element Techniques: Theory and Applications in Engineering*. Springer-Verlag, New York.

[23] Cessenat, O. (1996). *Application d'une nouvelle formulation variationnelle aux équations d'ondes harmoniques. Problèmes de Helmholtz 2D et de Maxwell 3D*. PhD thesis, Université Paris IX Dauphine.

[24] Cessenat, O. and Després, B. (1998). Application of an ultra weak variational formulation of elliptic pdes to the two-dimensional helmholtz equation. *J. Numer. Anal.*, 35(1):255–299.

[25] Champoux, Y. and Stinson, M. R. (1992). On acoustical models for sound propagation in rigid frame porous materials and the influence of shape factors. *J. Acoust. Soc. Am.*, 92(2):1120–1131.

[26] Chandler-Wilde, S. and Langdon, S. (2007). A galerkin boundary element method for high frequency scattering by convex polygons. *SIAM Journal on Numerical Analysis*, 45(2):610–640.

[27] Chazot, J. D., Nennig, B., and Perrey-Debain, E. (2013). Performances of the partition of unity finite element method for the analysis of two-dimensional interior sound fields with absorbing materials. *J. Sound. Vib.*, 332:1930 – 1946.

[28] Chazot, J. D. and Perrey-Debain, E. (2014). The partition of unity finite element method for the simulation of waves in air and poroelastic media. *J. Acoust. Soc. Am.*, 135(2):724–733.

[29] Chen, K., Cheng, J., and Harris, P. J. (2009). A new study of the burton and miller method for the solution of a 3d helmholtz problem. *IMA journal of applied mathematics*, 74(2):163–177.

[30] Ciskowski, R. D. and Brebbia, C. A. (1991). *Boundary element methods in acoustics*. Computa-tional Mechanics Publications Southampton, Boston.

[31] Colton, D. and Kress, R. (1992). *Inverse Acoustic and Electromagnetic Scattering Theory*. Springer Verlag, New York.

[32] Copley, L. G. (1967). Integral equation method for radiation from vibrating bodies. *J. Acoust. Soc. Am.*, 41:807–810.

[33] Craggs, A. (1972). The use of simple three-dimensional acoustic finite elements for determining the natural modes and frequencies of complex shaped enclosures. *J. Sound. Vib.*, 23(3):331–339.

[34] Cutnell, J. D. and Johnson, K. W. (1994). *Physics, 3rd Edition, Hoboken*. John Wiley and Sons, New Jersey.

[35] Deckers, E., Bergen, B., Genechten, B. V., Vandepitte, D., and Desmet, W. (2012a). Is the pollution effect of the fem avoidable for the helmholtz equation considering high wave numbers? *Comput. Methods Appl. Mech. Engrg.*, 241–244:286–301.

[36] Deckers, E., Genechten, B. V., Vandepitte, D., and Desmet, W. (2011). Efficient treatment of stress singularities in poroelastic wave based models using special purpose enrichment functions. *Comput. Struct.*, 89:1117–1130.

[37] Deckers, E., Hörlin, N. E., Vandepitte, D., and Desmet, W. (2012b). A wave based method for the efficient solution of the 2d poroelastic biot equations. *Comput. Methods Appl. Mech. Eng.*, 201–204:245–262.

[38] Deraemaeker, A., Babuška, I., and Bouillard, P. (1999). Dipersion and pollution of the fem solution for the helmholtz equation in one, two and three dimensions. *Int. J. Numer. Meth. Engng.*, 46:471–499.

[39] Desmet, W. (1998). *A wave based prediction technique for coupled vibro-acoustic analysis*. PhD thesis, Katholieke Universiteit Leuven.

[40] Doutres, O., Dauchez, N., Genevaux, J. M., and Dazel, O. (2007). Validity of the limp model for porous materials: a criterion based on the biot theory. *J. Acoust. Soc. Am.*, 122:2038–2048.

[41] Erber, T. and Hockney, G. M. (1991). Equilibrium configurations of n equal charges on a sphere. *J Phys A: Math Gen*, 24(23):1369 – 1377.

[42] Evans, G. A. and Webster, J. R. (1999). A comparison of some methods for the evaluation of highly oscillatory integrals. *J. Comput. Appl. Math.*, 112:55–69.

[43] Gabard, G. (2009). Exact integration of polynomial exponential products with application to wave-based numerical methods. *Commun. Numer. Meth. Eng.*, 25(3):237–246.

[44] Gabard, G. and Dazel, O. (2015). A discontinuous galerkin method with plane waves for sound-absorbing materials. *Int. J. Numer. Meth. Engng.*, 104(12):1115–1138. nme.4961.

[45] Gabard, G., Gamallo, P., and Huttunen, T. (2011). A comparison of wavebased discontinuous galerkin, ultra-weak and least-square methods for wave problems. *Int. J. Numer. Meth. Engng*, 85:380–402.

[46] Gamallo, P. and Astley, R. (2007). A comparison of two trefftz-type methods: The ultra-weak variational formulation and the least squares method for solving shortwave 2d helmholtz problems. *Int. J. Numer. Meth. Engng.*, 71:406–432.

[47] Gamallo, P. and Astley, R. J. (2006). The partition of unity finite element method for short wave acoustic propagation on non-uniform potential flows. *Int. J. Numer. Meth. Engng.*, 65:425–444.

[48] Genechten, B. V., Vandepitte, D., and Desmet, W. (2010a). A trefftz-based numerical modelling framework for helmholtz problems with complex multiple scatterer configurations. *J. Comput. Phys.*, 229:6623–6643.

[49] Genechten, B. V., Vandepitte, D., and Desmet, W. (2011). A direct hybrid finite element – wave based modelling technique for efficient coupled vibro-acoustic analysis. *Comput. Methods Appl. Mech. Engrg.*, 200:742–764.

[50] Genechten, B. V., Vergote, K., Vandepitte, D., and Desmet, W. (2010b). A multi-level wave based numerical modelling framework for the steady-state dynamic analysis of bounded helmholtz problems with multiple inclusions. *Comput. Methods Appl. Mech. Engrg.*, 199:1881–1905.

[51] Givoli, D. (1991). Non–reflecting boundary conditions: A review. *J. Comput. Phys.*, 94:1–29.

[52] Gladwell, G. M. L. (1966). A variational formulation of damped acousto-structural vibration problems. *J. Sound. Vib.*, 4:172–186.

[53] Glasser, L. and Every, A. G. (1992). Energies and spacings of point charges on a sphere. *J Phys A: Math Gen*, 25(9):2473 –2482.

[54] Gordon, W. B. (1975). Far-field approximation to the kirchhoff-helmholtz representations of scattered fields. *IEEE T. Antenn. Propag.*, pages 590–5920.

[55] Hagstrom, T. (1999). Radiation boundary conditions for the numerical simulation of waves. *Acta. Numerica.*, 8:47–106.

[56] Hagstrom, T., Mar-Or, A., and Givoli, D. (2008). High-order local absorbing conditions for the wave equation: Extensions and improvements. *J. Comput. Phys.*, 227(6):3322–3357.

[57] Hal, B. V., Desmet, W., and Vandepitte, D. (2003). A coupled finite element–wave based approach for the steady-state dynamic analysis of acoustic systems. *J. Comput. Acoust.*, 11:285–303.

[58] Ham, S. and Bathe, K. J. (2012). A finite element method enriched for wave propagation problems. *Comput. Struct.*, 94–95:1–12.

[59] Harris, J. G. (2001). *Linear elastic waves*. Cambridge University Press, Cambridge.

[60] Hopkins, C. (1989). *Sound Insulation*. Elsevier, Butterworth-Heinemann.

[61] Howarth, C. J. (2014). *New Generation Finite Element Methods For Forward Seismic Modelling*. PhD thesis, University of Reading.

[62] Huang, Z. Y. and Jiang, W. K. (2007). An effective method calculating acoustic green's function for closed rectangular cavity using the ewald's summation technique. *Acta. Acust. united. Ac.*, 93(5):853–856.

[63] Hubert, J. S. and Palencia, E. S. (1989). *Vibration and Coupling of Continuous Systems: Asymptotic Methods*. Springer, Berlin Heidelberg.

[64] Huttunen, T., Gammallo, P., and Astley, R. (2009). A comparison of two wave element methods for the helmholtz problem. *Commun. Numer. Meth. Eng.*, 25:35–52.

[65] Huttunen, T., Kaipio, J. P., and Monk, P. (2004). The perfectly matched layer for the ultra weak variational formulation of the 3d helmholtz equation. *Int. J. Numer. Meth. Engng*, 61:1072–1092.

[66] Huttunen, T., Malinen, M., and Monk, P. (2007). Solving maxwell's equations using the ultra weak variational formulation. *J. Comput. Phys.*, 223:731–758.

[67] Huttunen, T. and Monk, P. (2007). The use of plane waves to approximate wave propagation in anisotropic media. *J. Comput. Math.*, 25:1072–1092.

[68] Huttunen, T., Monk, P., and Kaipio, J. P. (2002). Computational aspects of the ultra-weak variational formulation. *J. Comput. Phys.*, 182:27–46.

[69] Ihlenburg, F. and Babuška, I. (1995). Dispersion analysis and error estimation of galerkin finite element methods for the helmholtz equation. *Int. J. Numer. Meth. Engng*, 38(22):3745–3774.

[70] Jonckheere, S., Deckers, E., Genechten, B. V., Vandepitte, D., and Desmet, W. (2013). A direct hybrid finite element – wave based method for the steady-state analysis of acoustic cavities with poro-elastic damping layers using the coupled helmholtz–biot equations. *Comput. Methods Appl. Mech. Engrg.*, 263:144–157.

[71] Kacimi, A. E. and Laghrouche, O. (2009). Numerical modelling of elastic wave scattering in frequency domain by the partition of unity finite element method. *Int. J. Numer. Meth. Engng.*, 77(12):1646–1669.

[72] Kacimi, A. E. and Laghrouche, O. (2010a). Improvement of pufem for the numerical solution of high-frequency elastic wave scattering on unstructured triangular mesh grids. *Int. J. Numer. Meth. Engng.*, 84(3):330–350.

[73] Kacimi, A. E. and Laghrouche, O. (2010b). Numerical analysis of two plane wave finite element schemes based on the partition of unity method for elastic wave scattering. *Comput. Struct.*, 88:1492–1497.

[74] Krommer, A. and Ueberhuber, C. (1998). *Computational Integration*. SIAM, Philadelphia.

[75] Ladevèze, P. (1996). A new computational approach for structure vibrations in the medium frequency range. *CR Acad Sci Paris*, 332(2b):849–856.

[76] Ladevèze, P., Arnaud, L., Rouch, P., and Blanzé, C. (2003). A multiscale computational method for medium-frequency vibrations of assemblies of heterogeneous plates. *Comput. Struct.*, 81:1267–1276.

[77] Laghrouche, O. and Bettess, P. (2000). Short wave modelling using special finite elements. *J. Comput. Acoust.*, 8(1):189–210.

[78] Laghrouche, O., Bettess, P., and Astley, R. J. (2002). Modelling of short wave diffraction problems using approximating systems of plane waves. *Int. J. Numer. Meth. Engng*, 54(10):1501–1533.

[79] Laghrouche, O., Bettess, P., Perrey-Debain, E., and Trevelyan, J. (2003). Plane wave basis for wave scattering in three dimensions. *Commun. Numer. Meth. Eng.*, 19(9):715–723.

[80] Laghrouche, O., Bettess, P., Perrey-Debain, E., and Trevelyan, J. (2005). Wave interpolation finite elements for helmholtz problems with jumps in the wave speed. *Comput. Method. Appl. M.*, 194(2-3):367–381.

[81] Laghrouche, O. and Mohamed, M. S. (2010). Locally enriched finite elements for the helmholtz equation in two dimensions. *Comput. Struct.*, 88:1469–1473.

[82] Lanoye, R., Vermeir, G., Lauriks, W., Sgard, F., and Desmet, W. (2008). Prediction of the sound field above a patchwork of absorbing materials. *J. Acoust. Soc. Am.*, 123:793–802.

[83] Li, S. and Huang, Q. (2010). An improved form of the hypersingular boundary integral equation for exterior acoustic problems. *Eng. Anal. Boundary Elem.*, 34(3):189–195.

[84] Lightman, A. P. (2000). *Great ideas in physics: the conservation of energy, the second law of thermodynamics, the theory of relativity, quantum mechanics*. McGraw-Hill, New York.

[85] Makarov, S. N. and Ochmann2, M. (1998). An iterative solver of the helmholtz integral equation for high-frequency acoustic scattering. *J. Acoust. Soc. Am.*, 103(2):742–750.

[86] Mayer, P. and Mandel, J. (1997). The finite ray element method for the helmholtz equation of scattering: first numerical experiments. *UCD=CCM Report*, 111.

[87] Mechel, F. (1989). *Schallabsorber Bd.1. ÄußereSchallfelder– Wechselwirkungen*. S.HirzelVerlag, Stuttgart.

[88] Melenk, J. M. (1995). *On generalized finite element methods*. PhD thesis, University of Maryland.

[89] Melenk, J. M. (2002). *hp-Finite Element Methods for Singular Perturbations*. Springer, Berlin Heidelberg.

[90] Melenk, J. M. and Babuška, I. (1996). The partition of unity finite element method: Basic theory and applications. *Comput. Methods Appl. Mech. Engrg.*, 139:289–314.

[91] Mertens, T., Gamallo, P., and Astley, R. J. (2008). A mapped finite and infinite partition of unity method for convected acoustic radiation in axisymmetric domains. *Int. J. Numer. Meth. Engng.*, 197:4273–4283.

[92] Meyer, W. L., Bell, W. A., and Zinn, B. T. (1978). Boundary integral solutions of three dimensional acoustic radiation problems. *J. Sound. Vib.*, 59(2):807–810.

[93] Mohamed, M. S., Laghrouche, O., and Kacimi, A. E. (2010). Some numerical aspects of the pufem for efficient solution of 2d helmholtz problems. *Comput. Struct.*, 88:1484–1491.

[94] Monk, P., Schoberl, J., and Sinwe, A. (2010). Hybridizing raviartthomas elements for the helmholtz equation. *Electromagnetics*, 30:149–176.

[95] Morris, J. R., Deaven, D. M., and Ho, K. M. (1996). Energies and spacings of point charges on a sphere. *Phys Rev B: Condens Matter Mater Phys*, 53(4):1740 – 1743.

[96] Morse, P. M. and Feshbach, H. (1953). *Methods of theoretical physic*. McGraw-Hill, New York.

[97] Mousavi, S. E. and Sukumar, N. (2009). Generalized duffy transformation for integrating vertex singularities. *Computational Mechanics*, 45(2):127–140.

[98] Nédélec, J. C. (2001). *Acoustic and electromagnetic equations: integral representations for harmonic problems*. Springer Ver, New York.

[99] Nefske, D. J., Wolf, J. A., and Howell, L. J. (1982). Structural-acoustic finite element analysis of the automobile passenger compartment: A review of current practice. *J. Sound. Vib.*, 80(2):247–266.

[100] Nennig, B., Perrey-Debain, E., and Chazot, J. D. (2011). The method of fundamental solutions for acoustic wave scattering by a single and a periodic array of poroelastic scatterers. *Eng. Anal. Boundary Elem.*, 35:1019–1028.

[101] Ortiz, P. and Sanchez, E. (2001). An improved partition of unity finite element model for diffraction problems. *Int. J. Numer. Meth. Engng.*, 50:2727–2740.

[102] Panneton, R. and Atalla, N. (1997). An efficient finite element scheme for solving the three-dimensional poroelasticity problem in acoustics. *J. Acoust. Soc. Am.*, 101:3287–3298.

[103] Peake, M. J., Trevelyan, J., and Coates, G. (2014). The equal spacing of n points on a sphere with application to partition-of-unity wave diffraction problems. *Eng. Anal. Bound. Elem.*, 40:114–122.

[104] Perrey-Debain, E. (2006). Plane wave decomposition in the unit disc: convergence estimates and computational aspects. *J. Comput. Appl. Math.*, 193:140–156.

[105] Perrey-Debain, E., Laghrouche, O., Bettess, P., and Trevelyan, J. (2004). Plane wave basis finite elements and boundary elements for three dimensional wave scattering. *Philos. T. Roy. Soc. A.*, 362(1816):561–577.

[106] Petyt, M., Lea, J., and Koopmann, G. H. (1976). A finite element method for determining the acoustic modes of irregular shaped cavities. *J. Sound. Vib.*, 45(4):495–502.

[107] Pluymers, B., Desmet, W., Vandepitte, D., and Sas, P. (2004). Application of an efficient wave based prediction technique for the analysis of vibro-acoustic radiation problems. *J. Comput. Appl. Math.*, 168:353–364.

[108] Pluymers, B., Desmet, W., Vandepitte, D., and Sas, P. (2005). On the use of a wave based prediction technique for steady-state structural-acoustic radiation analysis. *J. Comput. Model. Engrg. Sci*, 7:173–184.

[109] Rayleigh, J. W. S. (1945). *The theory of sound*. Dover Publications, New York.

[110] Rigobert, S., Atalla, N., and Sgard, F. C. (2003). Investigation of the convergence of the mixed displacement pressure formulation for three-dimensional por oelastic materials using hierarchical elements. *J. Acoust. Soc. Am.*, 114:2607–2617.

[111] Riou, H., Ladevèze, P., and Rouch, P. (2004). Extension of the variational theory of complex rays to shells for medium-frequency vibrations. *J. Sound. Vib.*, 272(1–2):341–360.

[112] Riou, H., Ladevèze, P., and Sourcis, B. (2008). The multiscale vtcr approach applied to acoustics problems. *J. Comput. Acoust.*, 16(4):487–505.

[113] Rouch, P. and Ladevèze, P. (2003). The variational theory of complex rays: a predictive tool for medium-frequency vibrations. *Comput. Methods Appl. Mech. Engrg.*, 192(28–30):3301–3315.

[114] Saff, E. B. and Kuijlaars, A. B. J. (1997). Distributing many points on a sphere. *Math. Intell.*, 19(1):5 – 11.

[115] Sommerfeld, A. (1912). Die greensche funktion der schwingungsgleichung. *Jahresber. Deutsch. Math.*, 21(1):309–353.

[116] Sugimoto, R., Bettess, P., and Tevelyan, J. (2003). A numerical integration scheme for special quadrilateral finite elements for the helmholtz equation. *Commun. Numer. Meth. Eng.*, 19:233 – 245.

[117] Sugimoto, R., Bettess, P., and Trevelyan, J. (2002). A numerical integration scheme for special quadrilateral finite elements for helmholtz equation. *Commun. Numer. Meth. Eng.*, 19:233–245.

[118] Terai, T. (1980). On calculation of sound fields around three dimensional objects by integral equation methods. *J. Sound. Vib.*, 69(1):71–100.

[119] Thompson, L. L. (2006). A review of finite element methods for time-harmonic acoustics. *J. Acoust. Soc. Am.*, 119:1315–1330.

[120] Tsynkov, S. V. (1998). Numerical solution of problems on unbounded domains, a review. *Applied Numerical Mathematics*, 27:465–532.

[121] Vanmaele, C., Vandepitte, D., and Desmet, W. (2007). An efficient wave based prediction technique for plate bending vibrations. *Comput. Methods Appl. Mech. Engrg.*, 196:3178–3189.

[122] Vanmaele, C., Vandepitte, D., and Desmet, W. (2009). An efficient wave based prediction technique for dynamic plate bending problems with corner stress singularities. *Comput. Methods Appl. Mech. Engrg.*, 198:2227–2245.

[123] Vergote, K., Vanmaele, C., Vandepitte, D., and Desmet, W. (2013). An efficient wave based approach for the time-harmonic vibration analysis of 3d plate assemblie. *J. Sound. Vib.*, 332:1930–1946.

[124] Wandzura, S. and Xiao, H. (2003). Symmetric quadrature rules on a triangle. *Computers & Mathematics with Applications*, 45(12):1829 – 1840.

[125] Willett, E. (2004). *The basics of quantum physics: understanding the photoelectric effect and line spectra*. Rosen Publishing Group, New York.

[126] Witherden, F. D. and Vincent, P. E. (2015). On the identification of symmetric quadrature rules for finite element methods. *Computers & Mathematics with Applications*, 69(10):1232 – 1241.

[127] Wu, H., Liu, Y., and Jiang, W. (2013). A low-frequency fast multipole boundary element method based on analytical integration of the hypersingular integral for 3d acoustic problems. *Eng. Anal. Boundary Elem.*, 37(2):309–318.

[128] Young, J. C. I. and Crocker, M. J. (1975). Prediction of transmission loss in mufflers by the finite element method. *J. Acoust. Soc. Am.*, 57(1):144–148.

[129] Zienkiewicz, O. C. (2000). Achievements and some unsolved problems of the finite element method. *Int. J. Num. Meth. Eng.*, 47(9–28):144–148.

[130] Zwikker, C. and Kosten, C. W. (1949). *Sound Absorbing Materials*. Elsevier, New York.

Appendix A

Porous model

In this work, we take advantage of the frequency-dependent Johnson-Champoux-Allard's expression of the fluid density ρ_p and the dynamic fluid bulk modulus K_p to describe the fluid phase. This two fundamental characteristic parameters of fluid are given by [2]

$$\rho_p = \rho_0 \alpha_\infty \left(1 - \frac{\sigma\phi}{\mathrm{i}\rho_0\alpha_\infty\omega}\sqrt{1 - 4\mathrm{i}\frac{\eta\alpha_\infty^2\omega\rho_0}{\Lambda^2\phi^2\sigma^2}}\right), \tag{A.1}$$

$$K_p = \frac{\gamma P_0}{\gamma - (\gamma-1)\left(1 - \dfrac{8\eta\sqrt{1 - \mathrm{i}\rho_0\dfrac{Pr\Lambda'^2\omega}{16\eta}}}{\mathrm{i}\Lambda'^2 Pr\omega\rho_0}\right)^{-1}}, \tag{A.2}$$

respectively, with $\mathrm{i}^2 = -1$. These expressions are based on the harmonic time variation $e^{-\mathrm{i}\omega t}$ where the excitation of the source varies sinusoidally in time with a single frequency. This equivalent homogeneous fluid (EHF) requires the knowledge of five semi-phenomenological parameters to be taken into account, including the volume porosity ϕ, the tortuosity α_∞, the airflow resistivity σ, and the viscous and thermal characteristic lengths Λ and Λ'. All the explanations and measurement techniques with respect to these acoustical parameters are introduced concretely in the reference [2].

Figure A.1 shows the value of the complex wavenumbers $k_p = Re(k_p)(1 + \mathrm{i}\chi)$ as function of the frequency for several different materials denoted by A-D, which would be used in the following examples in this chapter. All the other necessary parameters mentioned before can be found in reference [40] for material A-C. The material D related to FM2 foam is in [110]. For the sake of completeness, the values are listed in Table A.1.

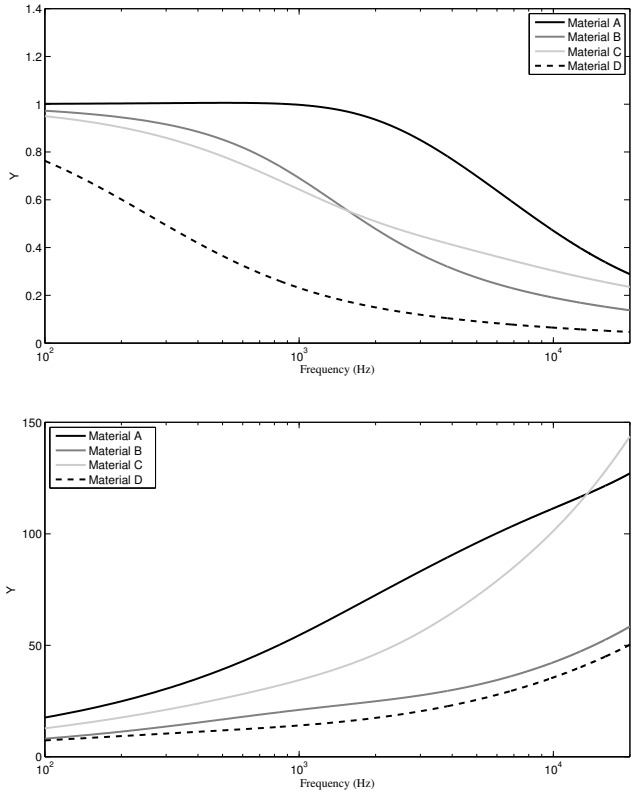

Fig. A.1 Ratio between the imaginary and the real part of the wavenumber for various materials (top); Complex wavenumbers (imaginary part) for various materials (bottom).

Parameters	Mat A	Mat B	Mat C	Mat D
ϕ	0.95	0.95	0.97	0.90
α_∞	1.00	1.00	1.54	7.8
σ $(\mathrm{kNm^{-4}s})$	105	23.0	57.0	25.0
Λ $(\mu\mathrm{m})$	35.1	54.1	24.6	226
Λ' $(\mu\mathrm{m})$	105.3	162.3	73.80	226
ρ_s $(\mathrm{kgm^{-3}})$	17	58	46	30

Table A.1 Characteristics of the materials.

Appendix B

Remarks on high order numerical quadrature

In this work, we also took advantage of advanced quadrature method to implement the surface integrals involved in the PUFEM algorithm, giving rise to a significant acceleration for computing the system matrix coefficients. To extend Gaussian quadrature to highly oscillating functions on triangle, there is a need to find dedicated quadrature rules. For instance Wandzura and Xiao [124] have obtained symmetric quadrature rules on triangle up to the order 30 [1]. More recently, Witherden and Vincent [126] proposes a algorithm and an open source software to compute near optimal rule valid up to the order 25 or 30[2].

If the order increases beyond 30, the polynomial systems are poorly conditioned and hence it is difficult to use such approaches. Alternative methods become more appropriate because it is more important to have an efficient rule than the optimal one. Three strategies have been tested during the PhD and have provided accurate results

1. The first is based on a Cartesian product rules (see [74, 105]) and involved the classical quadrature weights and abscissa of the Gauss-Legendre formula in the interval $[0, 1]$. In order to get a homogeneous distribution of the integration points, the number of points in the second direction is taken to be linearly varying.

2. The second is based on Wandzura rules (the highest) and triangle splitting. The triangle is split into sub-triangle to get the required accuracy.

[1] The coordinate and the weight can be found at https://people.sc.fsu.edu/~jburkardt/m_src/triangle_wandzura_rule

[2] https://github.com/vincentlab/Polyquad

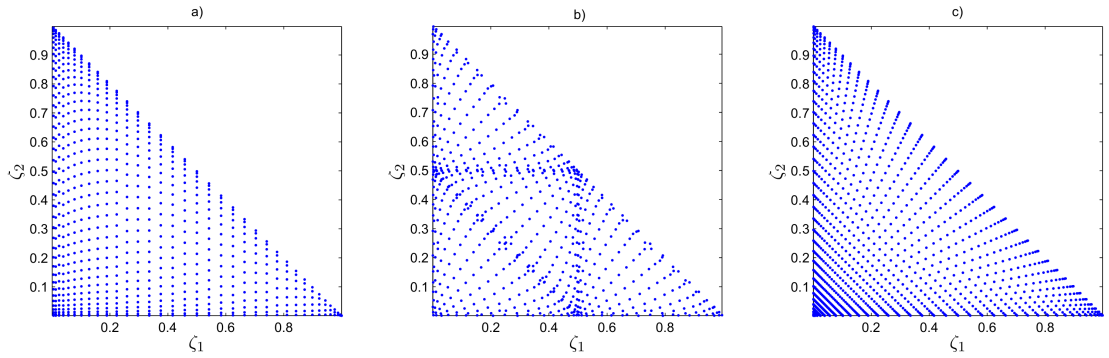

Fig. B.1 Gauss points obtained with the 3 presented strategies. a) With the Cartesian product, b) the triangle splitting and c) the Duffy transform. Around 700 points are used for each case.

3. The third is based on high-order rule inside of a quadrilateral. These rules can be constructed through a tensor product of one dimensional Gauss-Legendre rules and then use a Duffy type transformation to map these points onto a triangle [97].

The different strategies are conveniently plotted in Figure B.1. A benchmark of these methods has been performed. It has been shown that the triangle splitting and the Cartesian product are the most efficient in the intermediate range where the order is above 30. Then if the order increases again, the Duffy and triangle splitting become the two best. Because of its good versatility, the triangle splitting has been used throughout this work and especially for the computation of the boundary term involving the monopole incident field. A rule of thumb has been developed to find a relation between the number of split and the oscillation of the integrand.